Gerold Lenz

CHARACTERIZATION OF GROUND AND SYSTEM BEHAVIOUR IN WATER-BEARING FAULT ZONES

DOCTORAL THESIS

Graz University of Technology

Reviewers:

Em.Univ.-Prof. Dipl.-Ing. Dr.mont. Wulf Schubert

Institute of Rock Mechanics and Tunnelling
Graz University of Technology

Univ.-Prof. Dr.rer.nat. Florian Amann

Chair of Engineering Geology and Hydrogeology
RWTH Aachen University

Em.Univ.-Prof. Dipl.-Ing. Dr.tech. Stephan Semprich

Institute of Soil Mechanics, Foundation engineering
and Computational Geotechnics
Graz University of Technology

Graz, Juli 2020

Eidesstattliche Erklärung
Affidavit

Ich erkläre an Eides statt, dass ich die vorliegende Arbeit selbstständig verfasst, andere als die angegebenen Quellen nicht benutzt und die den benutzten Quellen wörtlich und inhaltlich entnommenen Stellen als solche kenntlich gemacht habe. Das in TUGRAZonline hochgeladene Textdokument ist mit der vorliegenden Dissertation identisch.

I declare that I have authored this thesis independently, that I have not used other than the declared sources/resources, and that I have explicitly marked all material which has been quoted either literally or by content from the used sources. The text document uploaded to TUGRAZonline is identical to the present doctoral thesis.

Graz, 27.07.2020	Gerold Lenz e.h.
Datum / Date	Unterschrift / Signature

Acknowledgements

First and foremost I would like to thank Prof. Wulf Schubert. Wulf has been sharing with me his practical expertise as well as his pragmatic approach to complex situations throughout my university and professional life. Even 15 years after going 'into the underground' when starting my diploma thesis at Wulf's institute, I never regretted a single day to step into this matter.

I would like to sincerely thank Prof. Florian Amann and Prof. Stephan Semprich for reviewing this thesis. By providing their practical and academic experience they definitely helped to further improve my work.

Furthermore, I would like to thank the project team for the Semmering base tunnel at Austrian federal railways (ÖBB), particularly Dieter Haas, Tobias Schachinger and Oliver Wagner. They have always been open to my scientific research in addition to my role as a geotechnical site engineer. I'm deeply thankful for being allowed to use all the data, knowledge and experience gained during four years of tunnel construction at the most challenging, but also most delighting site I've ever worked at.

Sincere acknowledgements are given to Itasca Consulting Group Inc., namely to Ben Harris, Judy Zetterlund and Augusto Lucarelli. Ben and Judy gave me the chance to participate in the Itasca Education Program and provided me with numerical software free of charge. Agusto Lucarelli shared his valuable experience in the field of coupled numerical analyses and got me back on the track whenever I got lost in my simulations.

Very likely, I would never have started this work without the initiative of Peter Schubert and Josef Daller, who suggested to make the best out of the 'Semmering experience' by spending the evenings on some scientific stuff. In addition to those two, all my colleagues at iC Consulenten in Salzburg and Vienna have been a great support since almost 15 years and therefore have a huge stake in this thesis. Furthermore I would like to thank Markus Brandtner, who kind of introduced me into the complex world of mechanical - hydraulic interaction in weak rock mass.

Special thanks are given to all the guys and girls at the Semmering base tunnel. Countless hours of professional (and also less professional) discussions, often paired with high-quality beverages, actually revealed the objectives of this thesis and contributed to it's progress. The comprehensive practical experience from all sides - engineers, geologists, surveying and working staff - has definitely facilitated a steep learning curve and kept me away from too fancy scientific approaches.

Alexander Kluckner and Gunter Gschwandtner have been the ones to discuss and review novel approaches and to obtain additional information and feedback. Christian Pilz contributed with scientific knowledge beyond the field of civil engineering. Thanks for all the discussions and particularly for reviewing this thesis.

As there is definitely more in life than just work, I would like to thank all my friends, particularly the 'Jungs' gang and my band colleagues, who are accompanying me now already

since decades. The days and particularly the evenings with you are quite a good alternative to spending the night on the thesis (although I often regretted the next morning).

My family has always been a great support throughout my life. And since my family enlarged by marriage, this support definitely increased as well. Thank you all for your love, support and motivation, and for keeping some problems off my back during the past years.

The greatest appreciation is given to my wife Simone. Her love and support was with me through all the years, even when times got rough. Thank you for being there!

Dedicated to my child, who provided the final kick to complete this thesis.

Hallstatt, Juli 2020

Gerold Lenz

Abstract

Groundwater contributes to the ground and system behaviour of underground structures in various ways. As tunnelling history showed, the presence of groundwater can cause collapses or severe material ingress during tunnel excavation. This thesis addresses the mechanisms leading to hydraulic failure in water-bearing rock mass under high overburden. The thesis is structured in two units. The first part deals with the distribution of hydraulic heads in vicinity of the tunnel face. A numerical parametric study for various geological settings provides the basis for empirical equations to estimate the hydraulic head field ahead of the face in both, homogeneous and heterogeneous rock mass. The developed approach is verified by pore pressure measurements during excavation of the Semmering base tunnel. The second part of the thesis addresses the failure mechanisms, which control stability of the tunnel face subject to groundwater flow. Numerical analyses are conducted to assess the effective stress conditions in vicinity of the face. In addition, a review of case histories helps to reveal the decisive failure modes. For the latter, closed-form calculation models are developed to evaluate face stability and erosion potential under seepage flow. Based on a comparative study for selected fault rocks, nomograms for a quick assessment of the ground and system behaviour are established. Last but not least, two relevant collapse scenarios are outlined, which may assist in planning of suitable prevention and mitigation measures as well as in detection of these processes during excavation.

Kurzfassung

Bergwasser kann das Gebirgs- und Systemverhalten von Untertagebauten maßgeblich beeinflussen. Zahlreiche Fallbeispiele aus der Geschichte des Tunnelbaus berichten von Verbrüchen oder massiven Materialeinbrüchen beim Tunnelvortrieb, welche im Wesentlichen auf den Einfluss des Bergwassers zurückzuführen sind. Die vorliegende Arbeit befasst sich mit den hydraulischen Versagensmechanismen im wasserführenden Gebirge unter hoher Überlagerung. Sie gliedert sich dabei thematisch in zwei Abschnitte. Im ersten Teil wird die räumliche Verteilung des hydraulischen Potentials in Ortsbrustnähe untersucht. Zu diesem Zweck erfolgen numerische Berechnungen, in welchen unterschiedliche geologische Verhältnisse betrachtet werden. Auf dieser Basis wird ein empirischer Ansatz zur Abschätzung des hydraulischen Potentials vor der Ortsbrust sowohl für homogene als auch heterogene Gebirgsverhältnisse entwickelt. Dieser Ansatz wird mittels Piezometermessungen im Zuge des Vortriebes des Semmering Basistunnels verifiziert. Der zweite Teil der Arbeit befasst sich mit den durch die Bergwasserströmung beeinflussten Versagensmechanismen der Ortsbrust. Zur Erfassung des Spannungszustandes in Ortsbrustnähe werden numerische Parameterstudien durchgeführt. Eine Auswertung von ausgewählten Fallbeispielen ermöglicht darüber hinaus Rückschlüsse auf die maßgeblichen Versagensmechanismen. Für diese Versagensmechanismen werden analytische Berechnungsmodelle zur Analyse der Ortsbruststabilität sowie des Erosionspotentials entwickelt und auf dieser Basis Nomogramme zur einfachen Abschätzung des Gebirgs- und Systemverhaltens unter unterschiedlichen geotechnischen Verhältnissen erarbeitet. Abschließend werden zwei potentielle Verbruchszenarien für den Vortrieb im wasserführenden Gebirge erläutert. Diese Szenarien sollen dazu dienen, kritische Situationen beim Vortrieb rechtzeitig zu erkennen und geeignete Gegenmaßnahmen zu planen.

Contents

Symbols and abbreviations

Latin letters

a	Aperture [mm]
A	Curve fitting parameter [-]
b	Curve fitting parameter [-]
B	Curve fitting parameter [-]
c	Cohesion [MPa]
c_u	Undrained shear strength [MPa]
C_{solid}	Fraction of solids [g/l]
d	Day
d_{dr}	Diameter of drainage [m]
d_p	Effective pore diameter [m]
D	Tunnel diameter [m]
D_{ref}	Reference tunnel diameter = 10 [m]
D^*	Curve fitting parameter [-]
e	Void ratio [-]
E	Young's modulus [MPa]
$E_{stat.flow}$	Energy of stationary flow [J]
g	Gravity [m/s^2]
G	Shear modulus [MPa]
h	Hydraulic head [m]
h_0	Initial hydraulic head [m]
h_{crit}	Critical hydraulic head [m]
k	Hydraulic conductivity [m/s]
k_r	Absolute roughness [m]
K	Intrinsic permeability [m^2]
K_d	Drained bulk modulus [MPa]
K_s	Bulk modulus of solid component [MPa]
K_f	Fluid bulk modulus [MPa]

K^*	Curve fitting parameter [-]
i	Hydraulic gradient [-]
i_{crit}	Critical hydraulic gradient [-]
M	Biot modulus [MPa]
n	Porosity [-]
p	Pore pressure [MPa]
p_0	Initial pore pressure [MPa]
p_{supp}	Support pressure [MPa]
q	Flow rate [m^3/s]
r	Radial distance to tunnel centre line [m]
r_a	Roughness coefficient [-]
r_p	Plastic radius [m]
R	Tunnel radius [m]
R_{inj}	Radius of grouting body [m]
R_w	Radius of the flow domain [m]
t	Fault zone width [m]
T	Transmissivity [1/s]
v	Discharge velocity [m/s]
v_d	Distance velocity [m/s]
v_f	Filter velocity [m/s]
v_{crit}	Critical velocity for erosion [m/s]
v_s	Groundwater flow / seepage velocity [m/s]
$v_{advance}$	Advance rate of excavation [m/d]
V	Volume [m^3]
z	Geodetic height [m]

Greek letters

α	Biot coefficient [-]
ϕ	Friction angle [^{o}]
γ	Specific weight of ground [kN/m^3]
γ'	Specific weight of ground, submerged [kN/m^3]
γ_w	Specific weight of fluid [kN/m^3]
η	Factor of safety [-]

η_w	Dynamic viscosity of fluid [Pa·s]
ν	Kinematic viscosity [m^2/s]
ν_p	Poisson's ratio [-]
ρ_d	Mass density of solid [kg/m^3]
ρ_w	Mass density of fluid [kg/m^3]
σ_0	Initial stress [MPa]
σ_1, σ_3	Total major and minor principal stress [MPa]
σ'_1, σ'_3	Effective major and minor principal stress [MPa]
σ_r, σ_t	Total radial and tangential stress [MPa]
σ'_r, σ'_t	Effective radial and tangential stress [MPa]
σ_{ft}	Tensile strength [MPa]
σ_{UCS}	Uniaxial compressive strength [MPa]

Abbreviations

BIM	Block-in-matrix
CD	Consolidated and drained triaxial test
CGF	Coarse-grained fault material
EDZ	Excavation damage zone
FGF	Fine-grained fault material
FISH	Built-in programming language of software FLAC3D ('FLACish')
HPFZ	High-permeability fault zone
LPFZ	Low-permeability fault zone
MC	Mohr-Coulomb constitutive model
MGF	medium-grained fault material
NATM	New Austrian Tunnelling Method
PH	Plastic hardening constitutive model
SQ	Sum of squares
TBM	Tunnel boring machine

1 Introduction

Groundwater is one major reason for tunnel collapses throughout history. Several historical and recent cases (Hennings, 1908; Egger et al., 1982; Knittel, 1995; Sausgruber & Brandner, 2003; Mahmutoglu et al., 2006; Schwarz et al., 2006; Millen et al., 2015) describe situations with high water or mud ingress into tunnels, often referred to as 'flowing / swimming ground', frequently followed by a collapse of the tunnel. In this thesis, the common term *flowing ground* is used to describe such conditions. Flowing ground events may cause project delays or break off, cost overrun or in the worst case even loss of human life. Tectonic fault zones are particularly prone to such events. On the one hand they usually exhibit low rock mass strength. On the other hand, differing hydraulic parameters within the fault zone may influence the distribution of hydraulic heads around the tunnel and thus yield more adverse groundwater conditions than in homogeneous rock mass.

Although the geological - geotechnical knowledge and respective methods developed rapidly during the last decades, the geomechanical failure modes triggering flowing ground conditions are hardly known. Lacking knowledge on the failure mechanism, practicable methods to assess tunnel stability in weak and water-bearing rock mass under high overburden are currently not available. Moreover, knowledge on the stability-controlling factors such as macro- and microstructure of the rock mass, mechanical and hydrogeological parameters usually is limited prior to excavation. Lacking adequate analysis tools and with limited knowledge on the geotechnical conditions only, an identification of potentially critical situations during design and construction often fails.

The thesis at hand shall contribute to understanding the ground and system behaviour (i.e. the interaction of ground and excavation without and with consideration of support measures respectively (Austrian Society for Geomechanics, 2010)) during tunnel excavation in weak and water-bearing rock mass. The decisive failure modes for various geotechnical settings are identified using novel empirical-analytical approaches and extensions to existing methods. Application of these methods during design and excavation may contribute to detect critical situations in time and therefore assist in a faster and safer construction.

2 State of the art

Assessing tunnel stability in water-bearing rock mass is an interdisciplinary task, where various geological, hydrogeological and geomechanical aspects have to be incorporated: a suitable description of the hydrogeological and mechanical properties of the rock mass, formulations for groundwater flow and stress distribution and finally a suitable calculation model. A brief literature review on these items assists in identifying the thesis' objectives and provides a basis for further research. The review focuses on:

1. Description of the hydraulic head field. For investigating excavation stability, the hydraulic head field (or pore pressure distribution respectively) close to the face and ahead of the face is of particular interest.
2. Description of the stress field around and ahead of an excavation in terms of total and effective stresses.
3. Analysis of excavation stability with consideration of groundwater impact.
4. Description of relevant geological features as well as the mechanical and hydraulic properties of fault zones.

2.1 Groundwater flow and hydraulic head field

2.1.1 Fundamentals of groundwater flow

Groundwater flow in a porous medium can mathematically be described by two fundamental equations: continuity equation (Equation 2.1) and Bernoulli equation (Equation 2.2).

$$q = v \cdot A = \text{ constant} \tag{2.1}$$

where: q = Flow rate [m^3/s]
v = Flow velocity [m/s]
A = Flow cross section [m^2]

$$\frac{E_{stat.flow}}{V} = z \cdot \gamma_w + p + \frac{\gamma_w}{g} \cdot \frac{v_s^2}{2} \tag{2.2}$$

where: E = Energy of stationary flow [kNm]
V = Volume [m^3]
z = Geodetic height [m]
γ_w = Specific weight of fluid [kN/m^3]
p = Pore pressure [kN/m^2]
g = Gravity [m/s^2]
v_s = Seepage velocity [m/s]

Groundwater flow velocity v_s usually is low. Therefore, Equation 2.2 can be simplified to the following form for expressing the hydraulic head (or hydraulic potential) h:

$$h = \frac{E_{stat.flow}}{V \cdot \gamma_w} = z + \frac{p}{\gamma_w} \tag{2.3}$$

Introducing a material-dependent factor k (hydraulic conductivity), the discharge velocity v can be described as a function of the hydraulic gradient i by Darcy's law:

$$v = k \cdot i \tag{2.4}$$

The hydraulic conductivity k depends on the pore geometry, represented by the intrinsic permeability K, as well as on the density ρ_w and the dynamic viscosity η_w of the fluid:

$$k = K \cdot \frac{\rho_w}{\eta_w} \cdot g \tag{2.5}$$

where: k = Hydraulic conductivity [m/s]
K = Intrinsic permeability [m^2]
ρ_w = Density of fluid [kg/m^3]
η_w = Dynamic viscosity of fluid [Ns/m^2]
g = Gravity [m/s^2]

In practice, the physical properties of the fluid usually do not vary to a relevant extent. Therefore, the hydraulic conductivity is commonly used to describe groundwater flow (however often referred to as permeability as well). Within the thesis at hand, the term permeability is used to qualitatively describe the ability of a rock mass for groundwater flow (e.g. low-permeability rock mass). For a quantitative specification, the hydraulic conductivity (in m/s) is used.

Strictly, Darcy's law is valid for laminar flow and evenly distributed pore volume only. Typically, flow in soils is laminar (Langguth & Voigt, 2004). However, in case of high hydraulic gradients turbulent flow may occur, where the permeability decreases with increasing hydraulic gradient.

2.1.2 Inflow into tunnels and hydraulic head field

Numerous analytical approaches exist to evaluate the inflow into tunnels under steady state conditions. El Tani (2002) gives a comprehensive, but not exhaustive, overview on available solutions. Perrochet (2005a) investigated tunnel inflow in transient conditions. In Perrochet (2005b) and Perrochet & Dematteis (2007), this approach was extended to heterogeneous rock mass conditions.

Based on a formulation to estimate the inflow into a tunnel, a description of the hydraulic head field around a tunnel (or a well) can be formulated by substituting the continuity equation (Equation 2.1) and Darcy's law (Equation 2.4) in the respective approach and consecutively solving the integral over r (radial distance). For a constant hydraulic head in the far field and radial-symmetric conditions, the pore pressure distribution in a distance r around a tunnel at steady state is given with the following equation (Vogelhuber, 2007):

$$p(r) = \frac{p_0}{ln(R_w/R)} \cdot ln(r/R) \tag{2.6}$$

where: $p(r)$ = Pore pressure at a distance r to the tunnel [MPa]
p_0 = Initial pore pressure [MPa]
R_w = Radius of flow domain [m]
R = Tunnel radius [m]
r = Radial distance to tunnel centre [m]

However, an assessment of the hydraulic head field ahead of the face, deducted from the approaches listed above, is not possible since all methods presume radial flow towards the tunnel and neglect the three-dimensional conditions close to the face.

Leitner & Müller (2007) conducted numerical analyses targeting the impact of fault zones on the groundwater inflow into tunnels. The authors showed the principal impact of layers with significantly higher or lower permeability on the total inflow. This work allows conclusions on the hydraulic head field in heterogeneous rock mass. The authors elaborate, that a transition from low- to high-permeability rock mass represents the most adverse case, because this setting yields the highest hydraulic gradients.

Zingg & Anagnostou (2008) provide a qualitative description of the hydraulic head field ahead of the face in homogeneous rock mass, based on numerical analyses. The authors assume steady state conditions and an impermeable tunnel lining. According to the authors, steady state flow can be expected in case of a hydraulic conductivity of $k \geq 10^{-8}$ m/s. In Zingg & Anagnostou (2012), a qualitative description of the hydraulic head field in heterogeneous rock mass (i.e. rock mass containing a fault zone with differing permeability) is given. This publication and Zingg (2016) furthermore show the effect of drainage in advance on the hydraulic heads.

Perazzelli et al. (2014) provide an empirical description of the hydraulic head ahead of the tunnel. The hydraulic head ahead of the face can be calculated as follows (presuming atmospheric pressure at the face):

$$h(x, y, z) = \left(1 - e^{\frac{-b \cdot x}{D}}\right) \cdot h_0 \tag{2.7}$$

where: $h(x, y, z)$ = Hydraulic head at position (x,y,z) [m]
x = Horizontal distance to tunnel face [m]
h_0 = Initial hydraulic head [m]
b = Shape parameter [-]
D = Tunnel diameter [m]

The shape parameter b was determined by a least-squares-fit to the results of numerical analyses. Similarly to the work of Zingg mentioned above, steady state flow and an impermeable tunnel lining are presumed.

2.2 Stress field

2.2.1 Total and effective stresses

For deep tunnels, fully saturated conditions can be expected in case of groundwater presence with respect to the overburden. The thesis at hand essentially deals with porous ground exhibiting a comparatively low permeability. Under the objective conditions, the ground is permeable enough to allow a certain seepage flow when subject to a change of volumetric stresses; at the same time it is not permeable enough to immediately equalize changes of the pore pressure by fluid flow. Stresses and pore pressure interact in a time-dependent process,

during which excess pore pressures are equalized by seepage. Interaction of stresses and pore pressure was first formulated in it's well known form by Terzaghi (1936) almost one century ago:

$$\sigma' = \sigma - p \tag{2.8}$$

where: σ = Total stress [MPa]
σ' = Effective stress [MPa]
p = Pore pressure [MPa]

Terzaghi's theory of a porous medium is based on a superposition of two continuous media: a skeleton of solid, incompressible grains (matrix) and an incompressible fluid, completely filling the remaining, fully interconnected pore network. Biot (1941) extended Terzaghi's concept of effective stresses from a one-dimensional consolidation problem to three-dimensional space and thus basically enabled using the consolidation theory in tunnel engineering. In contrast to Terzaghi's approach, Biot theory allows for consideration of conditions with a certain compressibility of the fluid and the matrix by introducing the coefficient α, the so called Biot coefficient:

$$\sigma' = \sigma - \alpha \cdot p \tag{2.9}$$

For an ideal porous medium, α is related to the ratio of the drained bulk modulus K_d to the bulk modulus of the matrix (K_s):

$$\alpha = 1 - \frac{K_d}{K_s} \tag{2.10}$$

The estimation of the Biot coefficient under realistic conditions, e.g. during consolidated and drained (CD) triaxial tests, is complex and time-consuming. Therefore, the estimation is rather subject to engineering judgement. For weak rock mass such as tectonic fault zones, the bulk modulus of the solid component usually is high compared to the drained bulk modulus of the medium. Hence, an assumption of $\alpha = 1.0$ is justifiable. For competent rock mass, the Biot coefficient may be significantly lower, as exemplarily shown by Selvadurai et al. (2019).

The stiffness of the porous medium is represented by the Biot modulus M:

$$M = \frac{K_f}{n + (\alpha - n) \cdot (1 - \alpha) \cdot K_f / K_d} \tag{2.11}$$

where: M = Biot modulus [MPa]
K_f = Bulk modulus of fluid [MPa]
K_d = Drained bulk modulus [MPa]
n = Porosity [-]
α = Biot coefficient [-]

The bulk modulus K_f of pure water is in the range of 2 GPa, depending on the fluid temperature. In terms of soil mechanics, the fluid usually is considered incompressible compared to the typical bulk moduli of soils. In rock mechanics, this condition cannot be presumed in general for two reasons: first, the bulk modulus of the rock mass may frequently be within the same order of magnitude (or even higher) as the fluid, even in case of comparatively weak

rock mass; second, the assumption of a single-phase fluid does not hold in practice. Pore water usually contains a certain portion of dissolved air. At first, the impact of dissolved air on the compressibility is insignificant, as long as the soil remains fully saturated (Fredlund & Rahardjo, 1993). However, as soon as the pore pressure decreases, e.g. due to stress-relief during excavation or due to drainage measures, the dissolved air precipitates and a partial saturation emerges in the ground. This process is fundamentally described by Henry's law:

$$\frac{M_i/\omega_i}{V_l} = K_{H,i} \cdot p_i \tag{2.12}$$

where: M_i = Mass of gas [kg]
ω_i = Mole mass of gas [kg/mol]
V_l = Volume of fluid [l]
$K_{H,i}$ = Henry's constant [mol/l · bar]
p_i = gas pressure [bar]

The concept of effective stresses is valid for a porous medium with fully interconnected pore space, where the pore pressure can act at every point of the medium. Innerhofer (1984) proposed a concept for the calculation of effective stresses in jointed rock mass. He introduced a wetting factor α (not identical with the Biot coefficient) to account for material bridges (non-persistent joints) within a fully interconnected network of fractures. In these material bridges, no joint water pressure can act on the (impermeable) rock mass. In other words, the wetting factor defines the area, over which a hydrostatic force can actually develop within the rock mass (Innerhofer, 2008). Deducted from Terzaghi's concept of effective stresses (Equation 2.8), Innerhofer calculates the effective stress as follows:

$$\sigma' = \sigma - \alpha \cdot p \tag{2.13}$$

with α being the wetting factor. This equation may look identical to Equation 2.9, but describes a totally different mechanical effect.

2.2.2 Stress redistribution

Kastner (1962) derived the first mathematical solution for the stress distribution around a circular hole under plane strain conditions considering linear elastic - perfectly plastic material behaviour. The stress distribution around a circular opening in an isotropic primary stress field is described by following equations:

Stress field in the plastic domain:

$$\sigma_t = \frac{\sigma_{UCS}}{k-1} + k \cdot \left(p_{supp} + \frac{\sigma_{UCS}}{k-1}\right) \cdot \left(\frac{r}{R}\right)^{k-1} \tag{2.14}$$

$$\sigma_r = \frac{\sigma_{UCS}}{k-1} + \left(p_{supp} + \frac{\sigma_{UCS}}{k-1}\right) \cdot \left(\frac{r}{R}\right)^{k-1} \tag{2.15}$$

Stress field in the elastic domain:

$$\sigma_t = \sigma_0 + (\sigma_0 - p_i^{cr}) \cdot \left(\frac{r_p}{r}\right)^{k-1} \tag{2.16}$$

$$\sigma_r = \sigma_0 - (\sigma_0 - p_i^{cr}) \cdot \left(\frac{r_p}{r}\right)^{k-1} \tag{2.17}$$

With:

$$k = \frac{1 + sin\phi}{1 - sin\phi} \tag{2.18}$$

$$p_i^{cr} = \frac{1}{k-1} \cdot (2 \cdot \sigma_0 - \sigma_{UCS}) \tag{2.19}$$

$$r_p = R \cdot \left(\frac{2}{k+1} \cdot \frac{(k-1) \cdot \sigma_0 + \sigma_{UCS}}{(k-1) \cdot p_{supp} + \sigma_{UCS}} \right)^{\left(\frac{1}{k-1}\right)} \tag{2.20}$$

where: σ_t, σ_r = Total stress in tangential and radial direction [MPa]
σ_{UCS} = Uniaxial compressive strength [MPa]
σ_0 = In-situ stress [MPa]
p_{supp} = Support pressure [MPa]
k = Lateral pressure coefficient [-]
r = Radial distance to tunnel centre [m]
R = Tunnel radius [m]
p_i^{cr} = Critical support pressure [MPa]
r_p = Plastic radius [m]
ϕ = Friction angle [^{o}]

Since then, numerous analytical solutions for the problem of stress redistribution during excavation where developed for various boundary conditions, such as anisotropic primary stress state, strain softening, and time-dependent material behaviour. A compilation of available methods and their historical development is provided in Gschwandtner (2010).

Kolymbas (1998) proposed a solution for the stress distribution ahead of the tunnel face, assuming a hemispherical tunnel face:

Stress field in the plastic domain:

$$\sigma_r = (p_{supp} + c \cdot cot\phi) \cdot \left(\frac{r}{R}\right)^{2 \cdot (k-1)} - c \cdot cot\phi \tag{2.21}$$

Stress field in the elastic domain:

$$\sigma_r = \sigma_0 - (\sigma_0 - p_{supp}) \cdot \left(\frac{R}{r}\right)^3 \tag{2.22}$$

$$\sigma_t = \sigma_0 + \frac{1}{2} \cdot (\sigma_0 - p_{supp}) \cdot \left(\frac{R}{r}\right)^3 \tag{2.23}$$

The extent of the plastic domain is calculated as follows:

$$r_p = R \cdot \left(\frac{\frac{2}{2 \cdot k+1} \cdot (\frac{3}{2} \cdot \sigma_0' - 2c \cdot \frac{cos\phi}{1-sin\phi}) + c \cdot cot\phi}{p_{supp} + c \cdot cot\phi} \right)^{\frac{1}{2 \cdot (k-1)}} \tag{2.24}$$

The equations stated above hold in terms of total stresses. However, for water-bearing rock mass with low permeability, the pore pressure needs to be considered and the analysis shall be conducted in terms of effective stresses. A first concept of introducing the effect of groundwater was proposed by Salencon (1969) (cited from Graziani & Ribacchi (2001)). He developed a solution to calculate the deformations around a tunnel under undrained conditions, postulating zero volumetric strain and undrained shear strength of the material:

$$\frac{\Delta r}{R} = \frac{c_u}{2G} \cdot e^{\left(\frac{\sigma_0 - p_{supp}}{c_u} - 1\right)} \cdot \frac{R}{r} \tag{2.25}$$

where: Δ_r = Radial displacement [m]
R = Tunnel radius [m]
c_u = Undrained shear strength [MPa]
G = Shear modulus [MPa]
σ_0 = In-situ stress [MPa]
p_{supp} = Support pressure [MPa]
r = Radial distance to tunnel centre [m]

An exhaustive description of approaches developed for this problem during the following decades would go beyond the scope of this thesis. For comprehensive (but still not exhaustive) lists it is referred to Gärber (2003) and Bobet (2010). All these approaches target the stress distribution around a tunnel under plane strain conditions. No information is provided on the stresses occurring ahead of the face. Nevertheless, the approach of Anagnostou (2009) for short-term conditions (i.e. assuming undrained conditions) is used to exemplarily demonstrate the impact of pore pressure on the stress field:

Stress field at the transition from elastic to plastic domain:

$$\sigma'_r = \sigma'_0 - s_u \tag{2.26}$$
$$\sigma'_t = \sigma'_0 + s_u \tag{2.27}$$

Pore pressure distribution:

$$p(r) = p_R + 2s_u \cdot ln\frac{r}{R} \tag{2.28}$$

With:

$$s_u = \sigma'_0 \cdot sin\phi + c \cdot cos\phi \tag{2.29}$$
$$p_R = p_{supp} - \sigma'_0 + s_u \tag{2.30}$$
$$r_p = R \cdot e^{\frac{\sigma_0 - p_{supp} - s_u}{2s_u}} \tag{2.31}$$

where: σ'_r, σ'_t = Effective stresses in radial and tangential direction [MPa]
σ'_0 = Effective in-situ stress [MPa]
$p(r)$ = Pore pressure at distance r [MPa]
p_R = Pore pressure at excavation boundary [MPa]
ϕ = Friction angle [^{o}]
c = Cohesion [MPa]
p_{supp} = Support pressure [MPa]
R = Tunnel radius [m]
r_p = Plastic radius [m]

In the elastic domain, the stress field can be calculated using Equations 2.16 and 2.17. Figure 2.1 exemplarily shows the stress distribution around a tunnel in terms of total and effective stresses. In the plastic domain, the change in total stresses due to excavation is compensated

by the pore pressure in short-term and the effective stresses therefore remain constant. Close to the excavation boundary, effective stresses increase due to negative pore pressures, which act favourably on tunnel stability. With increasing distance to the tunnel, positive pore pressures occur and decrease the effective stresses. At this point it is acknowledged, that the assumption of undrained behaviour represents a rather theoretical approach. As soon as cracking initiates in the rock mass, pore pressures reduce to atmospheric pressure.

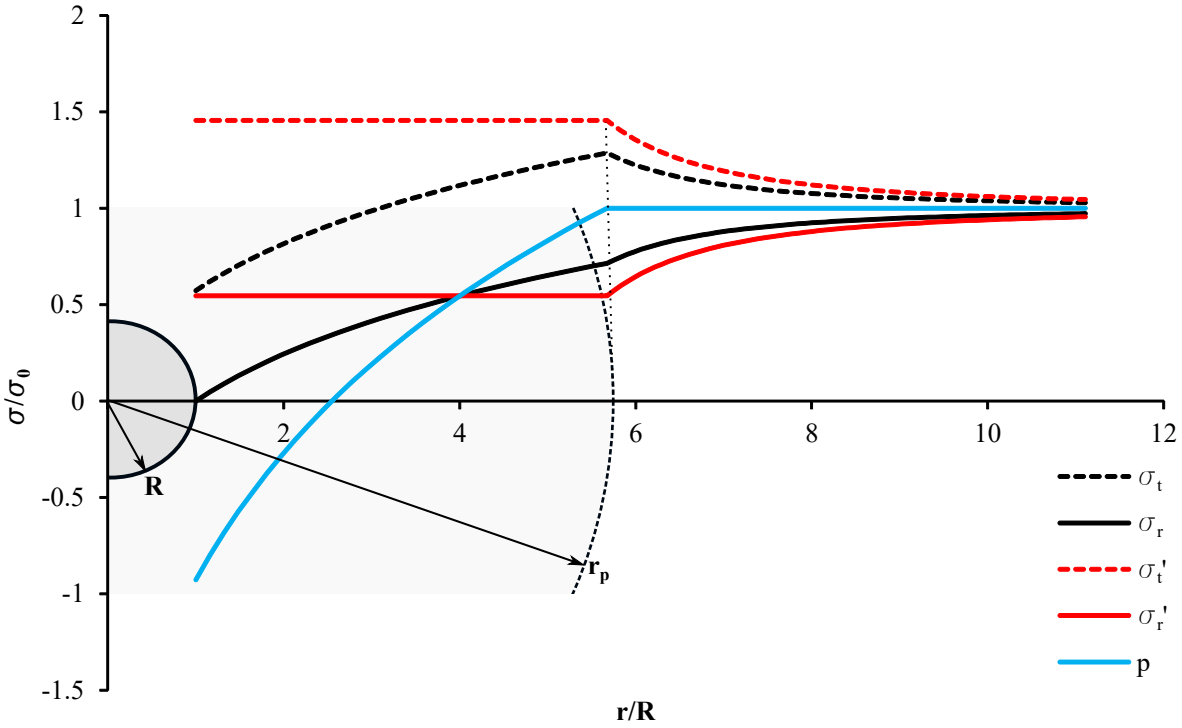

Figure 2.1: Stress redistribution and pore pressure for short-term behaviour (exemplarily)

Postulating undrained conditions for the short-term behaviour yields one boundary of the possible stress field. In case of rock mass with very low permeability and ductile behaviour, this approach may come close to the actual conditions. Over time, the pore pressure distribution changes to a steady state, causing changes of the effective stresses and consequently volumetric strains as well as time-dependent displacements. The other boundary of possible behaviour is represented by fully drained conditions; i.e. any hydraulic gradients resulting from a change of total stresses is immediately compensated by seepage flow and the steady-state pore pressure distribution prevails. These conditions typically apply for high-permeability rock masses. The actual stress state around the excavation is somewhere in between those boundaries, primarily depending on the rock mass permeability and the drainage conditions. This simple example emphasizes the complexity of the interaction of pore pressures and stress field, even when assuming the most simple conditions, that is plane strain conditions in homogeneous rock mass. Numerical analyses, allowing for consideration of mechanical-hydraulic coupling, therefore represent the state of the art for investigating tunnel stability in low-permeability rock mass.

2.3 Stability analysis

As stated above, the presence of groundwater affects the effective stress field around an excavation. Furthermore, tunnelling generates seepage forces towards the excavation by locally

lowering the water table. These effects have to be taken into account during stability analysis. The focus of this thesis and consequently of the literature review is set on the stability of the tunnel face.

Several approaches exist for analysing face stability in undrained conditions, dating back to the 1960's (Ruse, 2004). However, none of these approaches allows for consideration of seepage forces. Egger et al. (1982) proposed a solution for the design of a grouting body under seepage forces, using the convergence-confinement method. Similarly to Kolymbas (1998), they assumed a hemispherical tunnel face. The required strength of the grouting body can be calculated by following equation:

$$\sigma_{UCS} \leq \sigma_0 \cdot \frac{1}{2} \cdot \frac{R_{inj}}{R_{inj} - R} \tag{2.32}$$

where: σ_{UCS} = Uniaxial compressive strength [MPa]
σ_0 = In-situ stress [MPa]
R_{inj} = Radial extent of grouting body [m]
R = Tunnel radius [m]

Anagnostou & Kovári (1994) and Anagnostou & Kovári (1996) developed a limit-equilibrium approach to analyse face stability with consideration of seepage forces. The latter were computed numerically and then introduced into the limit-equilibrium calculation. To evaluate face stability, the authors assumed a wedge-and-prism failure body (Figure 2.2, left). The vertical loading of the failure body is computed using the silo theory. The required support pressure p_{supp} can be calculated (for atmospheric pressure at the face):

$$p_{supp} = F_0 \cdot \gamma' \cdot D - F_1 \cdot c + F_2 \cdot \gamma' \cdot h_0 - F_3 \cdot c \cdot \frac{h_0}{D} \tag{2.33}$$

where: p_{supp} = Support pressure [MPa]
F_0, F_1, F_2, F_3 = Coefficients [-]
γ' = Specific weight of ground, submerged [MN/m^3]
D = Tunnel diameter [m]
c = Cohesion [MPa]
h_0 = Initial hydraulic head [m]

F_0 to F_3 are dimensionless coefficients depending on the friction angle, the geometric parameters and the ratio of dry to submerged unit weight. The respective values can be obtained from nomograms provided in the publications cited above.

Lee et al. (2003) used the upper bound solution for stability analysis, considering conical blocks to describe the failure body (see Figure 2.2, right). Similarly to the method of Anagnostou and Kovári, the seepage forces are computed numerically.

In Zingg & Anagnostou (2008), Zingg & Anagnostou (2012) and Zingg (2016), the method of Anagnostou and Kovári was extended to allow for the consideration of drainage in both, homogeneous and heterogeneous rock mass. Still, stability analysis requires a numerical computation of the seepage forces in these approaches.

Perazzelli et al. (2014) developed an empirical approximation for the hydraulic head field in vicinity of the tunnel face in homogeneous rock mass (see Equation 2.7), which allowed for a fully analytical computation of face stability. Stability analysis is conducted using the method of slices, where the failure body is subdivided into horizontal slices. Equilibrium is calculated by solving the volume integral of vertical and horizontal forces over the failure

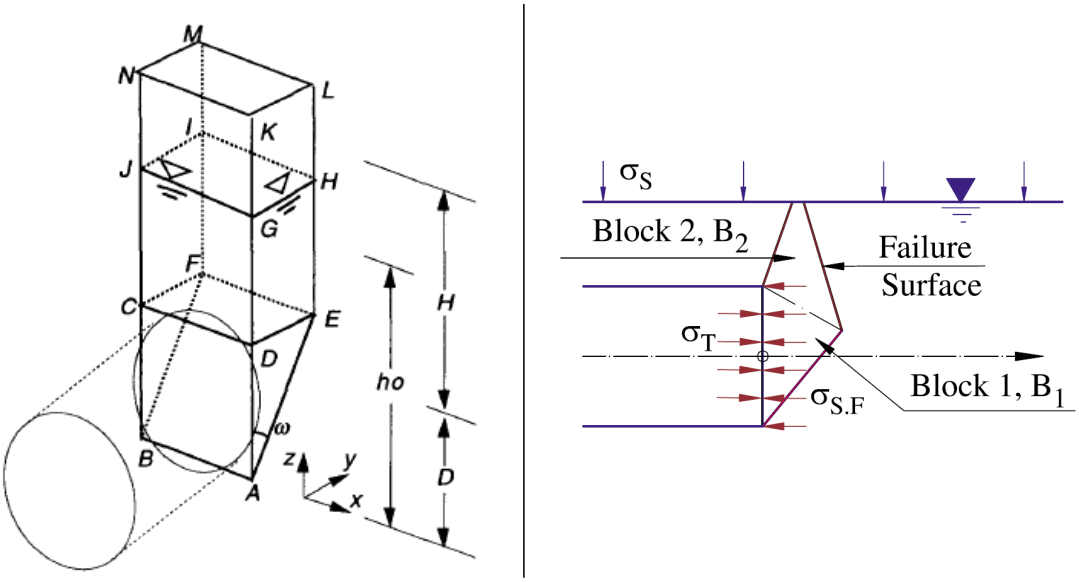

Figure 2.2: Failure modes for investigation of tunnel face stability: right: wedge - prism (Anagnostou & Kovári, 1996); left: conical (Lee et al., 2003)

body. With respect to the applied method, tensile failure within the prism (e.g. in case of high hydraulic gradients ahead of the face and highly cohesive rock mass) can be identified and a horizontal layering of different ground types can be considered.

2.4 Geological model of tectonic fault zones

When dealing with fault zones, a distinction is made between brittle faults and ductile shear zones (Riedmüller et al., 2001). Ductile shear zones are generated in deeper parts of the crust, while fault zones are common features of the upper crust. Tunnels (even when being referred to as deep tunnels) usually reach comparatively shallow depth only. Hence, brittle fault zones are of particular interest within this context (although ductile fault zones that have been subject to exhumation may be encountered as well), having the most significant impact on the rock mass properties. They show a heterogeneous internal structure, varying material properties and discrete shear planes due to their considerable thickness (Fasching & Vanek, 2011). Within this thesis, the term fault zone refers to brittle fault zones solely.

2.4.1 Geological features of fault zones

Brittle fault zones are lithologically heterogeneous, anisotropic and discontinuous (Faulkner et al., 2010). Using a simple conceptual model, a fault zone contains a fault core (in which the shear deformation is accumulated), surrounded by a zone of fractures and faulting in the so-called damage zone. Depending on the genesis of the fault zone and the geotechnical conditions, a damage zone may form on either side of the fault core, on one side only, or faulting may occur without formation of a geotechnically relevant damage zone. The fault core consists of gouge or cataclasite (or a combination of both), the damage zone generally consists of fractures over a wide range of length scales, and subsidiary faults (Faulkner et al., 2010). Fault zones may consist of a singe fault core or a series of multiple fault cores. In areas, in which the rock mass has been subject to less strain, preserved rock bodies may exist (Fasching & Vanek, 2011). Fault zones consisting of cataclasite and preserved bodies

often are referred to as block-in-matrix (BIM) rocks. The thickness of the fault core may range from centimetres to several tens of metres. A conceptual model of a brittle fault zone is shown in Figure 2.3. Complementary to this macrostructure, fault zones typically exhibit a microstructure formed by a network of fractures. The fracture density depends on the distance to the fault core (Faulkner et al., 2010), or in other words the fracture density increases gradually when approaching the fault core.

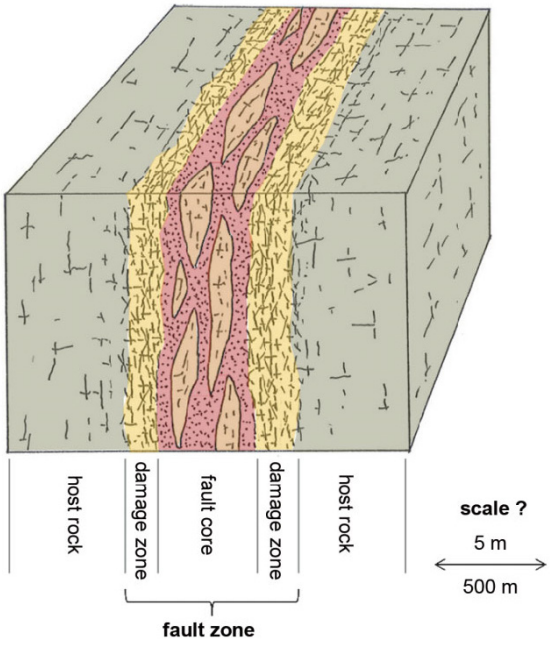

Figure 2.3: Model of internal fault zone architecture: host rock, damage zone, fault core (Fasching & Vanek, 2011)

The classification of fault rocks is often subject to scientific context or to project-specific requirements. Consequently, a plethora of classification systems for fault rocks exist. Within this thesis, the classification scheme proposed by Riedmüller et al. (2001) is used (see Figure 2.4). This system distinguishes between cohesive (rock-like) and non-cohesive (soil-like) rocks. Cohesive rocks are classified by the type of cementation. Non-cohesive (cohesionless) rocks are differentiated in blocks and matrix. Blocks are classified to their volumetric proportion. The matrix is classified by the particle size, following the engineering soil description, into G- (gravel-dominated), S- (sand-dom.), M- (silt-dom.) and C- (clay-dom.) cataclasite.

2.4.2 Mechanical properties of fault zones

With respect to the large variety of fault materials (see Figure 2.4) no general statements can be made on the values of mechanical parameters in fault zones. However, fault rocks have several mechanical aspects in common:

- The mechanical parameters in block-in-matrix (BIM) conditions are affected by volumetric proportion and mechanical parameters of the blocks (Riedmüller et al., 2001). Furthermore, the shape of the blocks and the direction of action relative to the block orientation influence the mechanical performance. An attempt towards a constitutive model for BIM rocks was presented by Pilgerstorfer (2014).
- Both, strength and stiffness parameters of fault rocks highly depend on the primary

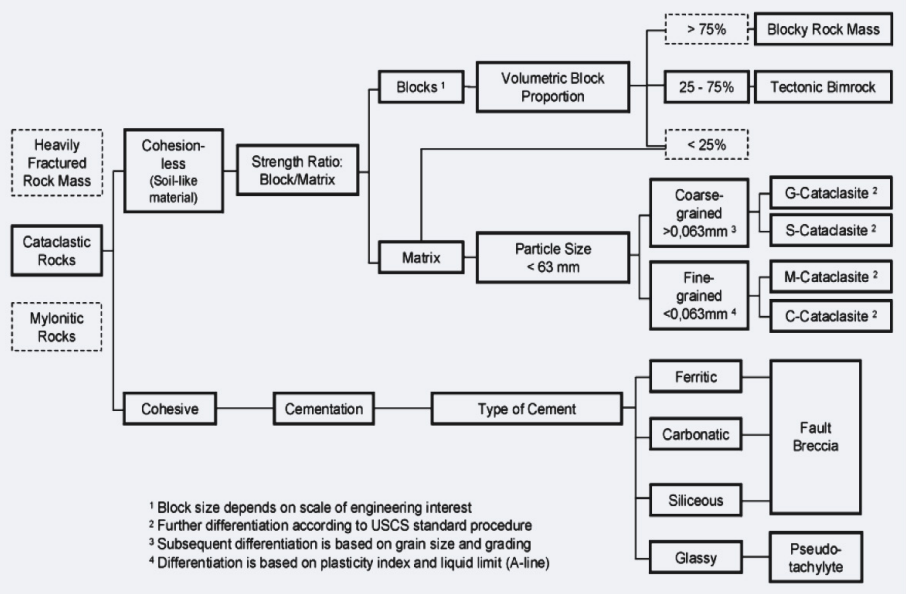

Figure 2.4: Engineering geological classification of cataclastic rocks (fault rocks) acc. to Riedmüller et al. (2001)

stress level (Asef & Reddish, 2002; Habimana et al., 2002).

- The softening behaviour of fault rocks is still largely unknown and may reach from a rather ductile behaviour to brittle failure (Radončić, 2011).
- The mechanical parameters may degrade due to fluid flow processes. For instance, seepage may cause wash-out of gypsum from a previously well-cemented fault rock, causing a loss of cementation and grain-to-grain bonding. Such cases were encountered in the author's personal experience during excavation of the Semmering base tunnel. In the worst case, dissolution processes may create or enlarge voids (Gysel, 2002).

2.4.3 Hydraulic properties of fault zones

Similarly to the mechanical properties, the hydraulic parameters of fault zones cover a wide range. It is straight forward to note that the permeability, and hydraulic conductivity respectively, of a fault rock depends on grain size distribution and void ratio, as shown in numerous studies. Empirical equations, e.g. according to Kozeny-Köhler (Langguth & Voigt, 2004), describe this relationship:

$$k = \frac{1}{r_a} \cdot 0.0405 \cdot \frac{e^3}{1+e} \cdot d_p^2 \tag{2.34}$$

where: k = Hydraulic conductivity [m/s]
r_a = Roughness coefficient [-]
e = Void ratio [-]
d_p = Effective pore diameter [mm]

The distribution of permeabilities in a fault zone is controlled by the lithology of the host rock and the deformation mechanism during faulting (Bense et al., 2013). In fault cores of strike-slip faults, a large part of the shear strain is accumulated, resulting in fine-grained cataclasites and low permeability. The damage zone is characterised by a network of fractures with increasing density towards the fault core and therefore typically exhibits a comparatively

high permeability. A qualitative distribution of permeabilities within a fault zone is shown in Figure 2.5. In case of normal faults, the permeability distribution may be significantly different: extension during faulting may increase the permeability of the fault zone and the fault zone may act as a conduit (Bense et al., 2013).

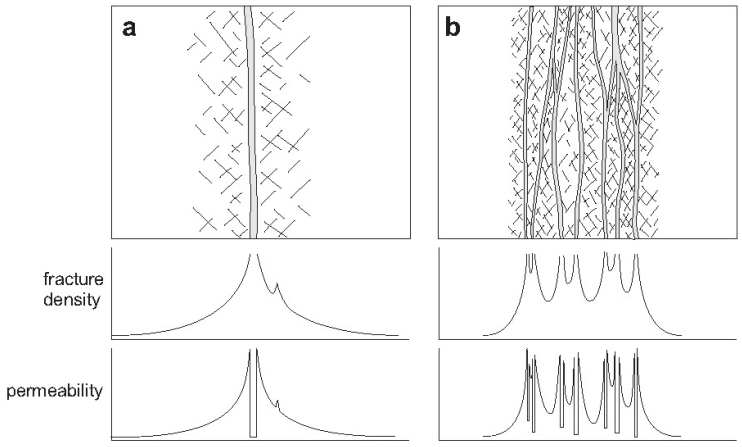

Figure 2.5: Distribution of fracture density and permeability within a fault zone consisting of a single core (a) and multiple cores (b), from Faulkner et al. (2010)

In addition to this general description on permeability in fault zones, further conclusions can be drawn on the hydraulic properties of fault rocks:

- Fault zones typically exhibit anisotropic permeability. The permeability normal to the direction of shear may be lower by several orders of magnitude than the permeability parallel to the shear movement (Evans et al., 1997; Faulkner et al., 2010; Winkler et al., 2010).
- Similarly to the mechanical parameters, rock mass permeability depends on the confinement stress and decreases with depth (Evans et al., 1997; Winkler & Reichl, 2014).
- Excavation works can affect the permeability of the surrounding rock mass in various ways, e.g. by opening of existing cracks or formation of new fractures. This effect is commonly known as excavation damage zone or excavation disturbance zone (EDZ). The before-mentioned influences can lead to a permeability increase by several orders of magnitude up to a depth of several metres into the rock mass (Pusch, 1989; Bossart et al., 2002; Millen et al., 2015).
- Dissolution and erosion effects may create or enlarge voids and therefore significantly increase the rock mass permeability (Gysel, 2002; Millen et al., 2015).

3 Case histories

Complementary to the assessment of the state of the art, a literature review is performed with the focus on cases of material ingress or collapse of tunnels excavated in water-bearing rock mass. Practical experience may allow for a better understanding of potential failure modes and conditions particularly prone to critical situations.

3.1 Albula tunnel

The challenging conditions during the construction of the Albula tunnel in Switzerland at the beginning of the 19th century are comprehensively summarized by Theiler et al. (2013). Several water and mud ingresses occurred in a 113 m long tunnel section consisting of locally disintegrated, 'sponge-like', water-bearing Rauhwacke. These events caused a delay in construction of 11 months. The initial water pressure in the objective section was approximately 12 bar. One major event occurred at chainage 1193 when the excavation hit an open joint partly filled with strongly weathered Rauhwacke (in form of cohesionless, fine sand). The tunnel was flooded by mud, stones and water over a length of 50 m and a height of 0.5 m. After restarting the excavation in a floor adit (with a smaller excavation cross section), a second inrush of water and material occurred at chainage 1200 when *'large quantities of sand and water gushed in with irregular pressure from all sides'*. The total amount of solids made up approx. $1500\,m^3$ (see Figure 3.1). A reduction of inflow rates over time finally allowed to complete the excavation. According to the authors, the described incidents are essentially related to karst phenomena in the Rauhwacke formations. High hydraulic gradients close to the tunnel face occurred due to the locally high permeability contrast between the high-permeability rock mass and the low-permeability joint fill. In contrast to the observed behaviour in the section containing karst features, a section of weak, highly porous and water-bearing Rauhwacke could be excavated without significant problems.

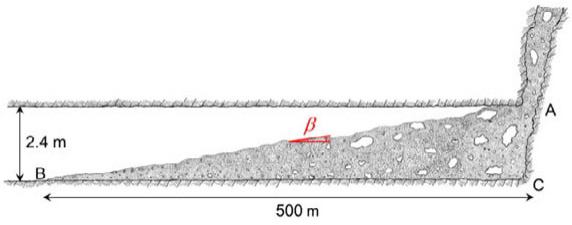

Figure 3.1: Longitudinal section of the floor adit with dimensions of the collapse (Theiler et al., 2013)

3.2 Karawanken tunnel

During the excavation of the Karawanken road tunnel at the border of Austria and Slovenia, an exploratory drilling at chainage 3010 hit a water-bearing zone with high water pressure

in the range of 6 - 7.5 MPa, causing a water inflow of 90 l/s and ingress of dolomitic particles (Schubert & Marinko, 1992). The water inflow stopped after short time due to jamming of the borehole. Excavation was continued with drainage pipes and reduced round length until a major water- and mud-inflow occurred at chainage 3028. Drainage drillings repeatedly jammed and could not allow for a significant drawdown of the water level. As an alternative, small drainage holes with a diameter of 0.5 m where blasted. After blasting the second hole, the face collapsed, followed by a massive water and material ingress, which filled the first 100 m behind the face. The collapsed section could be rehabilitated with drainage drillings, an additional drainage gallery and grouting measures. When passing the collapsed section, a 6 - 8 m thrust fault within the dolomite section could be identified as the origin of the water inflow.

3.3 Kaponig tunnel

Knittel (1995) reported two major collapses related to weak and water-bearing rock mass during the excavation of the Kaponig tunnel in southern Austria during the early 1990s. At chainage 1164, high water inflow in the invert was reported, followed by heaving of the rock mass in the invert in a range of 30 - 50 cm. After applying extensive drainage measures and installing a temporary shotcrete invert, excavation could be continued. Five metres later, a part of the tunnel face collapsed and a water inflow of up to 250 l/s occurred, which transported rocks '*up to the size of a suitcase*'. Based on core drillings and site observations, an approx. 1 m thick mylonitic layer, dipping moderately steep against the direction of excavation, could be identified, which obviously acted as an aquitard to a water bearing damage zone behind, consisting of heavily fractured mica schists. The initial hydraulic head is unknown. Measurements after the event still indicated a water pressure of significantly more than 10 bar. The collapsed section was re-excavated using heavy face support, spiling and drainage pipes. However, a second collapse occurred only two rounds later and a debris cone of 45^o formed at the face. Immediately after the collapse, sustaining water inflow in the range of 120 l/s occurred. After causing a delay of several months, the objective section could be excavated using an injection pipe roof and extensive drainage measures.

3.4 Tunnel Brixlegg East

During the excavation of the reconnaissance tunnel Brixlegg East in Tyrol, Austria, severe water and material ingress from a fault zone within the dolomites of the Raibl group occurred. During drilling of an anchor hole in the tunnel wall, a major water inflow of 25 l/s occurred, resulting in the wash-out of sand- to gravel-sized dolomitic material (Sausgruber & Brandner, 2003). High hydraulic gradients occurred due to an impermeable layer of fault gauge, striking in an acute angle to the tunnel axis. This layer acted as an aquiclude to the water-bearing, porous fault breccia of the Raibl dolomites behind, which were short-circuited by the borehole. The water pressure in the fault zone was approx. 6 bar. To successfully resume tunnelling, extensive grouting measures had to be applied.

3.5 Tunnel Vomp East

As reported by Schwarz et al. (2006), hydraulic failure of the invert occurred during bench excavation when intersecting fine-grained and low-permeability sediments (aquiclude), alternating with coarse-grained sediments (aquifer). Due to the initial water pressure of 3 - 5 bar,

a water inflow of up to 50 l/s was reported. The massive inflow triggered erosive forces and resulted in the formation of cavities with a size of several hundred cubic metres in vicinity of the tunnel. Injections were ruled out as mitigation measure for rehabilitation due to the high percentage of fine-grained material in the rock mass. The section was finally completed using a combination of drainage umbrellas in the invert and pipe umbrellas covering top heading and bench.

3.6 Ayas tunnel

An inrush of flowing ground with a total volume of 150 - 200 m^3 was reported at the Erkeksu drive of the Ayas tunnel in Turkey when excavation reached a fault zone with a length of 40 - 50 m at the contact between volcanic and loose sedimentary rock (Mahmutoglu et al., 2006). The ground comprised of saturated clays, silts, sands and gravels. No elaboration could be found on the actual reason or the timely progress of the collapse. After the event, an additional investigation campaign with several core drillings was conducted. Samples of clay from these drillings showed water contents far beyond the plastic limit of these soils. Finally, the problematic section could be completed by means of jet grouting.

3.7 Tunnel Tapovan

Millen et al. (2015) reported about a TBM getting trapped in a heterogeneous fault zone at an overburden of approx. 900 m in the Himalayas, India. '*Approximately 24 h later, massive surges of high pressure subsurface water, containing faulted rock material, broke two crown segments of the segmental lining immediately behind the tailskin with the initial flow rates reaching circa 700 l/s compounding the trapping problem*'. The authors traced the massive water inflow to an increase of rock mass permeability caused by an opening of cracks in the jointed rock mass due to relaxation as a consequence of tunnel excavation. As reported, displacements of 100 mm and larger were measured in this section. A nearby aquifer was short-circuited by the developing zone of higher permeability. In order to recover the TBM, drainage drifts were excavated and a grouting campaign was carried out.

3.8 Semmering base tunnel

During excavation of the eastern-most construction lot of the Semmering base tunnel, lot SBT1.1, up to the time of releasing this thesis three incidents involving groundwater in weak rock mass occurred. These cases have not been published yet, but refer to the author's personal experience.

At chainage 921 of the drive Gloggnitz, the top heading face collapsed when approaching a fault zone consisting of clayey fault gouge with a thickness of only around 20 cm. This fault zone acted as an aquiclude to a water bearing damage zone with an initial hydraulic head of 80 - 90 m situated behind the fault. The rock mass ahead of the fault consisted of heavily fractured Riebeckit gneiss with comparatively high strength. The collapsed face exhibited a bullet-shaped failure surface (see Figure 3.2). While water inflows in the range of 2 - 3 l/s were observed before the collapse, a significant surge in the range of >10 l/s occurred immediately after the collapse. The face could be stabilized with a shotcrete plug in time before gravity- and erosion-controlled enlargement of the void could occur. Consecutively, drainage drillings were applied in order to lower the hydraulic head behind the fault zone.

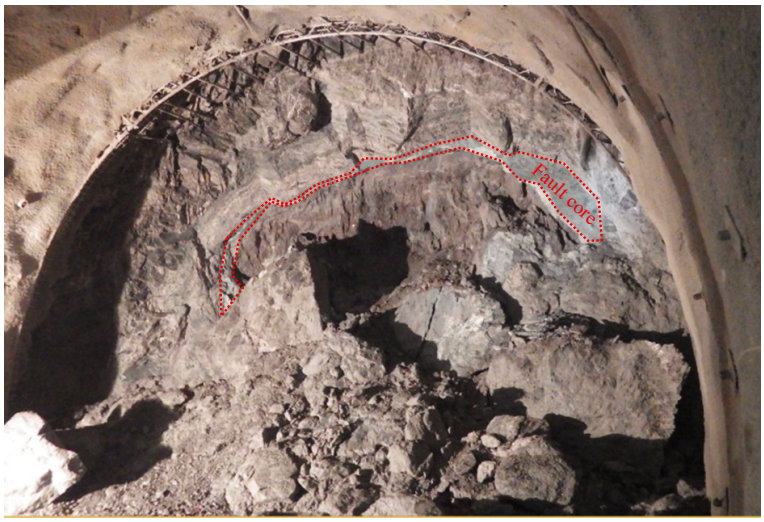

Figure 3.2: Face collapse caused by seepage forces at the Heuberg fault (chainage 921), Semmering base tunnel (ÖBB Infrastruktur AG, 2019)

Inflow rates decreased quickly to the level before the collapse and the excavation could be re-started without further problems.

The second event occurred when excavation proceeded through faulted, fine-grained mica schists exhibiting a comparatively low permeability at an overburden of approx. 120 m. At chainage 3466, an exploration drilling hit a lense of water-bearing and permeable dolomites at a distance of 18 m to the tunnel face, followed by an initially moderate inflow of 5 l/s, which seized rapidly. Three additional drainage pipes were installed consecutively to facilitate drainage of the rock mass. In one of these drainages a short-term inflow of 15 l/s, accompanied by wash-out of fine particles, was recorded. The inflow decreased rapidly and the surge seized within hours. When continuing excavation, a minor overbreak occurred close to the drainage due to loose material with high water content. To prevent further overbreaks, injection spiles with a length of 4 m were drilled. During drilling, massive water and material inflow occurred. This inflow decreased rapidly again and the excavation area could be supported by shotcrete. At this point, excavation was interrupted to allow for further drawdown of the water level. While excavation was halted, intermittent and by trend increasing water and material inflows of up to 60 l/s could be observed at various drainage drillings. This behaviour could be explained by jamming of drainages followed by the formation of new flow paths and progressing erosion. Approximately 4 h after stopping the excavation, cracks developed in the shotcrete at the tunnel face, indicating incipient deformations of the face. To prevent a collapse, a gravel backfill was applied to the face and additional drainage pipes were installed. However, one day later and after intermitting water and material inflow the tunnel face collapsed. The area close to the face was flooded by several consecutive mudflows, until the situation stabilized more or less by itself, leaving a flat debris cone up to the crown. As a consequence of the voids created during this event, the collapse propagated up to the surface within the next days, forming a chimney with a diameter of approx. 10 m. Figure 3.3 illustrates selected stages of the collapse. At the time of preparing the thesis at hand, this section has not yet been re-mined. The rehabilitation concept foresees drainage from the second tube (running parallel at an axial distance of approx. 50 m), local grouting measures and reinforcement of the debris by pipe umbrellas.

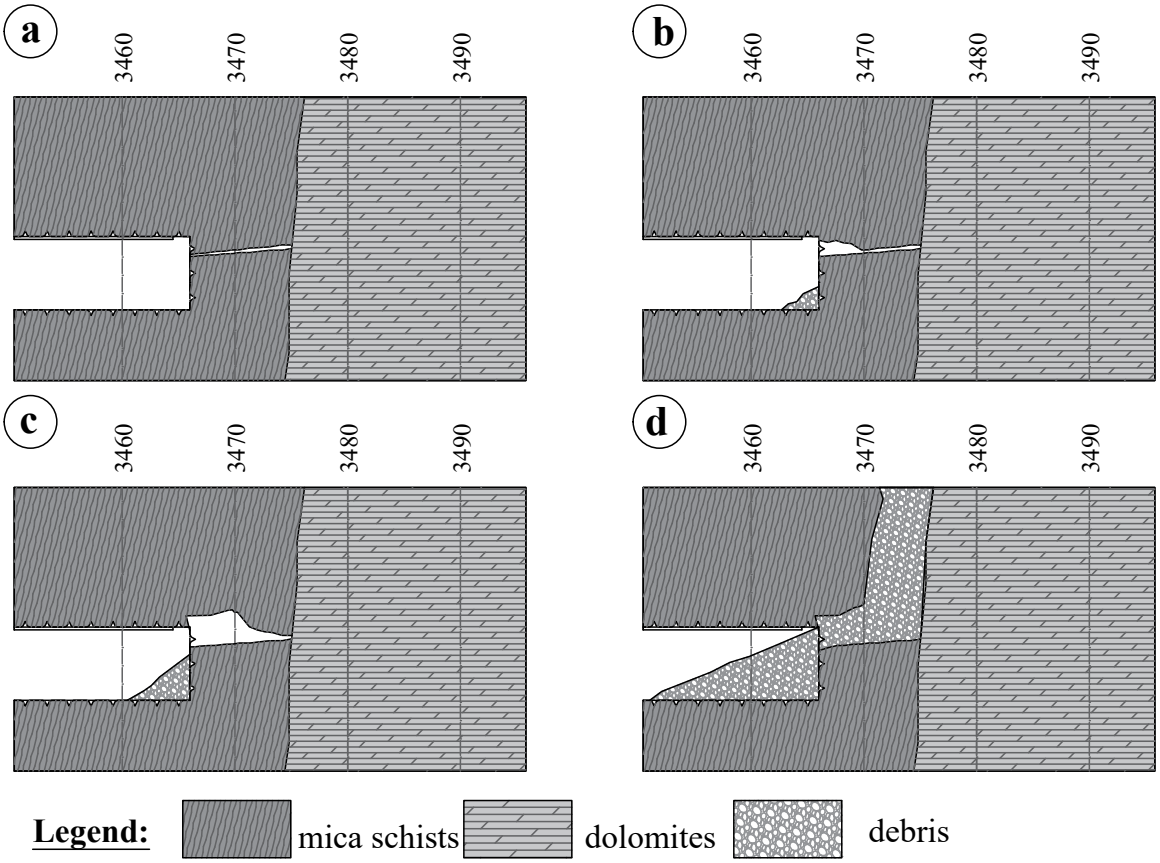

Figure 3.3: Geotechnical interpretation (longitudinal section) of collapse at chainage 3466, Semmering base tunnel: (a) initiation of erosion by drainage drilling; (b) formation of cavities due to continuous wash-out of material; (c) enlargement of erosion-formed cavities by local overbreaks; (d) collapse; modified after ÖBB Infrastruktur AG (2019)

A second major ingress of water and material occurred during excavation of the logistic caverns in the intermediate access Göstritz. The rock mass in the objective area consisted of a series of Rauhwacke with intercalated fault breccia. The hydraulic head was approx. 230 m above tunnel level. In course of the excavation, peak water inflows of 15 l/s and formation of several minor voids due to erosion within the fault breccia could be observed. These minor voids locally formed an interconnected network close to the tunnel. However, all these situations could be mitigated by drainage measures and local grouting and filling of voids. Thus, excavation successfully proceeded over several months. In June 2019, a sudden ingress of water and material with an inflow rate of 15 - 20 l/s occurred in the invert of the cavern. Due to the significant material inflow, a void of several cubic metres formed quickly in the invert. Filling the void with gravel and pre-cast concrete blocks failed due to the high inflow rate. Moreover, the inflow rate increased over time and reached a steady state level of 90 l/s, containing solid particles of up to 260 g/l. An approach to stop the inflow by injections with polyurethane foam failed because the injection material was spilled out before reacting. Over time, the particle content decreased, but the inflow rate remained at 85 - 90 l/s for several months. At the time of preparing this thesis, the inflow could be piped, excavation could be restarted and an injection campaign is intended to stop the inflow and to fill the newly formed voids. Based on the knowledge gained so far, this event is traced back to a zone (or a 'hose') with locally high permeability, either caused by a high degree of fracturing or by karst phenomena, while the rest of the rock mass predominantly exhibited low permeability, but

being prone to erosion at the same time. The high-permeability zone is connected to a large adjacent aquifer. When the tunnel excavation reached the high-permeability zone, it short-circuited the aquifer through local erosion channels, resulting in high hydraulic gradients and consequently high inflow (Figure 3.4). The rock mass surrounding the cavern mainly consisted of breccia with carbonatic bonding. This bonding obviously deteriorated by seepage and made the rather fine-grained rock mass particularly prone to erosion. Since the short-circuited aquifer exhibits a large volume and is continuously re-charged by surface water, this system reached a more or less steady state over several months up to the time being.

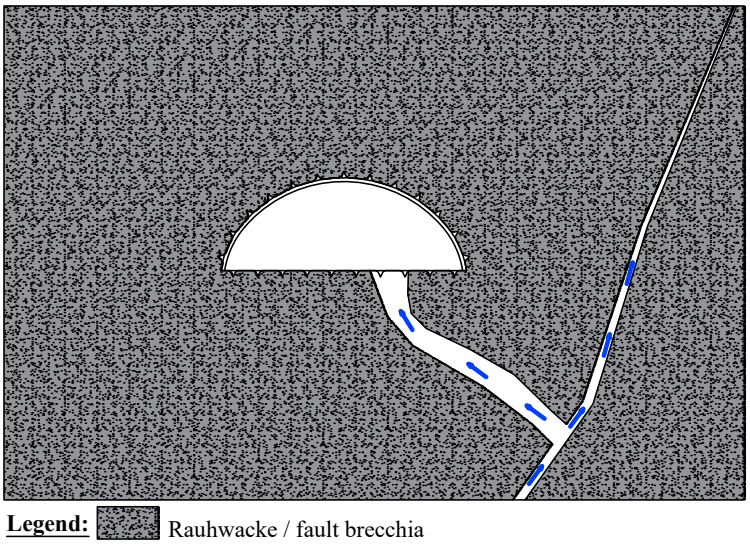

Figure 3.4: Geotechnical interpretation of water and material inflow in logistic cavern Göstritz, Semmering base tunnel; modified from ÖBB Infrastruktur AG (2019)

3.9 Conclusions

Although the events described above occurred under various geotechnical conditions, several similarities could be identified. The presented cases allow conclusions on the failure mechanisms and on potential mitigation measures:

- All events involved heterogeneous rock mass with zones of strongly differing hydraulic properties (i.e. either lower or higher permeability) compared to the host rock. Consequently, high hydraulic gradients could occur close to these geological features. Even fault zones with comparatively low thickness may influence the hydraulic head field significantly.
- Rock mass with low or no particle bonding and a high degree of saturation is particularly prone to flowing ground conditions. In deep tunnels, such zones can for instance be found in fault zones from brittlely deformed, competent rocks such as carbonates, granites and quartzites, or in karstified areas (Sausgruber & Brandner, 2003).
- Flowing ground conditions do not necessarily require high hydraulic heads. Several of the events listed above occurred at a moderate groundwater level of 50 - 100 m.
- Formation of a hydraulic bypass (short-circuit), e.g. due to open cracks in the rock mass or due to boreholes, causes a local increase of the hydraulic gradients and thus can trigger or facilitate erosion processes.

- The consequence of flowing ground conditions is a matter of particle transport and therefore highly depends on the total groundwater inflow into the tunnel. When total inflow is low or re-charge to the objective area is limited, water inflows may run dry after a short time or at least reduce to a handleable level before causing severe damage.
- From the case histories above, three different failure mechanisms can be distinguished: erosion of loose or poorly lithified material through cracks or boreholes (Albula tunnel, tunnel Brixlegg East, tunnel Tapovan, Semmering base tunnel); local or large scale collapse of the face triggered or amplified by seepage forces, followed by water and mud ingress (Karawanken tunnel, Kaponig tunnel, Semmering base tunnel); hydraulic failure by heave due to upwards-directed seepage flow (Kaponig tunnel, tunnel Vomp East).
- Tunnel excavation can affect the mechanical or hydraulic parameters of the surrounding rock mass. This can lead to an increase of permeability (Tapovan tunnel) or a reduction of rock mass strength (e.g. by increasing the water content of clayey material, as reported by Mahmutoglu et al. (2006)).
- The cases reported above emphasize the importance of drainage in such conditions. Drainage was an integral part of the mitigation measures in all reported cases.
- In addition, grouting may be used to reduce the inflow rate and increase rock mass strength. However, the applicability of grouting is subject to certain limitations. In rock mass with low permeability and consequently low grout penetration, benefits of grouting may be limited. In case of high flow velocities, the grout may be washed out before reacting.
- Complementary to drainage and grouting, forepoling measures (e.g. pipe roof) or face bolting may be used to prevent local overbreaks and provide adequate working safety.

4 Objectives

After reviewing the state of the art regarding analysis of tunnel stability in water-bearing rock mass and a number of case histories on this topic, following issues requiring additional research and clarification have been identified:

1. *Estimation of the hydraulic head field*:
   An assessment of the hydraulic heads around an excavation lays the basis for stability analysis. Numerical calculations are undoubtedly state of the art to evaluate hydraulic heads during tunnel excavation. However, this type of analysis offers certain drawbacks: it is often time-consuming and requires high effort in modelling, particularly when analysing the three-dimensional distribution of hydraulic heads; and it requires special and often expensive software. Complementary closed-from solutions could allow for parametric studies covering large parameter ranges or quick assessments as well as back-analyses during excavation. The existing solution for estimating hydraulic heads ahead of the face by Perazzelli et al. (2014) applies to the special case of homogeneous rock mass at steady state only. Approaches accounting for a transient hydraulic head or heterogeneous rock mass are currently not available. Furthermore, Perazzelli et al. (2014) consider an impermeable tunnel lining. This may be justified for mechanical excavation with pre-cast, watertight segmental lining. However, in conventional excavations the lining usually exhibits a certain permeability and the hydraulic head field in this case may differ significantly from results using the existing approach.

2. *Characterization of ground and system behaviour in water-bearing fault zones*:
   The failure mechanisms postulated in literature (chapter 2) do not match with the description of failure process reported in the case histories (chapter 3). On the one hand, the failure mechanisms described in chapter 2 do not consider failure triggered by discrete features of the rock mass, such as cracks or boreholes. Rather, a continuum modelling approach is applied. On the other hand, the existing methods presume loading conditions which are typical for homogeneous rock mass at low stress level. The effect of stress redistribution during excavation, particularly in over-stressed rock mass, is not taken into account. In addition, heterogeneous rock mass influences the stress redistribution and thus the loading of the ground ahead of the face. Last but not least, the interaction of stress redistribution and pore pressure in low-permeability rock mass is not taken into account. The existing analysis approaches therefore do not apply for the objective conditions of this thesis, dealing with deep tunnels in heterogeneous, weak and water-bearing rock mass. For these conditions, specific failure mechanisms should be derived and corresponding analysis models should be established.

3. *Influence of the excavation damage zone*:
   Practical experience shows that the hydraulic as well as the mechanical parameters of the rock mass are affected by excavation. Although the formation of an excavation damage zone is well known, its impact on stability of the tunnel face has not been investigated yet.

Based on these topics, the goals for the thesis at hand have been defined as follows:

1. Conception of a simplified geotechnical model for heterogeneous rock mass and identification of typical hydraulic and mechanical parameter ranges in fault zones as basis for all following issues.
2. Development of an empirical closed-form solution to estimate the hydraulic head field ahead of the tunnel face in both homogeneous and heterogeneous rock mass. This solution should apply for the typical range of hydraulic parameters in fault zones and account for transient flow conditions as well as the steady state. Additionally, the impact of an excavation damage zone on the hydraulic head field should be studied. The transient hydraulic head field during tunnelling should be verified by measurements on site, preferably conducted in faulted rock mass.
3. Qualitative assessment of the influence of heterogeneous rock mass and interaction of stress and pore pressure redistribution on the stress field ahead of the tunnel face. This analysis should contribute to understanding the relevant failure mechanisms.
4. Identification of potential failure mechanisms in water-bearing fault zones, deducted from case histories and numerical analyses.
5. Derivation of closed-form calculation models or criteria for the previously identified failure mechanisms to allow for fast assessment of the ground and system behaviour.
6. Comparative analysis for typical geotechnical settings in fault zones to reveal characteristic conditions prone to particular failure modes.

The beneficial effects of drainage, grouting and support measures will only be dealt with briefly within this thesis. Comprehensive studies on the effect of drainage in tunnelling are provided by Zingg (2016). The design of grouting measures is a science of its own and would therefore go beyond the scope of this thesis.

At this point it is recalled that the input data of the geotechnical-hydrogeological model is subject to a high number of unknowns and uncertainties during assessment of the geological model and parameter determination. These uncertainties may be reduced when putting high effort into exploration, but they can never be eliminated. In tunnelling practice, the observational method may be applied in such cases. The latter requires to assess the range of possible behaviour and to determine acceptable limits of behaviour beforehand. The thesis at hand should contribute to these tasks by providing easily applicable analysis tools to be used during design and construction.

5 Geotechnical-hydrogeological model

With respect to the complex geological and hydrogeological conditions in fault zones (see chapter 2), a simplified geotechnical model is established, providing the foundation for further analyses. The model contains following features:

- an idealized model of fault zone architecture;
- a range of typical hydraulic parameters of fault rocks;
- an adequate constitutive law and according mechanical parameters of the rock mass;
- an assessment of the hydraulic boundary conditions such as the permeability of the tunnel lining and the impact of groundwater re-charge on the hydraulic head field.

5.1 Fault zone architecture

Zoning of heterogeneous rock mass (i.e. rock mass with two or more compartments with different hydraulic and / or mechanical properties) into certain subdomains is a matter of scale. With respect to the high number of unknowns in the geological model when dealing with heterogeneous rock mass in deep tunnels, zoning is restricted to three subdomains: host rock, damage zone and fault core (see also Figure 2.3). Uniform hydraulic and mechanical properties as well as a fully interconnected pore / joint network within each of these subdomains is presumed. Based on the conceptual models for fault zone architecture (see chapter 2), following setting types are distinguished (see Figure 5.1):

- homogeneous rock mass;
- 1-layer-model: rock mass with a single fault or damage zone;
- 2- and 3-layer-model: rock mass with a fault core, accompanied by a damage zone on one or two sides, respectively;
- multi-layer-model: rock mass with multiple fault and damage zones.

To account for various geological conditions, the width of each compartment is varied. Within this thesis, a distinction is made between high-permeability fault zones (HPFZ) and low-permeability fault zones (LPFZ), that is fault zones with higher and lower permeability compared to the host rock. A qualitative distribution of the permeabilities in the different setting types is shown in Figure 5.1.

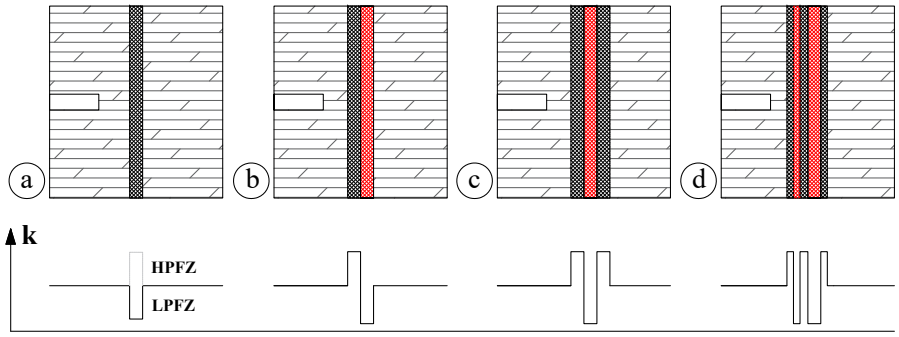

Figure 5.1: Setting types for heterogeneous rock mass: a): 1-layer-model; b) 2-layer-model; c) 3-layer-model; d) multi-layer model; Abbreviations: HPFZ...high-permeability fault zone; LPFZ...low-permeability fault zone

5.2 Hydraulic conductivity of fault rocks

The typical range of hydraulic conductivities in fault rock is determined by compiling data from various available project documents and publications: Evans et al. (1997), Sausgruber & Brandner (2003), Vogelhuber (2007), Winkler & Reichl (2014), ÖBB Infrastruktur AG (2015) and ÖBB Infrastruktur AG (2019). The range of hydraulic conductivities for selected lithologies is presented in Figure 5.2.

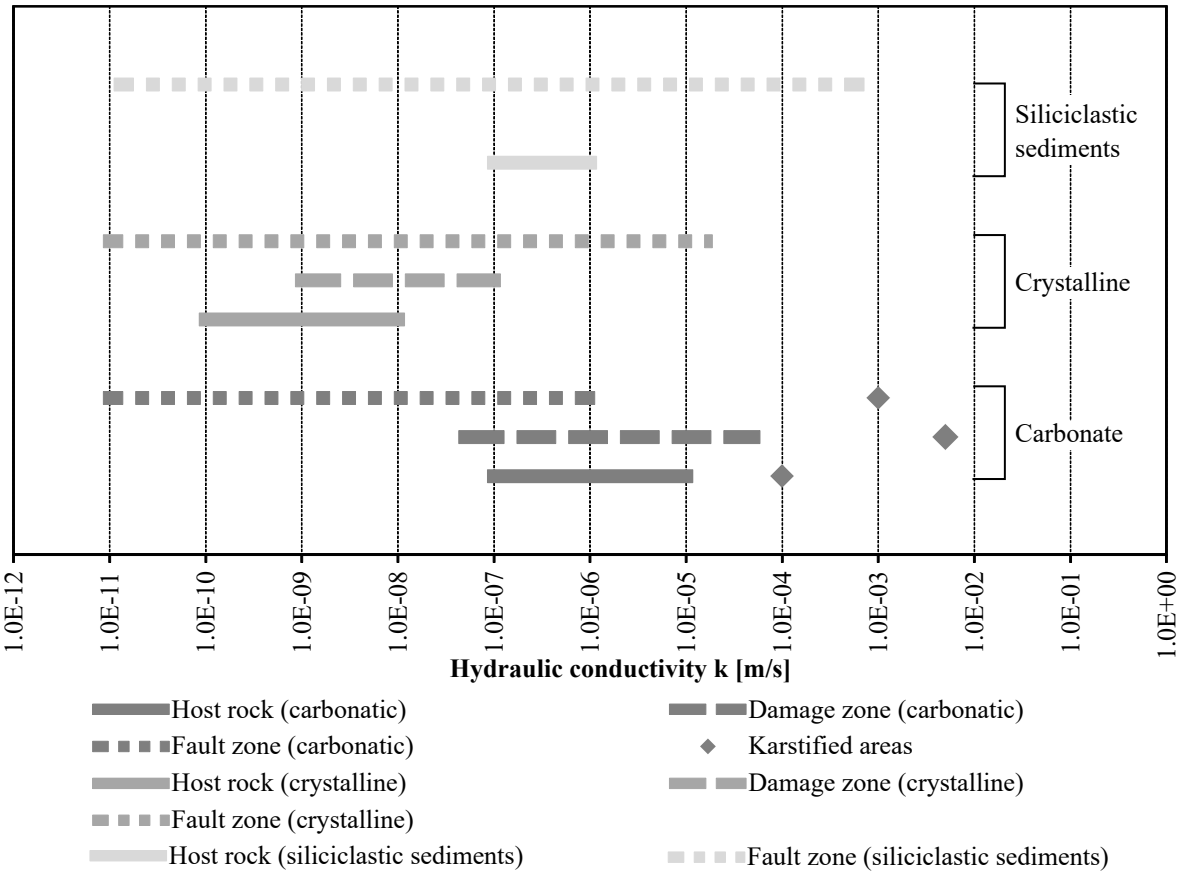

Figure 5.2: Ranges of hydraulic conductivity for different lithologies

The permeability of the host rock primarily depends on the fracture density, since fluid transport occurs primarily through fractures (Prinz & Strauss, 2011). From this point of

view, the comparatively narrow range of intact rock hydraulic conductivities displayed in Figure 5.2 may reflect project-specific conditions rather than a general range. For fault and damage zones, conductivities are typically within a range of $k = 10^{-5}$ m/s or lower, independently of the lithology. Under certain conditions, e.g. in case of karstified areas or poorly lithified zones, permeability may be 2 - 3 orders of magnitude higher. This evaluation shows that the permeability of fault zones may deviate from those of the host rock to either side, that is permeability may be (significantly) higher or lower.

5.3 Material types for comparative analysis

Similarly to the hydraulic parameters, the mechanical parameters of fault rocks vary in a large range. Suitable quantitative correlations between the parameters that potentially control the ground behaviour, such as strength and deformation properties, permeability, grain size distribution, etc., do not exist. Sausgruber & Brandner (2003) suggested simple qualitative relationships between the geomechanical and hydrogeological properties of fault rocks in brittle fault zones. They distinguished incompetent host rocks (e.g. phyllites, marls, shale) and competent host rocks (e.g. carbonates, granite, quartzites). Fault rocks from incompetent rocks exhibit cohesive soft-rock character with low compressive strength and low permeability. Fault rocks from competent rocks (at least at a young age) are considered to be more or less cohesionless (sand- to gravel-like) and highly permeable. With increasing age of the fault rock, these parameters may be altered to higher strength and lower permeability, e.g. due to chemical lithification.

Following this classification, three material types for further analysis are defined to cover the possible range of geotechnical conditions in fault zones:

- FGF: fine-grained fault material (C-, M-cataclasite acc. to Riedmüller et al. (2001)), e.g. resulting from cataclasis in silicates;
- CGF: coarse-grained fault rock (S-, G-cataclasite), representing cataclastic quarzites / carbonates;
- MGF: medium-grained fault rock (M-, S-cataclasite), representing a tectonic melange of the two before-mentioned materials.

All further analyses will be conducted representatively for these three material types. The required material parameters are deducted from representative laboratory samples taken during the exploratory campaign for the Semmering base tunnel (ÖBB Infrastruktur AG, 2019). The geometrical indicators (grain size) as well as the mechanical and hydraulic parameters of these material types are compiled in Table 5.1. The grain size distribution is displayed in Figure 5.3.

5.4 Permeability of the tunnel lining

The permeability of the tunnel lining directly affects the distribution of hydraulic heads. An impermeable lining allows only a local drawdown of the hydraulic head in vicinity of the face (provided that the face exhibits a certain permeability and atmospheric conditions). Consequently, high hydraulic gradients develop close to the face. The steady state is reached comparatively fast because only a small domain is affected by the drawdown. In a certain distance behind the face, the hydraulic heads return to their initial value (provided that sufficient groundwater re-charge occurs). In case of a fully permeable tunnel lining and

			Material type		
			Fine-grained fault rock (FGF) phyllite cataclasite	**Medium-grained fault rock (MGF)** Tectonic melange of silicatic and carbonatic host rocks	**Coarse-grained fault rock (CGF)** quartzite cataclasite
Effective weight	γ'	[kN/m^3]	24	24	24
Porosity	n	[-]	0.17	0.20	0.23
Void ratio	e	[-]	0.20	0.25	0.30
Effective cohesion	c'	[MPa]	0.20	0.10	0.05
Effective friction angle	ϕ'	[^{o}]	20	25	35
Hydraulic conductivity	k	[m/s]	10^{-10}	10^{-8}	10^{-6}
			Grain size distribution		
Mass percentage at sieving	clay	[%]	25	10	1
	silt	[%]	32	29	6
	sand	[%]	27	40	25
	gravel	[%]	16	21	68
Coefficient of uniformity	U	[-]	100	250	90
Grain size at 50 %	d_{50}	[mm]	0.02	0.16	6.0
Grain size at 10 %	d_{10}	[mm]	0.0001	0.002	0.10

Table 5.1: Mechanical parameters and grain size distribution for selected material types

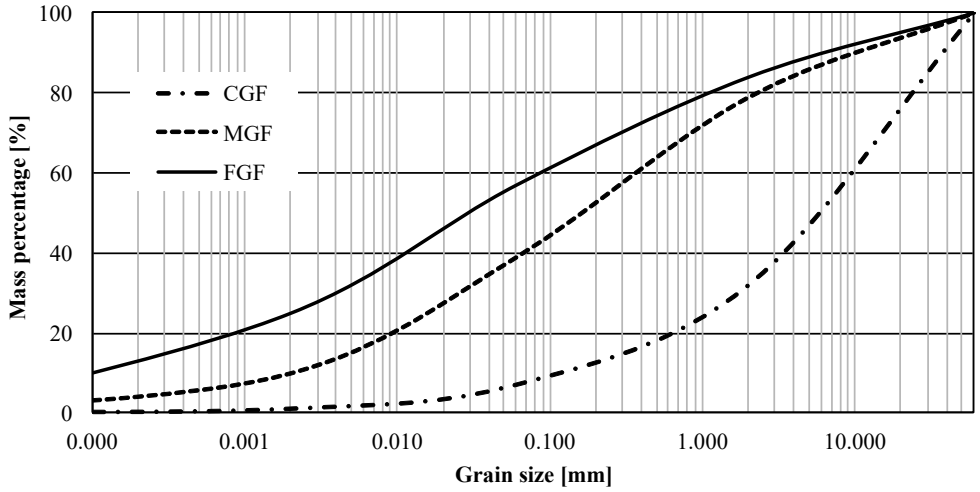

Figure 5.3: Grain size distribution for selected material types

athmospheric pressure in the tunnel, both, lining and face act as drainage faces. Hydraulic gradients at the face may be lower than in case of an impermeable lining. At the same time, drawdown occurs in a much larger domain and the steady state develops significantly slower. Eventually, steady state conditions may be reached far behind the face in case of low permeabilities.

Zingg (2016) in her research presumed an impermeable tunnel lining for shotcrete linings with respect to the low permeability of the shotcrete itself. In practice, any shotcrete lining exhibits a plethora of cracks (e.g. due to shrinkage or mechanical damage as well as construction joints) and holes (e.g. drainage holes, drill holes for rock bolts). Furthermore, groundwater may surge through the invert of the tunnel. Owing to the versatile possibilities for drainage, the assumption of an impermeable shotcrete lining cannot be justified. This is confirmed by the findings of Holter (2015), who carried out piezometer measurements around Norwegian road tunnels with shotcrete linings. Holter's measurements showed that an atmospheric pressure prevails at the extrados of the tunnel lining after reaching the steady state. Sufficient moisture is transported through the shotcrete to compensate any hydraulic gradient by seepage. In

addition, an impermeable tunnel lining is practically limited to hydraulic heads of 100 -200 m (in the best case) due to the limited bearing capacity of the lining. Consequently, a fully permeable tunnel lining is considered in all analyses within this thesis.

5.5 Impact of groundwater re-charge

Although rock mass compartments can exhibit a natural groundwater flow depending on topography and re-charge (Leitner & Müller, 2007), the initial flow velocity is assumed equal to zero within all analyses. Furthermore, sufficient groundwater re-charge from the surrounding rock mass is presumed, so that no drawdown of the global groundwater table occurs. In other words, the hydraulic head will remain on the initial level at a certain distance to the tunnel. With respect to tunnel stability and ground behaviour, this represents the more unfavourable case. In case of a confined aquifer without sufficient groundwater re-charge the groundwater table is lowered continuously due to inflow into the tunnel. Initially, when the aquifer is reached by the excavation, similar hydraulic gradients may occur as in case of sufficient groundwater re-charge. However, hydraulic gradients decrease over time, depending on the inflow rate to the tunnel and on the volume of the aquifer, and conditions for tunnelling may turn more favourable.

5.6 Excavation damage zone

As described in chapters 2 and 3, excavation may affect the properties of the rock mass, e.g. by opening of discontinuities or forming of new cracks due to mechanical impact or rock mass relaxation. In case of conventionally driven tunnels, drill holes for rock bolts and spiles may additionally affect the permeability if they are not fully grouted. In Frieg et al. (2012), a conceptual model of the excavation damage zone (EDZ) was established, which is modified within this thesis by incorporating the possible impact of drill holes (see Figure 5.4). The thickness of the EDZ was reported to be 1.5 - 2 m (Frieg et al., 2012; Bossart et al., 2002). Since the increase of permeability depends on several factors, such as the initial permeability, the joint and fracture network, the type and quality of the excavation method, etc., a general approach for assessing the permeability of the EDZ is not available. As a common ground, a permeability increase of several orders of magnitude can be assumed (Pusch, 1989; Bossart et al., 2002; Frieg et al., 2012). Within this thesis, a thickness of the EDZ of 1 - 2 m and an increase of permeability of one to two orders of magnitude is investigated.

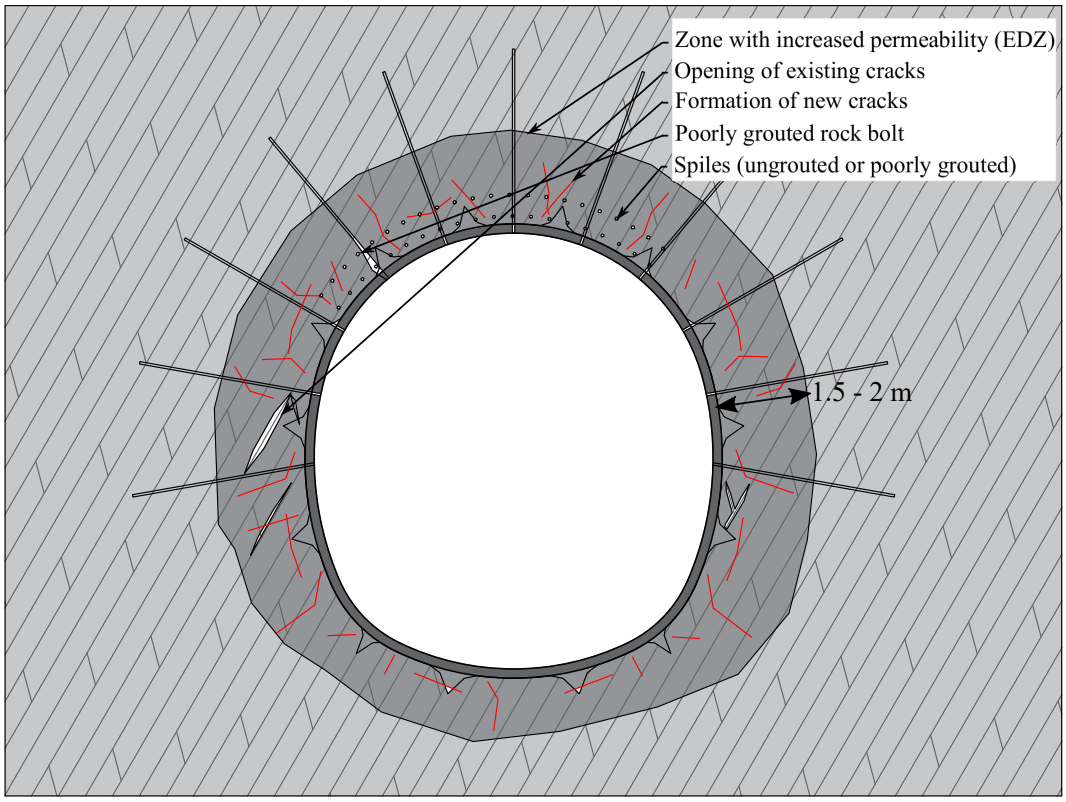

Figure 5.4: Geotechnical model of the excavation damage zone (EDZ)

6 Hydraulic head field

6.1 General

Knowledge of the hydraulic head field lays the basis for stability analysis in water-bearing rock mass. Since no adequate analytic approaches are available for the objective geotechnical conditions (see chapter 2), a sensitivity study with numerical methods is conducted to create a data pool for further analysis.

Neglecting any mechanical effects, such as the interaction of stresses and pore pressures, the potential factors controlling the hydraulic head field around an excavation are as follows:

- Permeability of the rock mass;
- Fault zone architecture and permeability contrasts in case of heterogeneous rock mass;
- Advance rate of the excavation;
- Geometry (size) of the excavation;
- Permeability of the tunnel lining;
- Groundwater regime (balance of discharge and re-charge) in the flow domain;
- Initial hydraulic head.

Within the sensitivity study, items 1-4 are varied in typical ranges for deep infrastructure tunnels. With respect to the low groundwater flow velocity, the term for kinetic energy is neglected and the hydraulic head can be calculated from the pore pressure only (see Equation 2.3).

6.2 Numerical analysis

6.2.1 Modelling

All numerical analyses are conducted with the software FLAC3D (Itasca Consulting Group, Inc., 2017). The results presented in this chapter are obtained by fluid flow calculations without consideration of hydraulic-mechanical coupling. The tunnel lining is assumed fully permeable (see chapter 5). The hydraulic heads therefore solely depend on the pressure difference between groundwater and tunnel, on the permeability of the rock mass, on the flow time (or the advance rate of the excavation respectively) and on the geometric dimensions of the model.

The numerical model used for the majority of the calculations consists of 51 000 zones (i.e. finite elements) with prismatic shape. Lateral and longitudinal extents are 100 m each (see Figure 6.1). In the majority of calculations, only one half of the tunnel is modelled to minimize calculation effort (except for models with asymmetric boundary conditions, such as fault zones crossing in an acute angle to the tunnel axis). Assuming sufficient re-charge to the flow domain (as explained in chapter 5), the hydraulic head at the outer boundaries

is fixed to the initial value, except for the boundary at $x = 0$. Test calculations with varying model dimensions were carried out beforehand and showed that a lateral extent of 100 m of the numerical model is sufficient to accurately reproduce the hydraulic head field under the objective conditions. Within the tunnel, atmospheric pressure is presumed. Fluid flow into the tunnel is allowed both at the face and the lining.

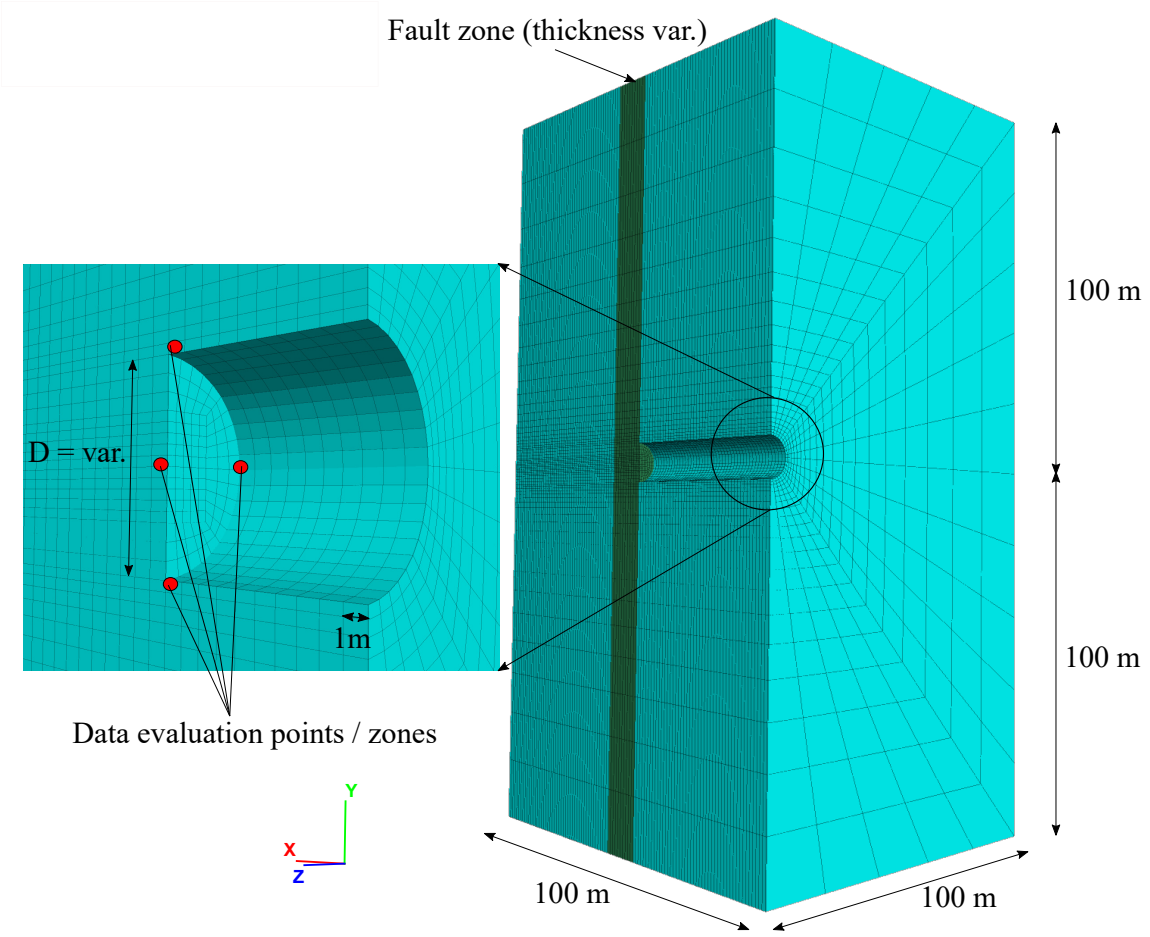

Figure 6.1: FLAC3D base model for numerical analysis

The tunnel diameter varies between 5 - 15 m, representing typical dimensions of infrastructure tunnels. For sake of simplicity, a circular shape is presumed. The model discretization in longitudinal direction is 1 m. A stepwise excavation with a round length of 1 m is considered in all analyses. The calculations are performed with following sequence:

1. Round x: Excavate material and set pore pressure in lining and tunnel face to zero
2. Calculate fluid flow. As the primary convergence criterion, a steady-state fluid flow is defined. In case this criterion is not met (and the steady state is not reached), flow time of the respective excavation step is limited to the time required to excavate one round (t_{round}) at a specific advance rate (ranging from 2 - 16 m/d). After reaching the round time, excavation proceeds to the next step. Thus, a transient hydraulic head field can be generated.
3. Round $x + 1$: sequence as described above

The sequence above still represents an approximation of the real excavation process since excavating and applying atmospheric pressure in the actual round happen in an infinitesimally

small time step. The real development of the hydraulic heads during one round varies over time. For sake of simplicity, real time behaviour is not logged (unless otherwise noted). Consequently, only a range of the hydraulic head field can be determined (see Figure 6.2). All evaluations shown in the following chapters refer to the upper bound, that is pore pressures are logged immediately before excavating the next round at the time t_{round} (time required for completing one excavation round).

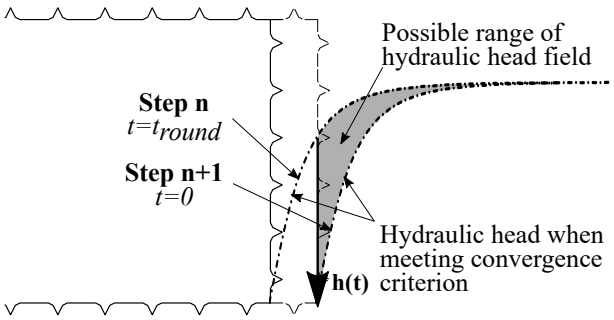

Figure 6.2: Possible range of the hydraulic head field during excavation of one round

6.2.2 Data evaluation

Pore pressure data is logged in four selected zones (crown, sidewall, invert and axis, see Figure 6.1) in each excavation step using a routine coded in FISH, the built-in programming language of FLAC3D. Additionally, the accumulated inflow at the tunnel face is recorded for each round with a FISH routine.

For homogeneous conditions, all data is evaluated at station x = 50 m, i.e. in the middle of the model, where the influence of the boundaries is expected to be a minimum. For heterogeneous conditions, results are evaluated in form of state lines and trend lines at every gridpoint / zone in the selected positions to allow for comparability in longitudinal direction. This type of data evaluation is commonly used to display displacement monitoring data.

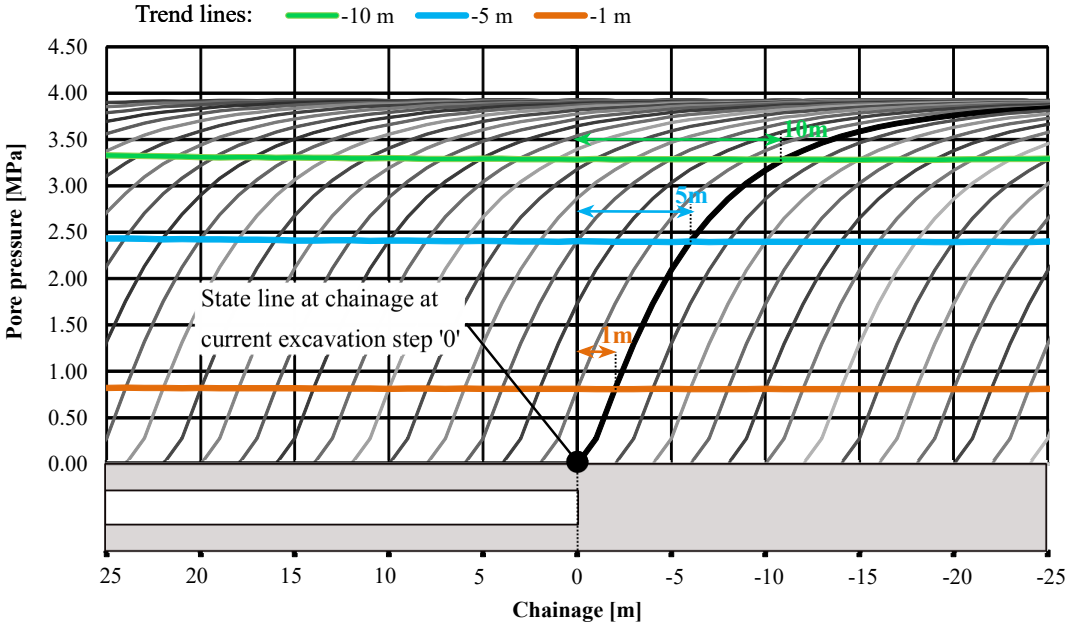

Figure 6.3: Conceptual state and trend line diagram

State lines are obtained by connecting the values of a certain parameter (e.g. displacement component or pore pressure) in a certain measurement position (e.g. crown, sidewall) along the tunnel axis. Trend lines are calculated by connecting the values of each state line at equal distance to the excavation face. Figure 6.3 shows the principle of state and trend line evaluation exemplarily for the pore pressure (in homogeneous rock mass). The grey lines represent the state lines for each excavation step. The coloured lines are the trend lines 10 m, 5 m and 1 m ahead of the tunnel face (the negative sign indicates a chainage ahead of the current face position). This type of data evaluation allows to calculate the (linearised) hydraulic gradients by calculating the pore pressure difference between two adjacent trend lines, divided by the difference of longitudinal distances of the trend lines to the face.

The input parameters of the analyses vary in several dimensions. To allow for comparability, selected parameters are normalized as follows (see Figure 6.4):

- Hydraulic heads are scaled to their initial value h_0 (Equation 6.1).
- The horizontal distance of trend lines is scaled to the tunnel diameter D.
- The distance, at which the maximum hydraulic head occurs within a fault zone to the fault zone start, is scaled to the fault zone width t (Equation 6.2).
- For a qualitative description of the hydraulic head field in heterogeneous rock mass, the distance to the fault zone start, at which the hydraulic head reaches 50 % of the initial value, is determined (Equation 6.4).

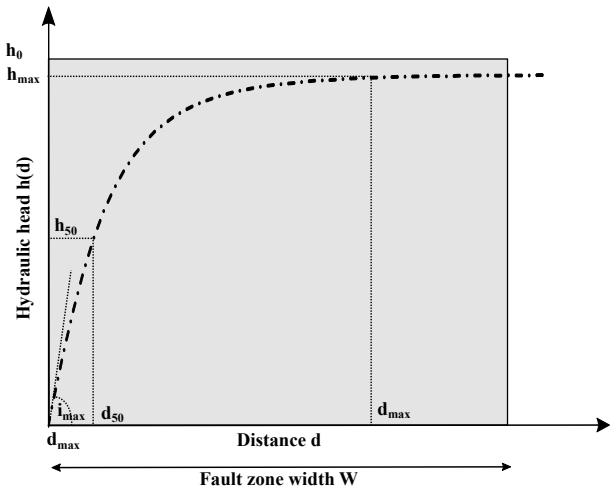

Figure 6.4: Evaluation of normalized values in 1-layer-models

The normalized values are calculated as follows:

$$\text{Normalized max. hydraulic head:} \quad \eta_{max} = \frac{h_{max}}{h_0} \tag{6.1}$$

$$\text{Normalized location of maximum hydraulic head:} \quad \delta_{max} = \frac{d_{max}}{t} \tag{6.2}$$

$$\text{Normalized value of 50 \% hydraulic head:} \quad \eta_{50} = \frac{h_{50}}{h_0} \tag{6.3}$$

$$\text{Normalized location of 50 \% hydraulic head:} \quad \delta_{50} = \frac{d_{50}}{t} \tag{6.4}$$

$$\text{Normalized max. hydraulic gradient:} \quad \iota_{max} = \frac{i_{max}}{h_0} \tag{6.5}$$

$$\text{Normalized location of max. hydraulic gradient:} \quad \delta_{\iota,max} = \frac{d_{i,max}}{t} \tag{6.6}$$

The hydraulic gradient can be calculated from the differential hydraulic head between two adjacent zones, divided by the length of the flow path. Due to the chosen model discretization in longitudinal direction (equal to 1 m), the maximum possible (linearised) hydraulic gradient calculated from the numerical analyses cannot exceed the value of $\frac{h_0}{1m}$.

6.2.3 Scope

The parameters for homogeneous rock mass are limited to the ranges for fault material identified in chapter 5. The calculated models are grouped into four variations (A-D) with respect to their specific influencing factor. The investigated variations are summarized in Table 6.1.

Variation	Hydraulic conductivity [m/s]	Advance rate [m/d]	Tunnel diameter [m]	Initial pore pressure [MPa]
A	varying 10^{-5} - 10^{-10}	fixed	fixed 10	fixed 4
B	fixed 10^{-6} and 10^{-8}	varying 2 - 16	fixed 10	fixed 4
C	fixed 10^{-6} and 10^{-8}	fixed 4	varying 5 - 15	fixed 4
D	fixed 10^{-6} and 10^{-8}	fixed 4	fixed 10	varying 1 - 8

Table 6.1: Scope of fluid flow calculations in homogeneous rock mass

For heterogeneous rock mass, fault zone width is varied between 1 - 20 m. Different settings such as models with one or more layers with varying hydraulic conductivities are investigated to represent settings with a single fault zone, a fault core with adjacent damage zones or a fault zone with multiple core and damage zones (see Figure 5.1). The scope of analyses in heterogeneous rock mass is summarized in Table 6.2.

		High-permeability fault zone	Low-permeability fault zone
Hydraulic conductivity [m/s]	Host rock	10^{-6} - 10^{-10}	10^{-6} - 10^{-8}
	Fault zone	10^{-4} - 10^{-9}	10^{-7} - 10^{-10}
Fault zone width [m]		1 - 20	
Advance rate [m/d]		2 - 8	
Tunnel diameter [m]		5 - 15	
Initial pore pressure [MPa]		4 - 8	

Table 6.2: Scope of fluid flow calculations in heterogeneous rock mass

6.3 Homogeneous rock mass

6.3.1 Parametric study

Figure 6.5 shows the spatial pore pressure distribution around the tunnel face after reaching the steady state for an initial pore pressure of 4 MPa (equal to an initial head of 400 m). Close to the tunnel face the isohypses are almost parallel to the face, whereas with increasing distance they exhibit a bullet shape around the tunnel.

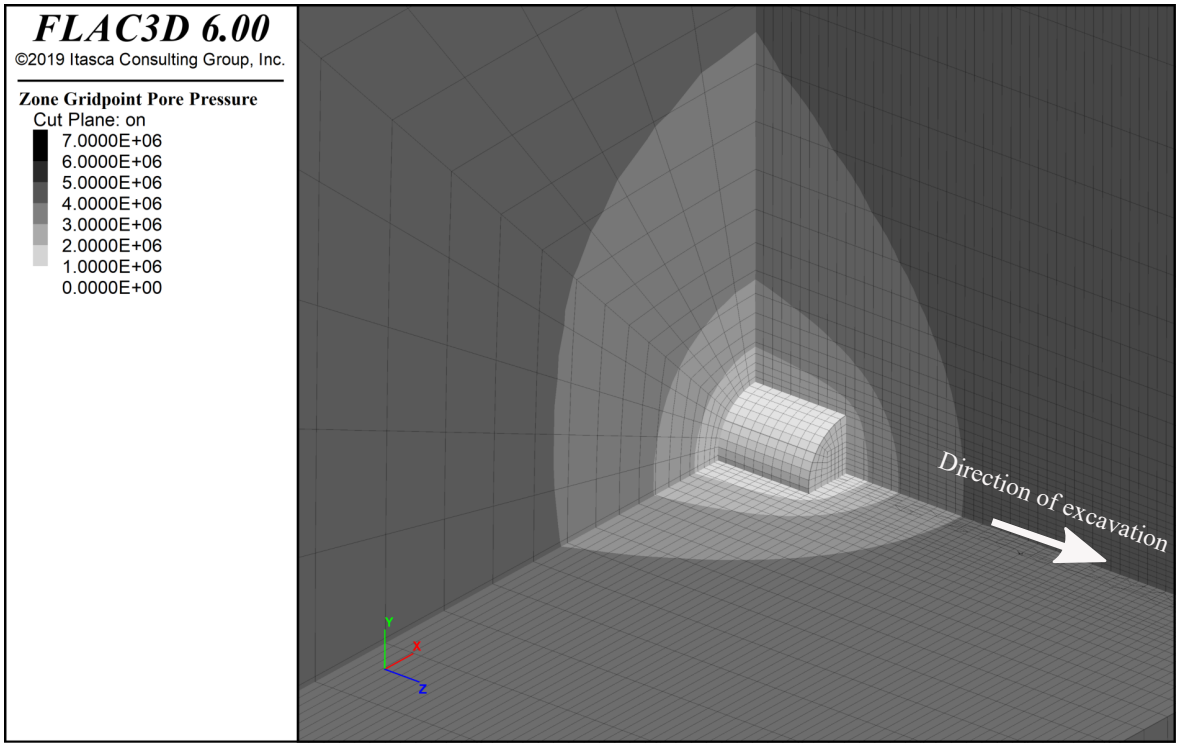

Figure 6.5: Spatial pore pressure distribution in homogeneous rock mass at steady state (initial pore pressure 4 MPa)

The highest hydraulic gradient (represented by the minimum distance between two isohypses) occurs at the intersection of face and lining. At a distance of 1 m to the tunnel, the hydraulic gradient in the intersection of face and lining is approx. twice the gradient at the centre of

the face (tunnel axis). This ratio decreases with increasing distance to the face. At a distance of 0.5 D, the ratio is approx. 1.33. At a distance of 1 D to the tunnel face, the gradient at the centre is equal to the maximum gradient. Although not representing the location of the maximum gradient, the centre point of the tunnel face is used for further data evaluation by two reasons: First, the centre of the face is the most vulnerable part with respect to face stability due to lack of confinement stresses (parallel to the tunnel axis). Second, for evaluation of the hydraulic head field, the spatial orientation of the seepage vector has to be known before starting the calculation, because the locations for data evaluation have to be specified in advance. With respect to symmetry, the seepage vector in the centre of the face is approx. parallel to the tunnel axis (neglecting the impact of gravity and therefore a minimal inclination in the vertical plane).

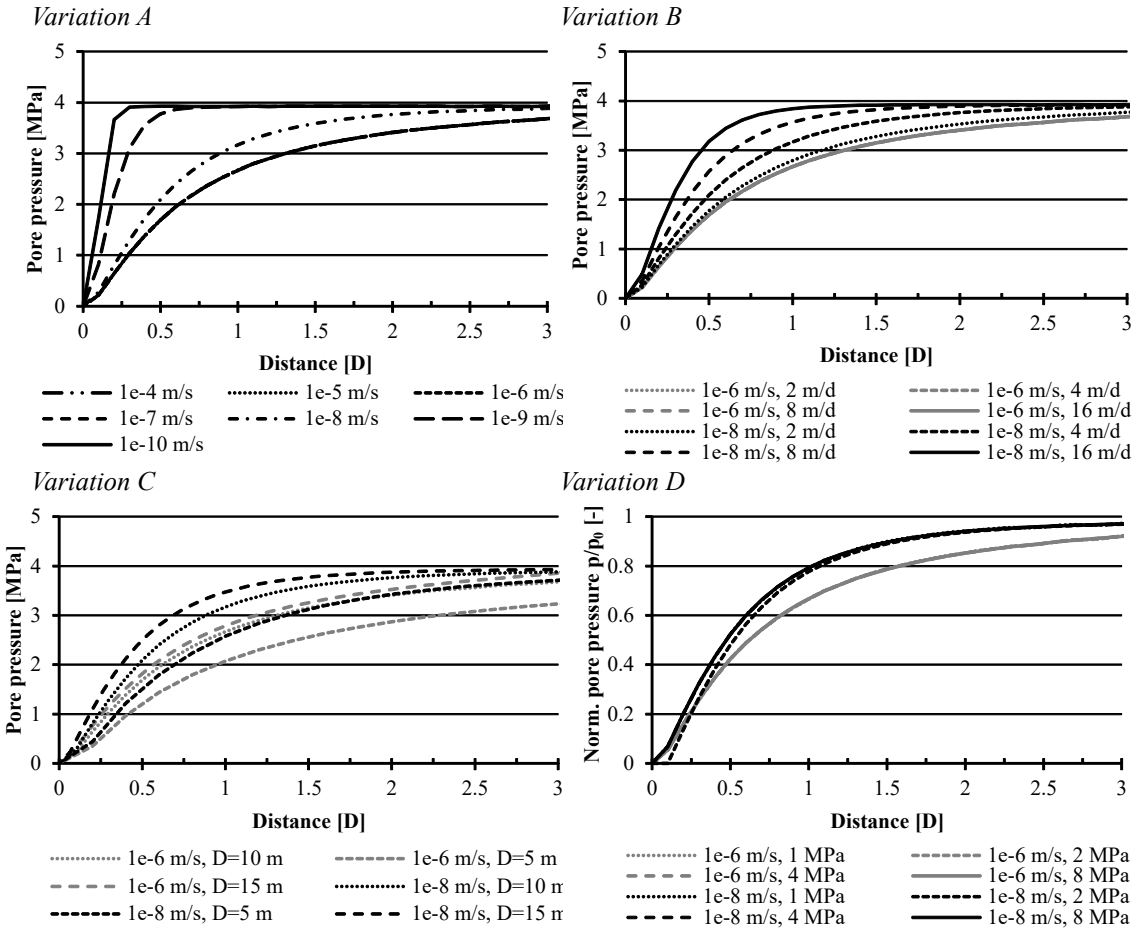

Figure 6.6: Pore pressure distribution ahead of the face at tunnel axis for variations A - D in homogeneous rock mass

Figure 6.6 shows the pore pressure distribution ahead of the face for the variations as per Table 6.1, evaluated at the tunnel axis. The x-axis is scaled to the tunnel diameter D. Figure 6.7 shows a scatter plot of the normalized maximum hydraulic gradients $\iota_{max} = \frac{i_{max}}{h_0}$ at the centre of the tunnel face.

Variation A in Figure 6.6 displays the impact of the rock mass permeability. For hydraulic conductivities $\geq 10^{-7}$ m/s, an identical pore pressure distribution is calculated, because the steady state is reached in these cases. This is in line with the findings of Zingg & Anagnostou (2008) and Perazzelli et al. (2014), who state that the steady state is reached up to hydraulic conductivities $\geq 10^{-8}$ m/s, however assuming an impermeable tunnel lining. In case of a

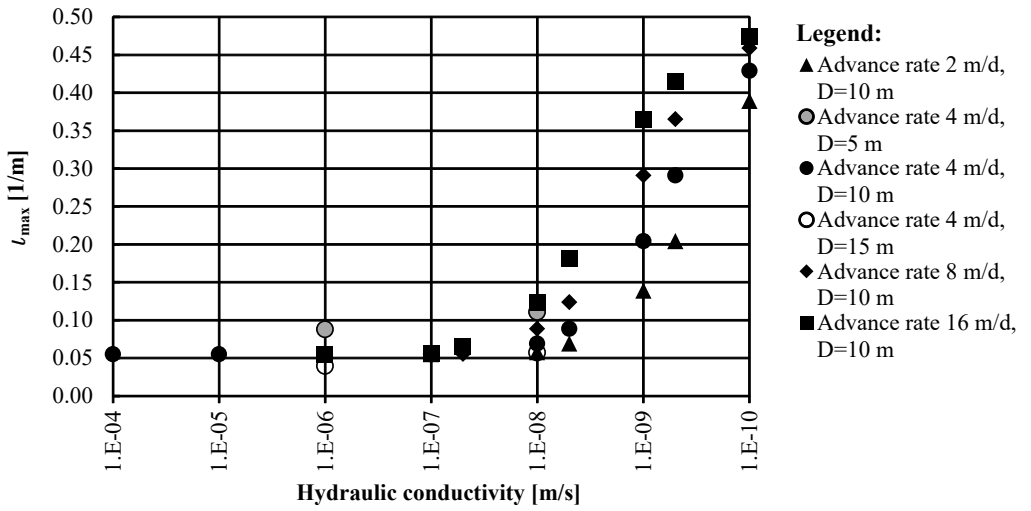

Figure 6.7: Normalized max. hydraulic gradients for homogeneous rock mass

hydraulic conductivity $\leq 10^{-8}$ m/s, a transient state prevails, indicated by the dependence of the hydraulic head field on the permeability.

Variation B shows the impact of the advance rate. For a hydraulic conductivity of 10^{-6} m/s, the advance rate has no effect on the pore pressure distribution, because the steady state is reached in any case, as shown above. For a hydraulic conductivity of 10^{-8} m/s, higher hydraulic heads and gradients occur at higher advance rates (represented by a steeper curve in Figure 6.6). In the latter case, a shorter time frame for drainage is available before excavating the next round. Therefore, less drawdown occurs and the steady state is not reached within one round. Generally speaking, the advance rate influences the hydraulic head field in case of hydraulic conductivities $\leq 10^{-8}$ m/s, as visible from the scatter plot of the normalized hydraulic gradients (Figure 6.7).

The influence of the tunnel diameter is displayed in variation C. Because the horizontal axis is scaled to the tunnel diameter, larger diameters appear to produce steeper hydraulic gradients. However, the actual gradients are higher for small diameters, because less area acts as drainage face in these cases (see Figure 6.7).

Variation D confirms that the initial pore pressure does not affect the shape of the hydraulic head field significantly, independently of the permeability. Consequently, the hydraulic head field is scaled to the initial head for all further considerations.

6.3.2 Estimation of the hydraulic head field

An empirical estimation for the hydraulic head field in homogeneous rock mass was provided by Perazzelli et al. (2014) (see Equation 2.7). This solution was derived assuming an impermeable tunnel lining and applies for steady state conditions only. However, for fault zones with a hydraulic conductivity $\leq 10^{-8}$ m/s a transient state prevails. For a more general application, the equation for the hydraulic head ahead of the face is modified by introducing the parameters K^* and D^*:

$$h(x) = (1 - e^{-K^* \cdot D^* \cdot x}) \cdot h_0 \tag{6.7}$$

where: $h(x)$ = Hydraulic head at distance x to the face [m]
K^* = Curve fitting parameter for hydraulic conductivity and advance rate (Fig. 6.8) [-]
D^* = Curve fitting parameter for tunnel diameter (Eq. 6.8) [-]
x = Horizontal distance to the tunnel face [m]
h_0 = Initial hydraulic head [m]

The parameters K^* and D^* are determined by fitting the approximation function (Equation 6.7) to the results of the numerical analyses using the method of least squares. The value of K^* can be evaluated from Figure 6.8.

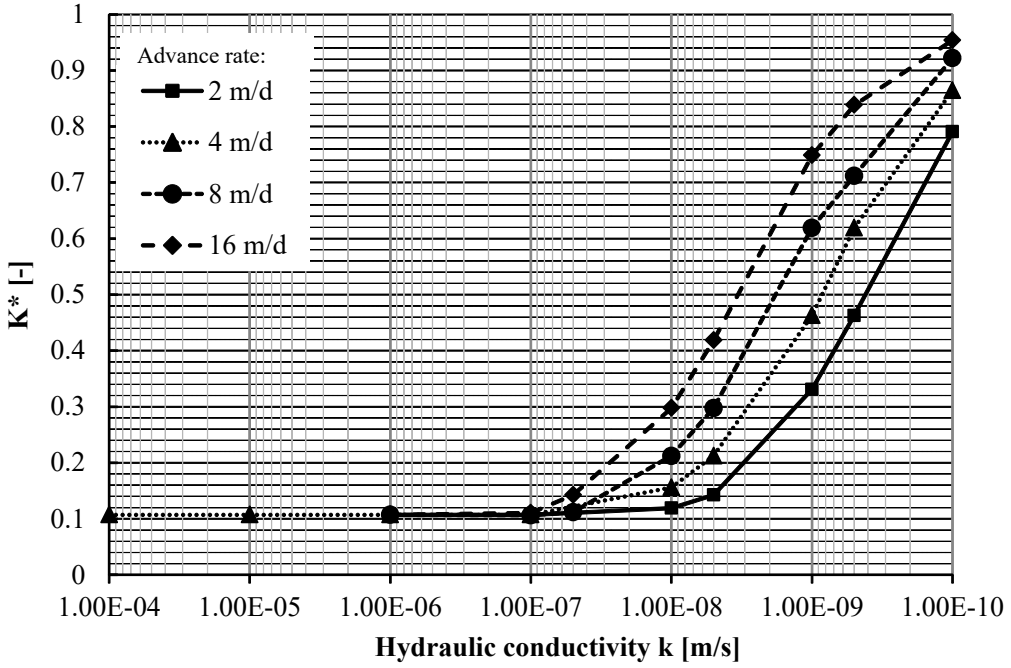

Figure 6.8: Parameter K^* for various hydraulic conductivities and advance rates

For parameter D^*, a linear regression is assumed between the values calculated for selected tunnel diameters (shown in Figure 6.9). This assumption disregards that the area of the tunnel face actually depends on the second power of the radius. However, as the area of the face is small compared to the area of the lining, this approximation can be justified. The value of D^* is calculated from the tunnel diameter D according to Equation 6.8.

$$D^* = -0.0431 \cdot D + 1.446 \tag{6.8}$$

The maximum hydraulic gradient i_{max} can be calculated by differentiating Equation 6.7 with respect to x at position $x = 0$ (i.e. at the face):

$$i_{max} = K^* \cdot D^* \cdot h_0 \tag{6.9}$$

A comparison between the hydraulic heads obtained in the numerical analyses and the approximation function for selected hydraulic conductivities is provided in Figure 6.10. The quality of the analytical solution is represented by the sum of squares (SQ). The approximation function according to Equation 6.7 gives a good estimate of the hydraulic head field in case of high to medium permeabilities ($k \geq 10^{-8}$ m/s). In case of low permeabilities, the hydraulic head close to the face is slightly underestimated.

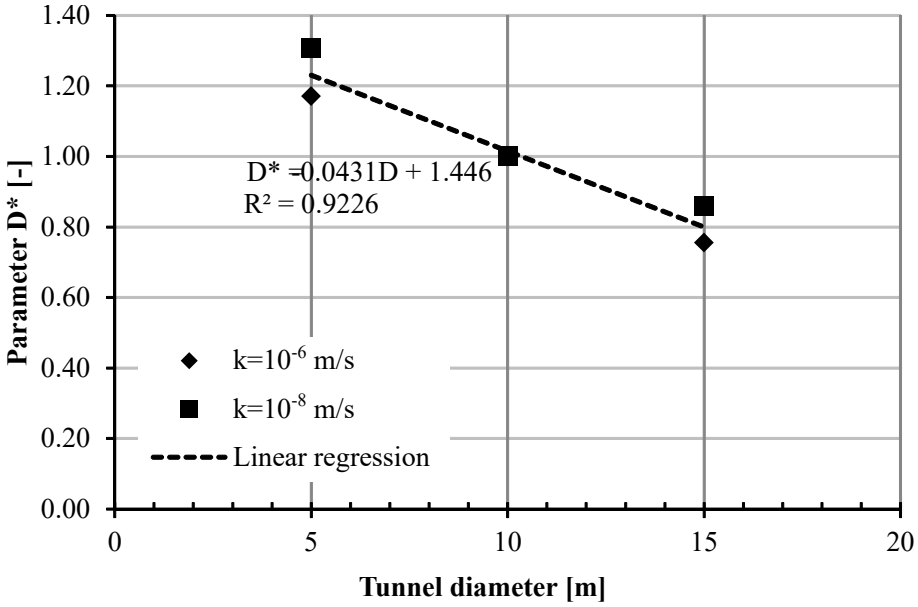

Figure 6.9: Parameter D^* as a function of the tunnel diameter

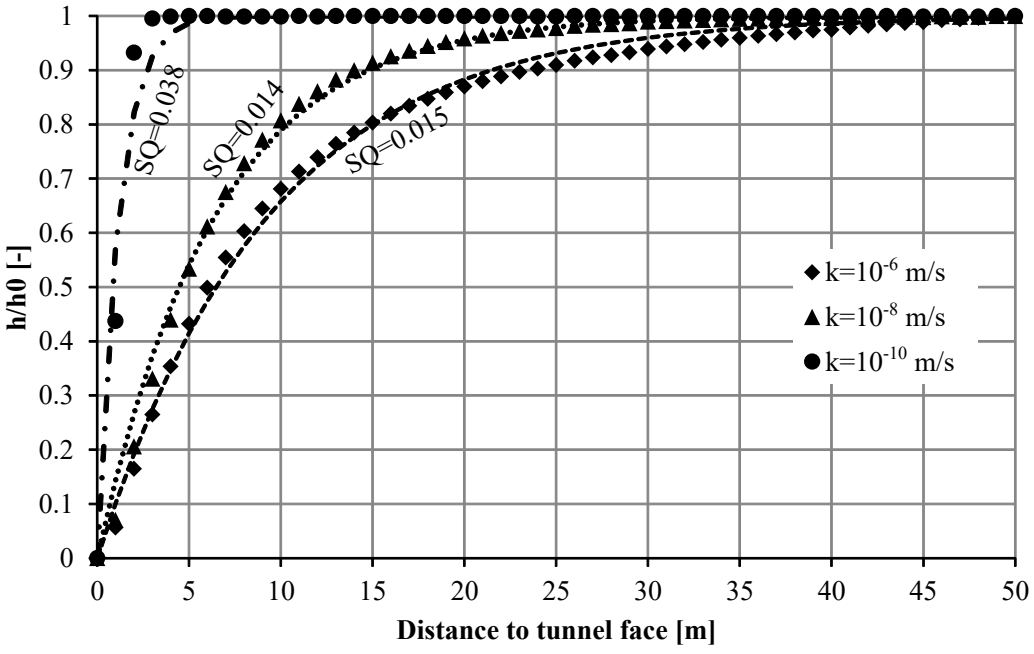

Figure 6.10: Comparison of hydraulic head ahead of the tunnel face for selected hydraulic conductivities, tunnel diameter D = 10 m, advance rate 4 m/d: results from numerical analyses (markers) and analytical approximation function (lines)

6.4 Heterogeneous rock mass

6.4.1 Parametric study

The spatial distribution of the pore pressure in vicinity of the tunnel face when reaching a low-permeability fault zone with a width of 10 m oriented perpendicular to the tunnel axis is shown in Figure 6.11. The results are based on a permeability contrast of two orders of magnitude between fault rock and host rock and an initial pore pressure of 4 MPa. While the isohypses of the pore pressure show a bullet shape in homogeneous rock mass (see Figure 6.5), they are distorted by the fault zone in case of heterogeneous rock mass. As shown in Figure 6.11, the isohypses ahead of the face are oriented almost parallel to the fault zone. At the time of reaching the fault zone, the pore pressure at a distance of 0.5 D to the tunnel face remains almost at its initial value.

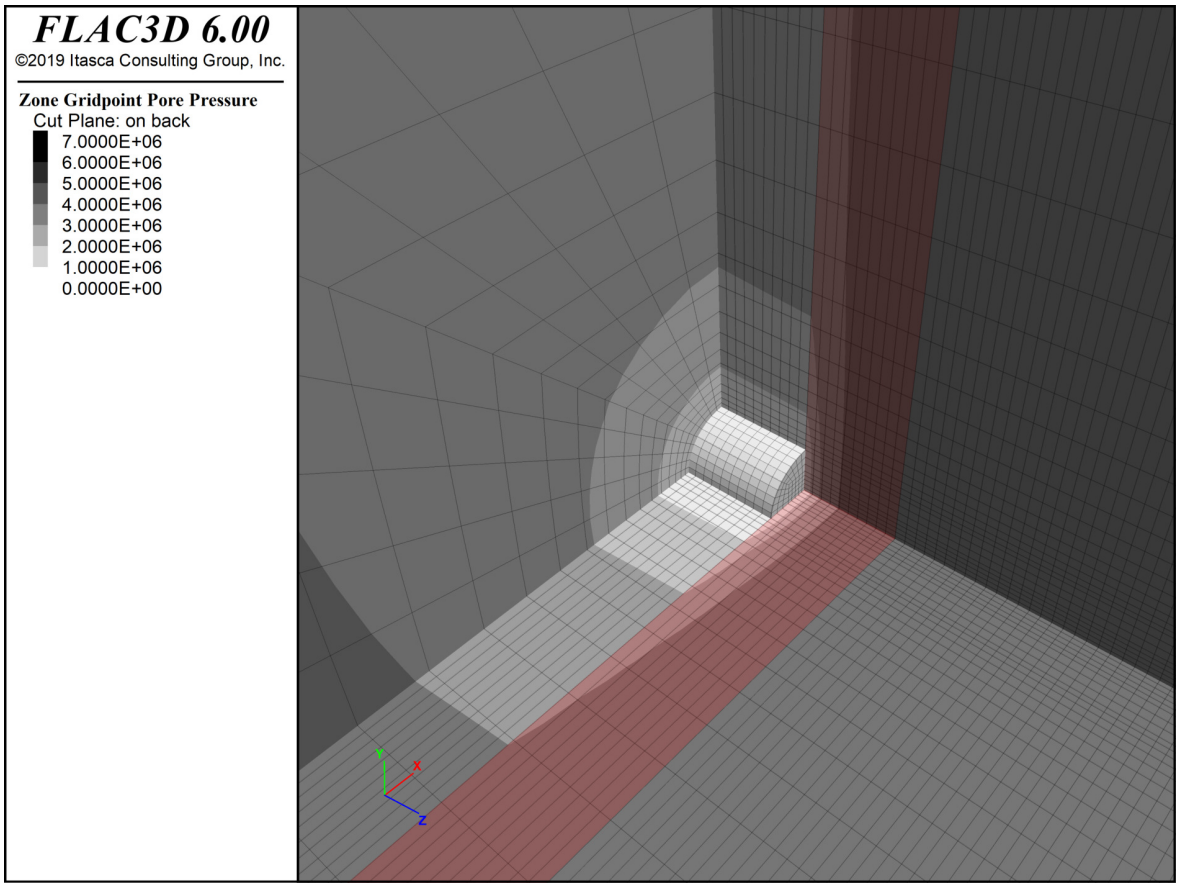

Figure 6.11: Spatial pore pressure distribution in heterogeneous rock mass when reaching a fault zone with low permeability (red shade, initial pore pressure 4 MPa)

The distribution of the hydraulic heads along the tunnel axis is exemplarily displayed in a state and trend line plot (Figure 6.12) for both, fault zones with low and high permeability. Both cases refer to a permeability contrast of two orders of magnitude, a fault zone width of 10 m and an initial pore pressure of 4 MPa.

When the fault zone exhibits a lower permeability than the host rock (low-permeability fault zone LPFZ), hydraulic gradients (represented by the trend lines of pore pressure) decrease when the excavation approaches the fault zone, because re-charge to this region is hindered by the low permeability of the fault (Leitner & Müller, 2007). In other words, the fault zone acts as an aquiclude. As soon as the fault zone is reached (chainage 0), hydraulic gradients

a) Low-permeability fault zone

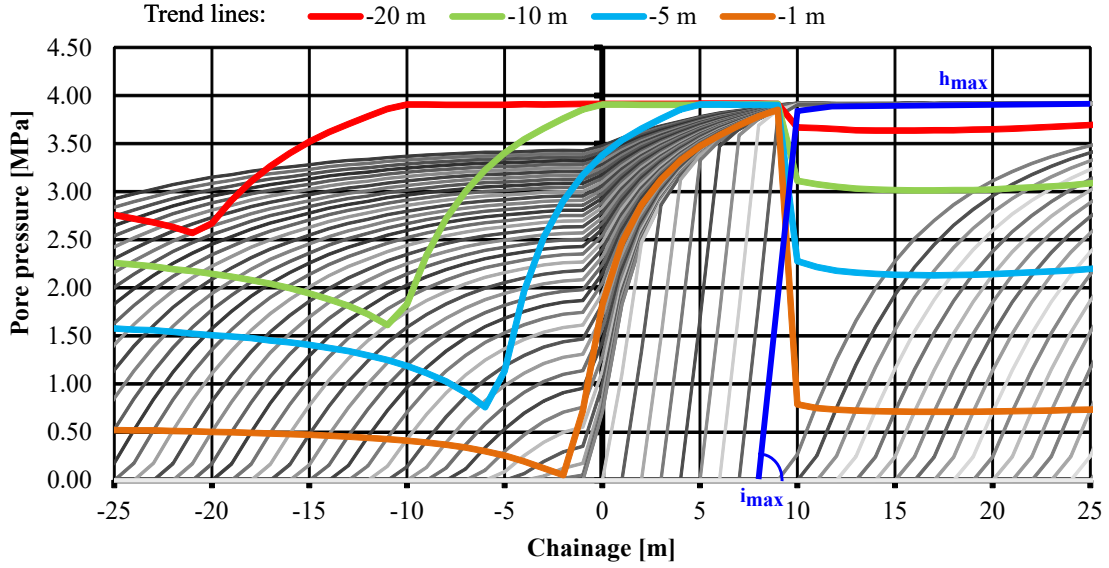

b) High-permeability fault zone

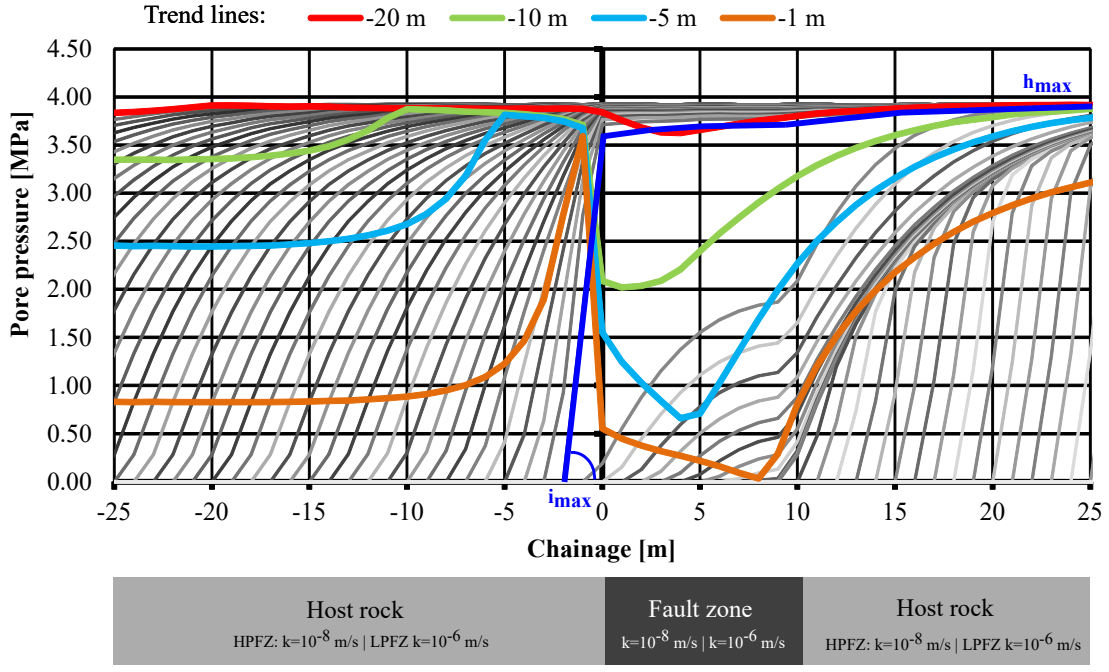

Figure 6.12: State and trend lines of pore pressure for a fault zone width of 10 m, a): $k = 10^{-6}$ m/s (host rock) and $k = 10^{-8}$ m/s (fault zone); b): $k = 10^{-8}$ m/s (host rock) and $k = 10^{-6}$ m/s (fault zone); Abbreviations: HPFZ...high-permeability fault zone; LPFZ...low-permeability fault zone

increase significantly and reach their maximum (i_{max}) at the transition to the more permeable host rock behind the fault. The pore pressure at the time of leaving the fault zone (chainage 10) is 97 % of the initial value. The pore pressure distribution immediately before re-entering the host rock, representing the maximum hydraulic gradient, is indicated by the state line in dark blue.

In case of a high-permeability fault zone (HPFZ), the longitudinal distribution of hydraulic heads is more or less contrary. Hydraulic gradients increase towards the fault zone, because drawdown is compensated by re-charge from the fault zone. The maximum gradient (i_{max}) occurs at the start of the fault zone (indicated by the dark blue state line), while the gradients within the fault zone are significantly lower, since the initially high gradients are quickly equalized by seepage. The pore pressure in the fault zone in this case is approx. 90 % of the initial value.

With respect to the differences in the position of the maximum hydraulic gradient and the pore pressure distribution within the fault zone, a consequent distinction in data evaluation is made between LPFZ and HPFZ. For assessing tunnel stability, the maximum hydraulic head in the fault zone and the maximum hydraulic gradient are of particular interest. To reduce the amount of data to be analysed, the displayed results are limited to the maximum hydraulic gradients. Due to discretization of the numerical model in longitudinal direction (1 m), the maximum hydraulic gradient i_{max} and the maximum hydraulic head h_{max} are equal to the maximum value of the trend line '-1 m'.

To allow for comparability of different fault zone widths and varying hydraulic conductivities, the normalized maximum hydraulic gradient is plotted as a function of the transmissivity (T) of the fault zone (Figure 6.13). The transmissivity describes the flow quantity through a layer with a width W and a hydraulic conductivity k for a hydraulic gradient of 1: $T = k \cdot W$ (Prinz & Strauss, 2011).

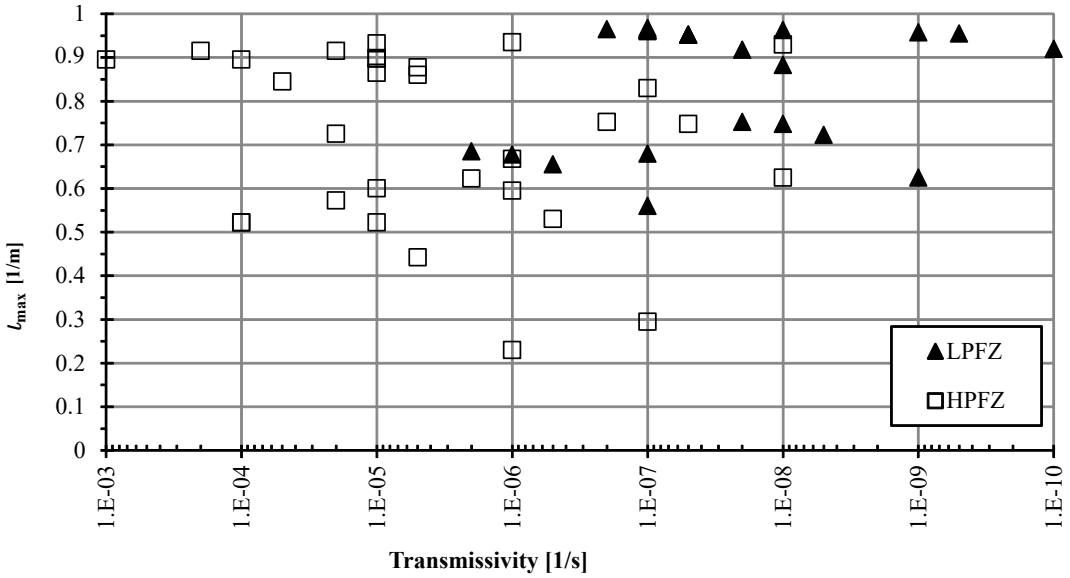

Figure 6.13: Normalized max. hydraulic gradient versus transmissivity of fault zone in heterogeneous rock mass

The normalized hydraulic gradients in heterogeneous rock mass are significantly higher than in homogeneous rock mass (< 0.5, see Figure 6.7) for the majority of the investigated parameter sets. A reasonable correlation of the gradient to the transmissivity cannot be identified.

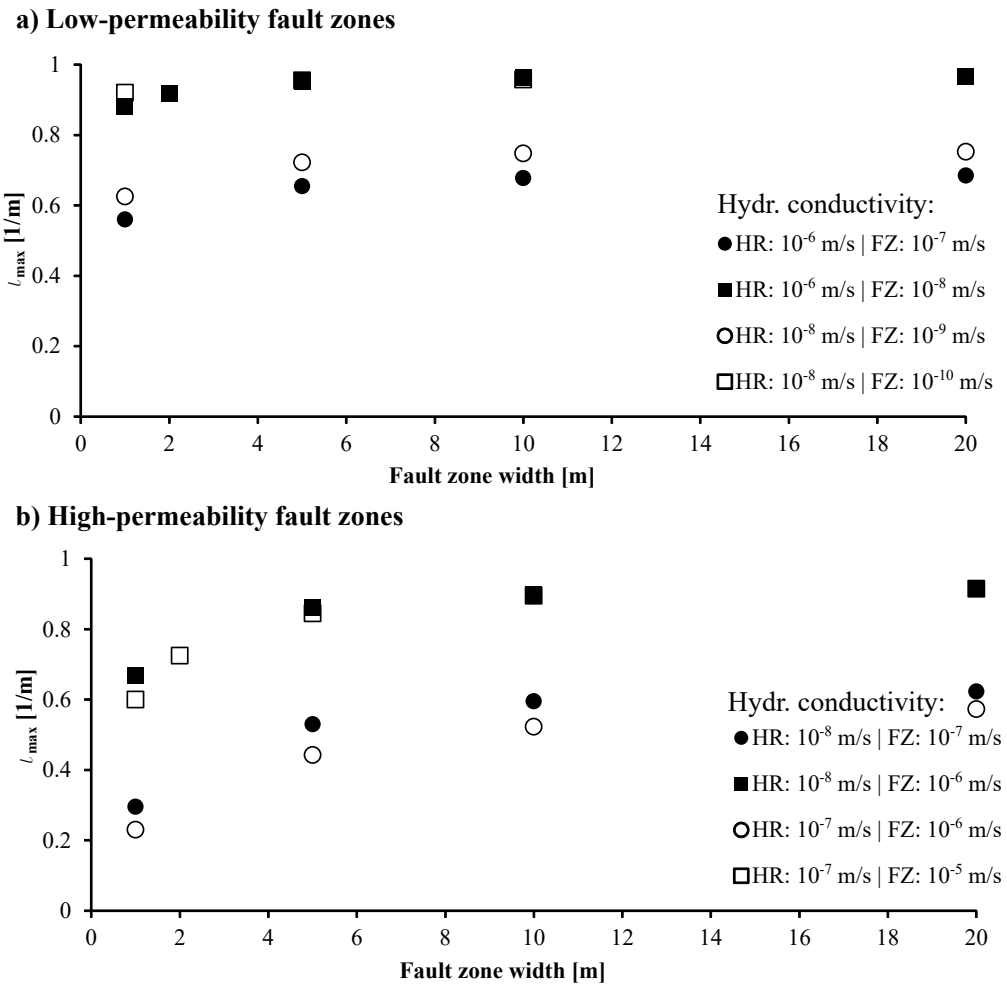

Figure 6.14: Normalized max. hydraulic gradient versus fault zone width for selected low- (a) and high- (b) permeability fault zones; Abbreviations: HR...host rock; FZ...fault zone

When plotting the normalized hydraulic gradients against the fault zone width, an increase of the maximum gradient with increasing fault zone width and hydraulic contrast (i.e. permeability contrast between host rock and fault zone) can be observed (Figure 6.14). In both cases (LPFZ and HPFZ), not much further increase of the hydraulic gradient occurs for a width of > 5 m independently of the hydraulic contrast. In case of a hydraulic contrast of one order of magnitude, the maximum hydraulic gradients reach values of approx. 0.6 (HPFZ) to 0.75 (LPFZ). At a hydraulic contrast of two orders of magnitude, the maximum hydraulic gradients reach 0.9 or higher for fault zones wider than 5 m.

To investigate the influence of the actual permeability, the maximum hydraulic gradients are plotted against the hydraulic conductivity of the host rock (Figure 6.15). In case of a hydraulic contrast of two orders of magnitude, the maximum hydraulic gradient reaches a value of 0.9, independent of the host rock conductivity. At a lower hydraulic contrast, the maximum hydraulic gradient increases with decreasing permeability, both in case of LPFZ and of HPFZ.

The conducted sensitivity analysis additionally targets the influence of initial pore pressure, advance rate and tunnel diameter. Similar to homogeneous rock mass, the initial pore pres-

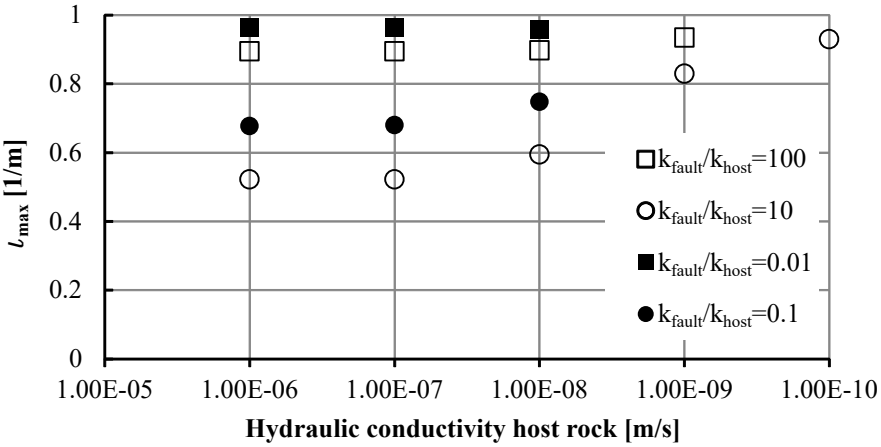

Figure 6.15: Normalized max. hydraulic gradient versus hydraulic conductivity of the host rock for low-permeability fault zones (filled markers) and high-permeability fault zones (hollow markers)

sure has no significant impact on the hydraulic head field. A corresponding plot is omitted in this case. In other words, the hydraulic head field can be scaled to the initial value. The influence of a change of advance rate is shown in Figure 6.16a. The difference in the normalized hydraulic head when doubling the advance rate from 4 m/d to 8 m/d is in the range of 2 %. Consequently, the impact of advance rate is not investigated further. The variation of the tunnel diameter shows that the maximum gradient decreases with increasing tunnel diameter (Figure 6.16b), similar to homogeneous rock mass.

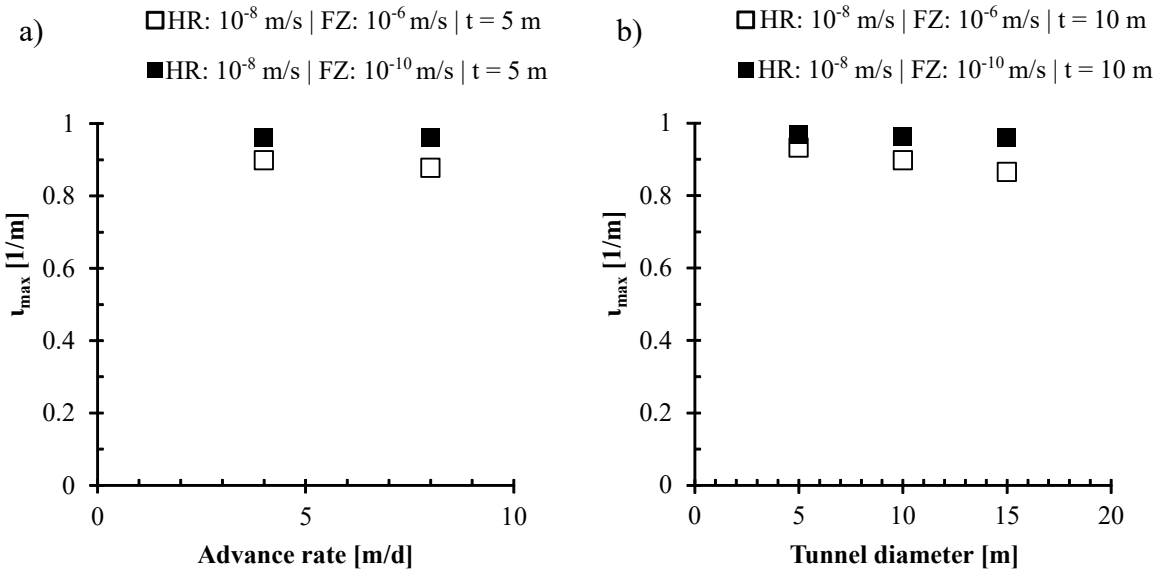

Figure 6.16: Normalized max. hydraulic gradient versus advance rate (a) and tunnel diameter (b); Abbreviations: HR...host rock; FZ...fault zone

From the evaluations presented above, a priority list of influencing factors on the hydraulic head field in heterogeneous rock mass is established:

1. *Hydraulic contrast:* The hydraulic contrast (permeability contrast) between fault zone and host rock essentially controls the hydraulic head field. A contrast of two orders of

magnitude or higher yields a hydraulic head of at least 2/3 of the initial value head at a distance of 1 m to the face, increasing with fault zone width.

2. *Fault zone width:* The hydraulic gradient shows an approximately logarithmic dependence on the fault zone width. Even for fault zones with a width of 1 m, the resulting hydraulic gradients are still significantly higher than in homogeneous rock mass.
3. *Host rock permeability:* The maximum hydraulic gradient increases with decreasing host rock permeability.
4. The influence of advance rate and tunnel diameter is of low significance compared to items 1 - 3.
5. The initial hydraulic head does not influence the distribution of the hydraulic head.

Generally speaking, the calculations show that even in case of a thin fault zone, the hydraulic head in or behind the fault zone can be close to the initial value, provided the hydraulic contrast is large enough. With respect to the uncertainties remaining in the geological-hydrogeological model and the parameter determination, such situations may remain undetected even in case of thorough site investigation. From an engineering point of view it is therefore advisable to consider the initial hydraulic head within (HPFZ) or behind (LPFZ) the fault zone for stability analyses, unless sufficiently detailed knowledge on permeabilities and fault zone architecture is available.

6.4.2 Multi-layer fault zones

With respect to the influence of the hydraulic contrast, the findings above derived for a fault zone consisting of one single layer are tested in a model consisting of a sequence of high- and low-permeability zones. The model consists of host rock with a hydraulic conductivity of $k = 10^{-8}$ m/s, a damage zone with increased hydraulic conductivity ($k = 10^{-6}$ m/s) and a width of 4 m, a fault core with low hydraulic conductivity ($k = 10^{-9}$ m/s) and a thickness of 2 m, and finally a second damage zone with similar parameters as the first one.

The distribution of the hydraulic heads along the tunnel axis is shown in a state and trend line diagram in Figure 6.17. The analysis confirms the findings elaborated above. When reaching the first high-permeability damage zone (chainage -4), the hydraulic head is approximately 85 % of the initial head. After entering the damage zone, the initially high heads are equalized by seepage and comparatively low hydraulic gradients occur until the excavation reaches the fault core (chainage 0). The hydraulic head at this point is approx. 70 % of the initial head. Within the low-permeability fault core, hydraulic gradients increase gradually. At the transition from fault core to damage zone (chainage 6), the maximum hydraulic head and gradients occur, because drawdown in advance is hindered by the fault core and this region is continuously re-charged by the high permeability damage zone behind. When leaving the fault zone, the hydraulic head is approximately 95 % of the initial head. With respect to the typical permeability distribution in fault zones (see chapter 2, Figure 2.5), it becomes obvious that hydraulic heads in the same range as the initial groundwater level and corresponding hydraulic gradients may occur in heterogeneous conditions (at least locally), even if the extent of the fault zones is limited.

6.4.3 Estimation of the hydraulic head field

According to the findings described above, a function for estimating the hydraulic head should at least incorporate the impact of hydraulic contrast and the fault zone width. Host rock

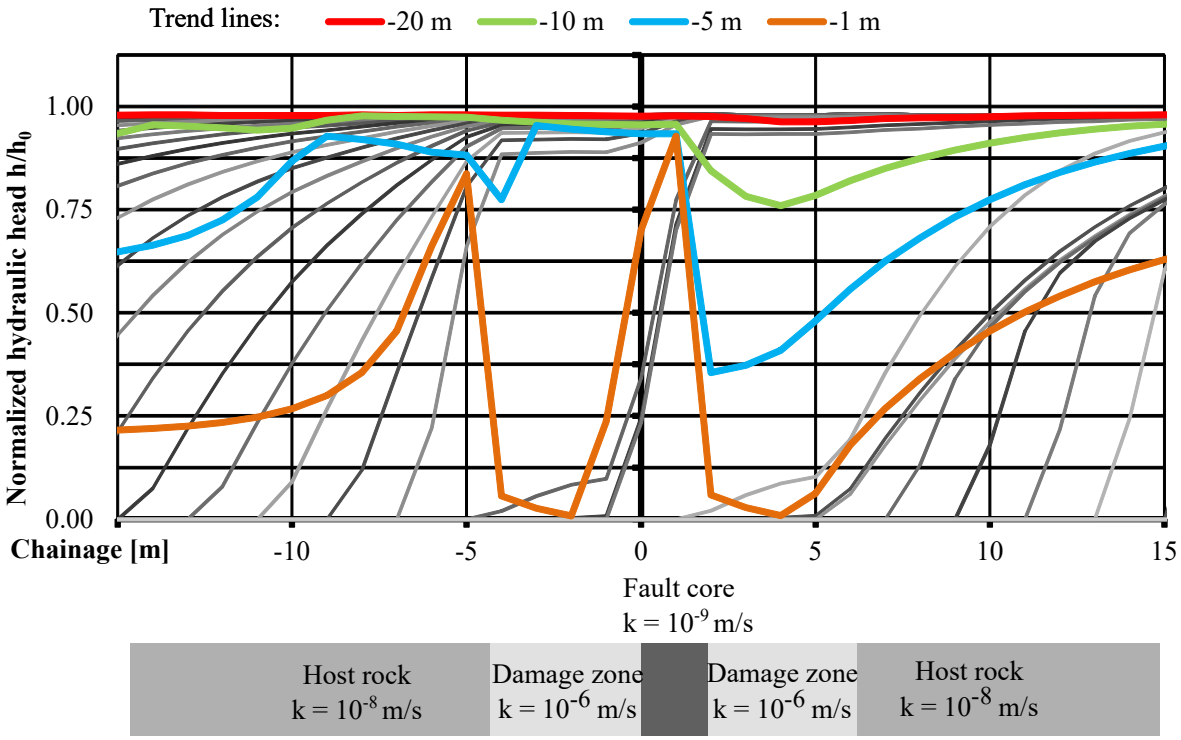

Figure 6.17: State and trend line diagram of nomralized hydraulic head for a model consisting of a low-permeability fault core and two adjacent damage zones with increased permeability

permeability is of comparatively low significance and may therefore be neglected for sake of simplicity. For the same reason, impacts of advance rate and tunnel geometry are not considered.

With respect to tunnel stability, the transition from host rock to fault zone (HPFZ) and from fault zone to host rock (LPFZ) represent the most critical situations, because the maximum hydraulic gradients and inflow rates occur in these sections. The approximation function should allow for an estimation of the hydraulic heads ahead of the face at these stages. A bi-linear function (as indicated in Figure 6.12) is used to describe the hydraulic head field: the hydraulic head increases linearly from atmospheric pressure to h_{max} over a longitudinal distance of 1 m (as modelled in the numerical analyses) and than remains on a constant level. The dependence on the fault zone width is considered by an exponential function as follows:

$$h_{max} = i_{max} = h_0 \cdot A \cdot (1 - e^{-B \cdot t}) \tag{6.10}$$

where: h_{max} = Maximum hydraulic head in / behind fault zone [m]
i_{max} = Maximum hydraulic gradient [-]
h_0 = Initial hydraulic head [m]
A, B = Curve fitting parameters acc. to Table 6.3 [-]
t = width of fault zone [m]

The fitting parameters A and B are determined by a least squares fit of the approximation function to the results of the numerical calculations (see Figure 6.18). To obtain estimates on the safe side, the least squares fit is applied to the cases of minimum investigated host

rock conductivity ($k = 10^{-8}$ m/s), because these cases yield higher hydraulic gradients. The calculated fitting parameters A and B are summarized in Table 6.3.

a) Low -permeability fault zones

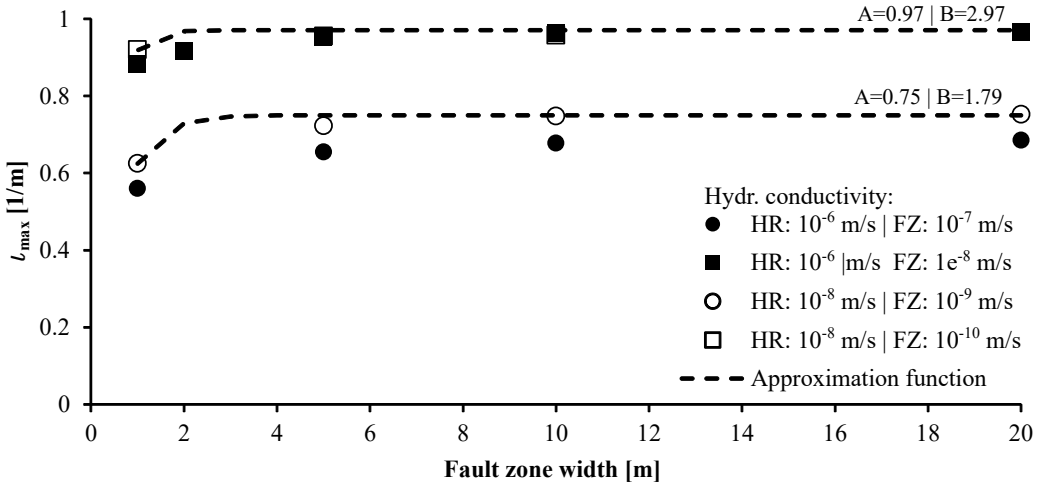

b) High-permeability fault zones

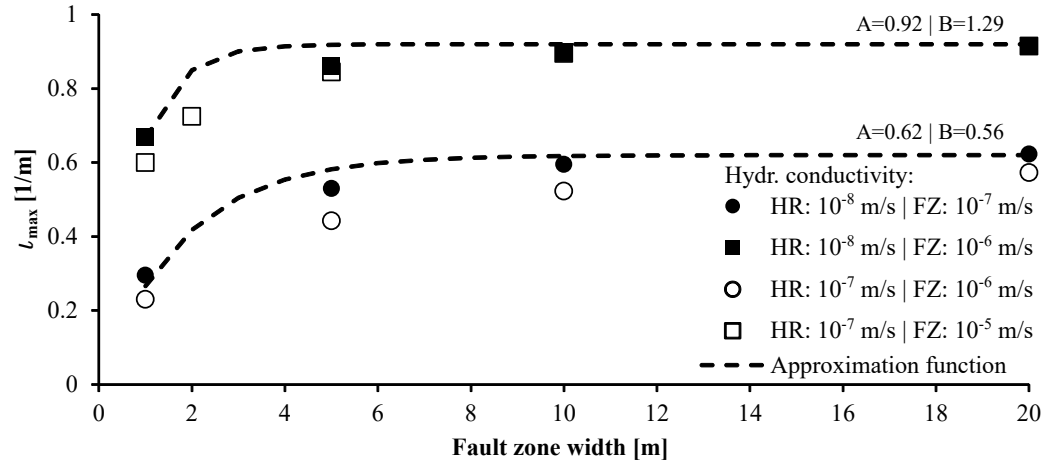

Figure 6.18: Normalized maximum gradient for low-permeability (a) and high-permeability (b) fault zones; Abbreviations: HR...host rock; FZ...fault zone

A comparison between the results of the numerical analyses and the approximation function (Equation 6.10) is provided in Figure 6.19. Exemplarily, the results for a tunnel diameter of 10 m and a fault zone thickness of 10 m are displayed. The horizontal axis is normalized by the tunnel diameter. For the HPFZ, the hydraulic head field immediately before entering the fault zone is shown. For the LPFZ, the comparison is done at the transition to the host rock. In case of a hydraulic contrast of two orders of magnitude (or higher), the assumption of a uniform distribution of the hydraulic head agrees well with the results from the numerical analyses for both, HPFZ and LPFZ. For lower hydraulic contrasts, the hydraulic head depends on the distance to the face. Therefore, the actual hydraulic heads deviate significantly from the assumption of a uniform distribution, as postulated in the approximation function. Close to the face, hydraulic heads are therefore overestimated, whereas at a distance to the face of 0.3 D or higher, the actual hydraulic head exceeds the value given by the approximation function. The differences between actual hydraulic heads and approximation function can be traced

	Low-permeability fault zone		High-permeability fault zone	
permeability contrast k_{fault}/k_{host}	≤ 0.01	0.1	10	≥ 100
A	0.97	0.75	0.62	0.92
B	2.97	1.79	0.56	1.29

Table 6.3: Fitting parameters for approximation function in heterogeneous rock mass

back to the influence of host rock permeability and the dependence of the hydraulic head on the distance to the transition, which are not considered in the approximation function. A statistical qualification of the approximation function is omitted in this case as the deviations are evident from Figure 6.19. The proposed approximation function can only provide a rough estimate of the hydraulic head. From an engineering point of view, results at the most crucial point (i.e. the transition to more permeable rock mass) are on the safe side, since the hydraulic heads close to the face are overestimated. Therefore, this approximation may act as basis for stability assessment in cases, where the hydraulic parameters of fault and host rock as well as the extent of the fault zone are sufficiently known. In any other case, the assumption of the initial hydraulic head acting at the transition to more permeable rock mass represents a reasonably conservative approach.

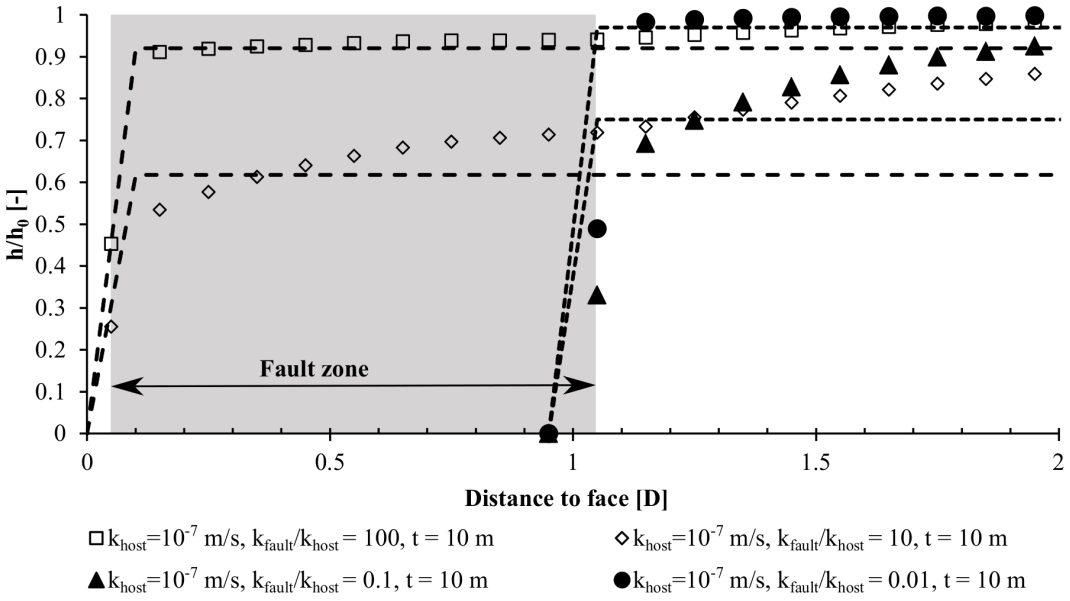

Figure 6.19: Comparison of hydraulic head field from numerical analyses (markers) and approximation functions (dashed lines)

6.4.4 Impact of fault zone orientation

All results presented above refer to a fault zone striking perpendicular to the tunnel axis and dipping vertically. To investigate the influence of fault zone orientation, an additional calculation is performed for a fault zone with a thickness of 10 m, crossing the tunnel axis at 45^o and dipping vertically. The conductivities are $k = 10^{-8}$ m/s for the host rock and $k = 10^{-6}$ m/s for the fault zone. The tunnel diameter is 10 m and the initial pore pressure is taken as 4 MPa.

A comparison of the pore pressure distribution for a fault zone perpendicular to the tunnel axis and for a fault zone crossing the tunnel axis in acute angle is displayed in Figure 6.20.

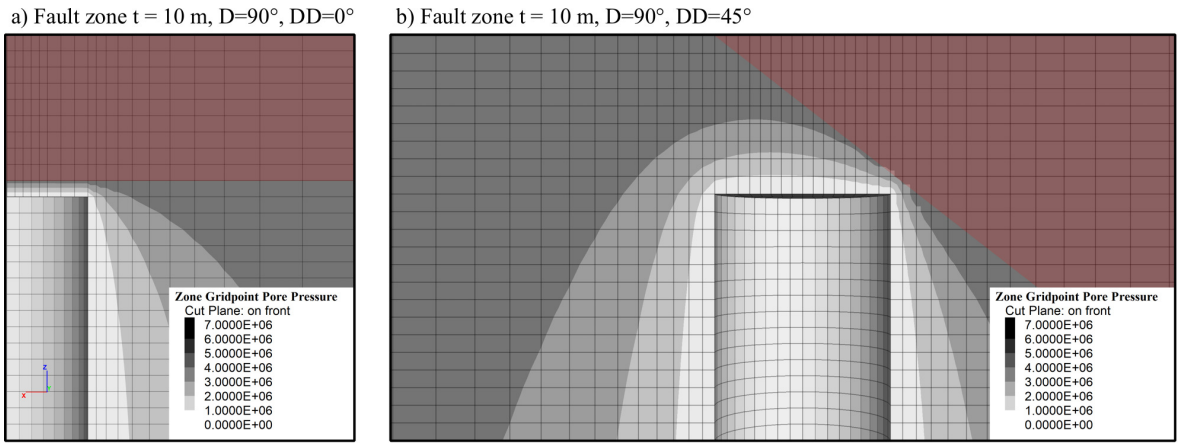

Figure 6.20: Pore pressure distribution [Pa] 1 m ahead of fault zone for fault zone orientation perpendicular to tunnel axis (a) and 45° to tunnel axis (b), initial pore pressure 4 MPa; abbreviations: t...thickness; D...dip angle; DD...dip direction

The fault zone crossing in acute angle (Figure 6.20b) causes a distortion of the hydraulic head field, yielding steeper hydraulic gradients close to the right sidewall, where the tunnel drive encounters the fault zone first. However, the maximum hydraulic gradient and the maximum head in the fault zone, prevailing just before reaching the fault zone, are similar in both cases (a and b). In case of a lower hydraulic contrast and high-permeability host rock, fault zone orientation may have a greater influence on the maximum hydraulic gradient. The hydraulic gradients at the right sidewall in this case can equalize by seepage more easily, leading to more drawdown within the fault zone before actually reaching it. Consequently, hydraulic gradients when reaching the fault zone are lower and more favourable. For all further considerations within this thesis, the more unfavourable case of a fault zone oriented perpendicular to the tunnel axis is presumed.

6.4.5 Impact of anisotropic permeability

Depending on the lithology and the genesis of a fault zone, subsequent shearing and associated rotation of grains along deformation bands can introduce hydraulic anisotropy (Bense et al., 2013; Faulkner et al., 2010; Winkler et al., 2010). The impact of anisotropic permeability is studied in a representative example consisting of a low-permeability fault zone (t = 10 m) and a tunnel with a diameter of 10 m. Hydraulic conductivity of the fault zone is $k = 10^{-6}$ m/s parallel to the fault zone and $k = 10^{-8}$ m/s perpendicular to the fault zone. Hydraulic conductivity of the host rock is $k = 10^{-6}$ m/s. Figure 6.21 shows the trend line 1 m ahead of the face (identical with the maximum hydraulic gradient) when tunnelling through the fault zone for both, isotropic (black) and anisotropic (red) permeability. When reaching the fault zone with anisotropic permeability, hydraulic gradients are approx. 45 % higher compared to isotropic permeability. The higher permeability parallel to the fault zone impedes drawdown ahead of the fault. Rather, the fault zone is re-charged from lateral areas due to the high permeability in this direction. Within the fault zone, the high hydraulic gradients are equalized quickly by seepage parallel to the fault. Towards the end of the fault zone, the gradients increase again, because the head field is essentially controlled by the high-permeability host rock behind. At the transition to the host rock, the hydraulic gradient is similar to the case of isotropic permeability. For assessing tunnel stability, this is the most critical point, as elaborated previously. Since similar gradients occur in this section in case of isotropic and anisotropic permeability, anisotropic permeability is not further investigated within this

thesis.

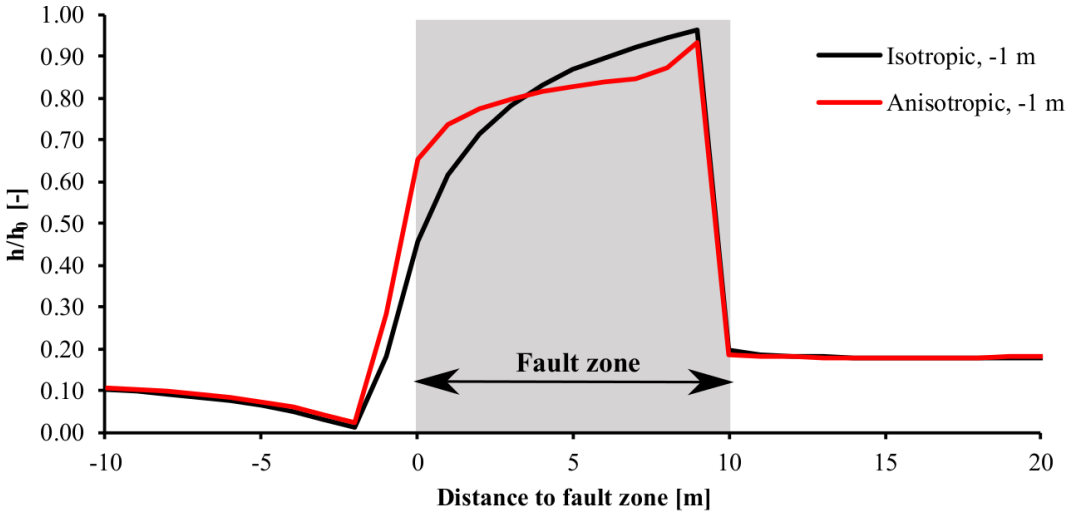

Figure 6.21: Trend line for normalized hydraulic heads 1 m ahead of the face for fault zones with isotropic (black) and anisotropic (red) permeability

6.5 Impact of excavation damage zone

All investigations presented above consider a constant permeability of the rock mass throughout model time. However, as practical experience shows, tunnel excavation can affect the permeability close to the tunnel, as described in chapter 5. The zone with increased permeability is referred to as excavation damage zone (EDZ). To qualitatively study the impact of the EDZ on the hydraulic head field, an increase of 1 - 2 orders of magnitude in permeability is considered in the calculations. The extent of the EDZ is modelled with 2 m, both in radial direction and ahead of the face. An exemplary plot of the hydraulic conductivities when considering the EDZ is shown in Figure 6.22. In total, six calculations considering an EDZ are performed (see Table 6.4).

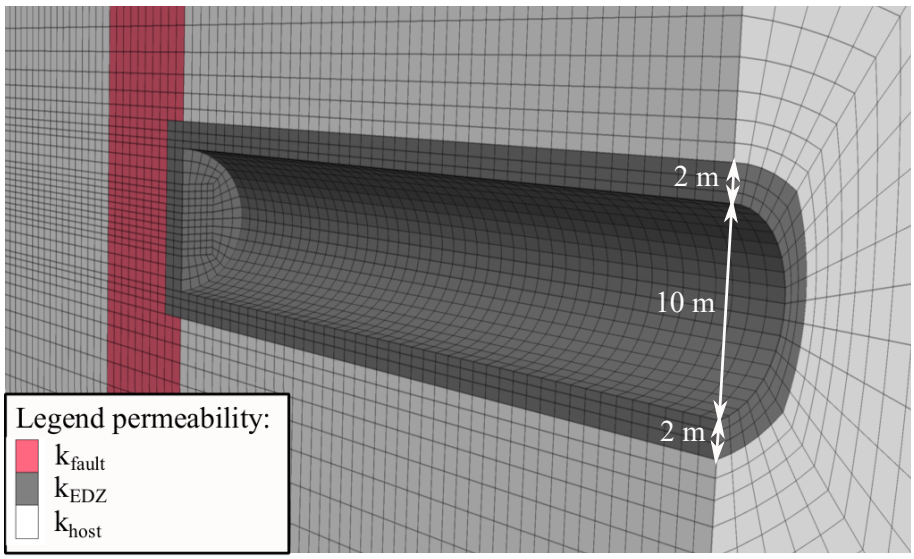

Figure 6.22: Numerical model of the EDZ in 3D analyses

Model	Hydraulic conductivity [m/s] Host rock	Fault zone	EDZ	Fault zone width [m]	Tunnel diameter [m]	Initial pore pressure [MPa]	Advance rate [m/d]
Hom_EDZ_{10}	10^{-8}	-	10^{-7}	-	10	4	4
Hom_EDZ_{100}	10^{-8}	-	10^{-6}	-	10	4	4
$LPFZ\_EDZ_{10}$	10^{-8}	10^{-10}	10^{-7}	10	10	4	4
$LPFZ\_EDZ_{100}$	10^{-8}	10^{-10}	10^{-6}	10	10	4	4
$HPFZ\_EDZ_{10}$	10^{-8}	10^{-6}	10^{-7}	10	10	4	4
$HPFZ\_EDZ_{100}$	10^{-8}	10^{-6}	10^{-6}	10	10	4	4

Table 6.4: Numerical models with consideration of an excavation damage zone (EDZ)

Figure 6.23 shows the effect of an EDZ with an increase in permeability by the factor of 10 and 100 on the pore pressures in homogeneous rock mass. The pore pressures in a distance of up to 5 m to the tunnel face decrease significantly, compared to the model with equivalent permeability without EDZ. The high permeability of the EDZ increases the drainage area of the tunnel and therefore facilitates drawdown. The maximum hydraulic gradient is approx. 15 % lower than without consideration of an EDZ. The calculations for an increase of permeability by the factor 10 and 100 in the EDZ yield results in the same order of magnitude. This highlights that the actual permeability of the EDZ has little influence on the hydraulic head field.

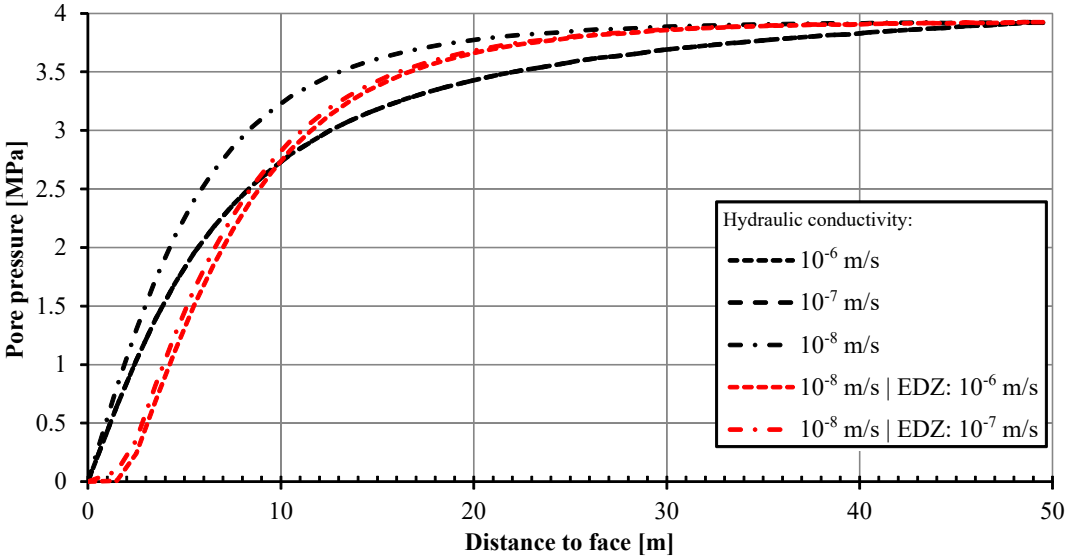

Figure 6.23: Pore pressure distribution at tunnel axis for homogeneous rock mass without (black) and with (red) consideration of an EDZ

For heterogeneous conditions, the cases of a fault zone with higher (HPFZ) and lower hydraulic conductivity (LPFZ) are investigated (see Table 6.4). For comparison, the maximum hydraulic gradients are plotted along the tunnel axis (Figure 6.24). In both cases (LPFZ and HPFZ), the maximum hydraulic gradients at the transition to the more permeable rock mass are significantly lower when considering an EDZ, because the EDZ facilitates drawndown ahead of the face. Similar to homogeneous rock mass, the actual permeability within the EDZ is of minor significance.

In summary, the formation of an EDZ acts favourably on tunnel stability, because the hydraulic gradients are lower than without EDZ. At the same time, the EDZ represents an area with reduced rock mass quality as well as increased permeability and is therefore potentially susceptible to higher inflow rates (at least over a short time) and erosion.

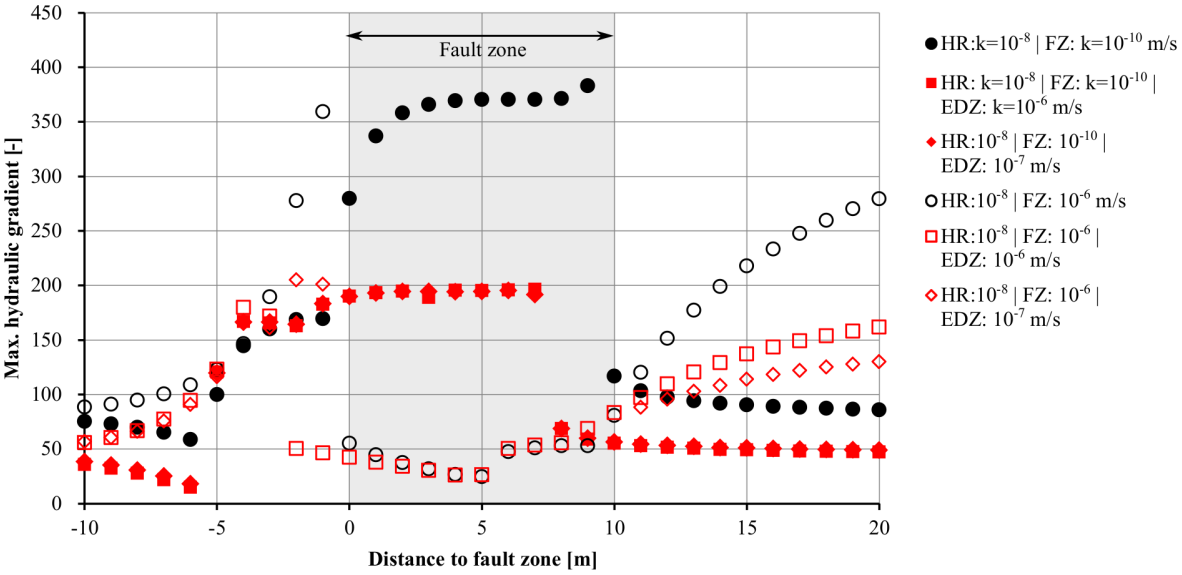

Figure 6.24: Max. hydraulic gradients for low- and high-permeability fault zones without (black) and with (red) consideration of an EDZ; Abbreviations: HR...host rock; FZ...fault zone

6.6 Case study

During the excavation of the Semmering base tunnel, piezometers were installed ahead of the tunnel face in selected fault zones. The measurements should provide information on the pore pressures in vicinity of the tunnel during excavation and thus contribute to verifying the chosen modelling approach during the design phase, which was based on numerical analyses with hydraulic-mechanical coupling (Lenz et al., 2018). The available measurement data are used to verify the results presented in this thesis, particularly to investigate the applicability of the approximation function for the hydraulic head.

6.6.1 Piezometer measurements in the fault zone 'Eichberg'

Two piezometers were installed in the two tunnel drives starting from Gloggnitz (construction lot SBT1.1) in the easternmost section of the Semmering base tunnel. The piezometers are situated at the beginning of a major strike-slip fault zone with a thickness of more than 100 m within the Greywacke zone, the so-called Eichberg fault zone. The rock mass consists primarily of phyllites and schists, which generally exhibit a high degree of tectonization. A simplified geological model is displayed in Figure 6.25. According to the geological prognosis, a hydraulic conductivity in a range of $k = 10^{-8} - 10^{-10}$ m/s was expected.

The measurement layout should allow for measuring the pore pressure in the fault zone in various distances to the excavation. However, at the time of device installation, the position and spatial orientation of the fault zone was not exactly known. The first piezometer was installed in an exploration bore, drilled from track 1 approx. 50 m ahead of the expected fault zone position. The sensor was installed at a lateral distance of approx. 15 m to the tunnel lining at chainage 1347. A second device was installed laterally after excavation of track 1 in a borehole perpendicular to the tunnel axis towards track 2 at the expected transition to the fault zone in track 2. The position of the two piezometers with respect to the encountered geological conditions is shown in Figure 6.25. The sensor PZ TM 1506 was installed at a lateral distance of approx. 10 m to the lining of track 2. An installation closer to the lining

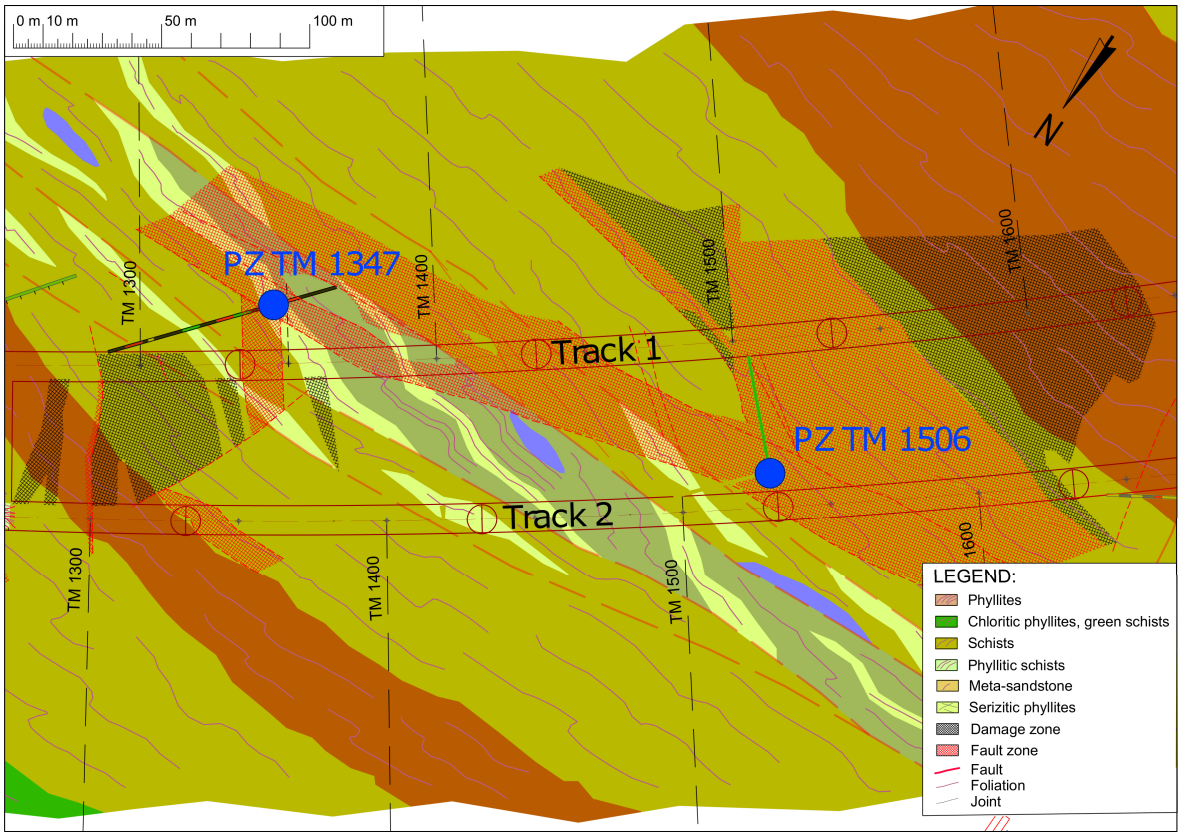

Figure 6.25: Position of piezometers in the drives Gloggnitz and simplified geological conditions (modified from Lenz et al. (2018)); Abbreviations: TM...chainage; PZ...piezometer

was omitted because of the high risk that the sensor gets damaged during rock bolting.

In order to allow for measurement of negative pore pressures, vibrating wire piezometers of the type GEOKON 4500DP with a measurement range of -0.1 to 2 MPa were used. The conditions for piezometer installation turned out to be quite challenging. In the first borehole (track 1), the casing of the borehole had to be removed for geophysical measurements before installation of the piezomemeters. The second drilling was conducted without casing straight away, because equipment for cased drillings was not available at that time. In both cases the unlined boreholes locally collapsed in the weak rock mass, which required re-drilling of the holes. For facilitating device installation the boreholes around the piezometers were fully grouted, as proposed by Mikkelsen & Green (2003). To eliminate the influence of grout stiffness on the measurements, the grout was designed to mimic the actual stiffness of the rock mass. A mix of cement and bentonite (cement: 25 kg; bentonite: 5 kg; water: 50 l) was used, reaching a stiffness of approx. 70 MN/m^2 after 28 days (Mikkelsen & Green, 2003). The sensor was mounted on a 1-inch-steel tube , which was used to push the sensor into place and to protect the data cable from damage (e.g. due to subsequently installed drill holes and rock bolts). To provide continuous data readings, data loggers with a sampling interval of 15 min were used.

Figure 6.26 shows the pore pressures recorded over time in the two piezometers in the Eichberg fault zone. In the piezometer at chainage 1347 (track 1), the pore pressure quickly increased after the zero reading to a peak value of approx. 1.05 MPa and remained at this peak for several days, although the top heading further advanced during this time. Hence, it can be

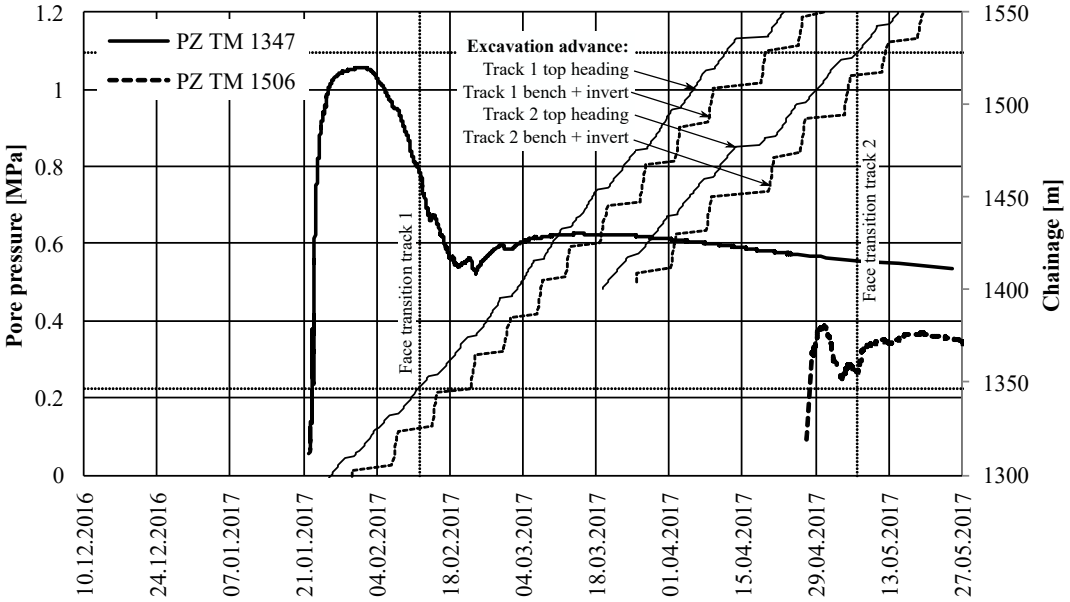

Figure 6.26: Time history of pore pressure in piezometers at chainage 1347 and chainage 1506

concluded that the peak refers to the in situ pore pressure without any disturbance by the tunnel drives ahead of the face. The measurements agree with the geological prognosis, which predicted an initial hydraulic head of 100 - 130 m. Unfortunately, corresponding measurement data from the surface (such as standpipe readings) were not available for comparison. At the end of January 2017, the pore pressure started to decrease, which can be traced to the approaching of track 1 excavation, which was in a distance of approx. 30 m to the sensor at this time. The decrease continued after face transition, until a minimum value of approx. 0.52 MPa was reached one week after face transition at the time of ring closure (approx. 25 m behind the face). Shortly after reaching it's minimum, the pore pressure increased to approx. 0.62 MPa. The reason for this increase could not fully be clarified. The recorded increase of the pore pressure qualitatively is in line with the findings of Giraud et al. (1993), who traced this phenomenon to a diffusion process in the rock mass. The piezometer at chainage 1506 (track 2) qualitatively showed a similar time history, however on a different level. The maximum pore pressure recorded was approx. 0.38 MPa, which is only one third of the initial pore pressure before excavation of track 1. Obviously, excavation of track 1 caused a significant drawdown of the pore pressure in vicinity of track 2 (axial distance track 1 - track 2: approx. 55 m). The pore pressure reached a minimum of approx. 0.25 MPa at a distance of 5 m ahead of the face. Immediately after face transition, the pore pressure rapidly increased to a value of 0.35 MPa. The reason for this increase could not be clarified.

The rock mass conductivity was verified in back-calculations based on the recorded inflow rates. In vicinity of the piezometer TM 1347, an inflow in a range of 0.002 - 0.01 l/s was recorded during excavation. At piezometer TM 1506, recorded inflows were within the same order of magnitude. For back-calculation of the hydraulic conductivity, a steady state is assumed, which actually is valid for hydraulic conductivities $> 10^{-8}$ m/s only. Using the approach of El Tani (1999) a conductivity in the range of 10^{-7} - 10^{-8} m/s was calculated. It is acknowledged that this comparison can only provide a rough estimation by two reasons: First, the inflow quantities are too low to be adequately measured on site. The values are therefore based on a visual estimation of the site geologist. Second, the calculation of inflow quantities from analytical equations assumes a stationary hydraulic head field, whereas close to the face a transient state prevails in case of the objective permeability. Nevertheless, the

performed back-analysis reveals the order of magnitude of rock mass permeability. Although the fault zone exhibits a heterogeneous composition in terms of lithologies (see Figure 6.25), it is rather homogeneous from its hydraulic properties, as confirmed by the recorded inflow rates.

The hydraulic head field ahead of the face can be estimated using Equation 6.7 as a function of the minimum radial distance between the piezometer and the tunnel. The initial hydraulic head is assumed equal to the recorded peak value in the piezometers. A comparison between the measurements and the results of the approximation function is provided in Figure 6.27. Since the approximation function describes the hydraulic head field ahead of the tunnel, a comparison is only possible until the excavation passes the position of the piezometer (i.e. up to a distance of 15 m for PZ TM 1347 and 10 m for PZ TM 1506). The calculation with $k = 10^{-8}$ m/s shows a good agreement with the piezometer measurements. With respect to the ambiguous heterogeneities within the rock mass and the uncertainties in parameter determination, an estimation of the hydraulic head is limited to an order-of-magnitude level. For this purpose, the conducted case study confirms the practical applicability of the derived approximation function for homogeneous rock mass.

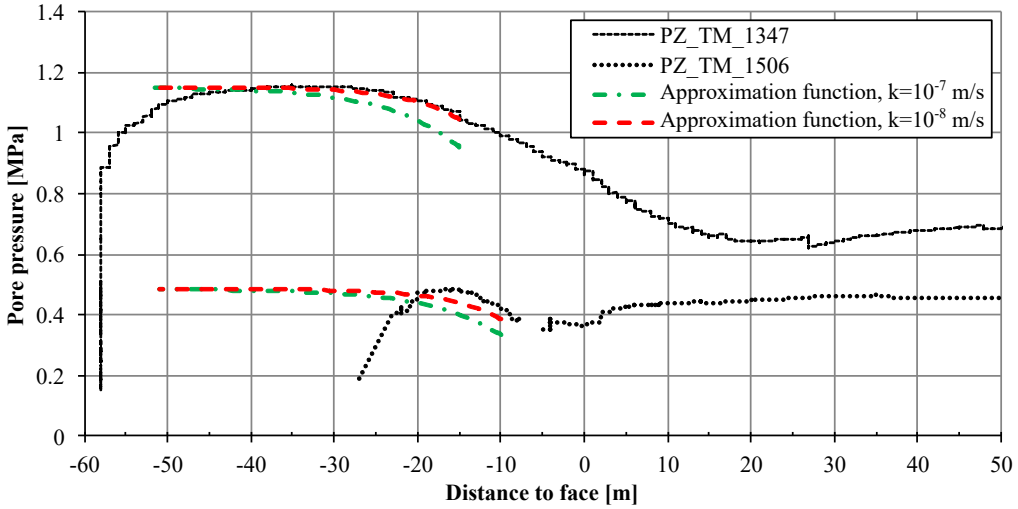

Figure 6.27: Pore pressure in piezometers PZ TM 1347 and PZ TM 1506 plotted versus distance to the tunnel face and results of approximation function (Equation 6.7)

6.6.2 Piezometer measurements in the fault zone 'Schlagl'

A single piezometer was installed during excavation of the intermediate access 'Goestritz' in the so-called Schlagl fault zone, which marks the transition from sericitic-phyllitic cataclasites to the carbonatic rock mass of the Otter massive (Figure 6.28). The exact position and spatial orientation of the transition was previously determined by several exploration drillings during excavation. The hydraulic conductivity of the fine-grained sericitic-phyllitic cataclasites was expected in a range of $\leq 10^{-8}$ m/s, while the carbonates exhibit comparatively high hydraulic conductivities of $\geq 10^{-6}$ m/s. The latter assumption was confirmed by several probe drillings, which caused a significant surge (>1 l/s per borehole), combined with ingress of fine material. The initial hydraulic head was approx. 25 - 40 m above tunnel axis as standpipes in the objective area showed. Due to good knowledge of the geological setting at the time of installation, the piezometer could be installed comparatively close to the tunnel lining in a lateral distance of approx. 5 m to the sidewall. An installation closer to the tunnel

was omitted to avoid conflicts with radial bolting. For details on the installation it is referred to the previously presented case study.

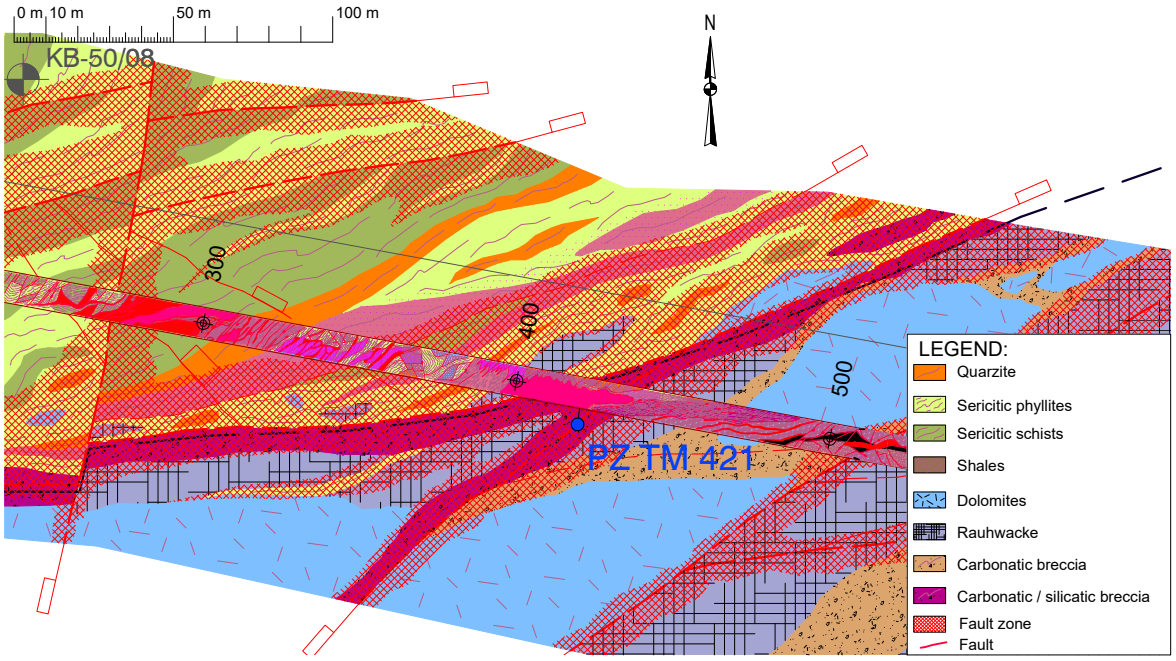

Figure 6.28: Position of piezometers in the intermediate access Goestritz and simplified geological conditions; Abbreviations: TM...chainage; PZ...piezometer; KB...core drilling

Figure 6.29 shows the time history recorded in the piezometer at chainage 421. The pore pressure quickly increased after grouting the borehole and stagnated at a value of approx. 0.27 MPa, which corresponds well with the hydraulic heads measured in the standpipes in this area. Starting at 21.09.2016, the pore pressure slightly decreased, followed by a series of rapid increases and consecutive drops of the pore pressure. The time of these step-shaped increases coincided exactly with the time of blasting in the top heading. In short-term, the pore pressures immediately increased due to stress redistribution during excavation, which correlates with the behaviour expected for undrained conditions. However, the excess pore pressure decreased over the time required for one round and did not affect the actual drawdown of the pore pressure due to excavation. Approx. 48 h before face transition, the pore pressure rapidly dropped and reached a minimum of approx. -0.01 MPa (i.e. a negative pore pressure / suction) just before face transition. The sudden decrease of the pore pressure could be related to a drainage drilling, which was installed in vicinity of the sensor.

The measurement data outlines the interaction of stresses and pore pressures. In the objective case, the hydraulic head field is significantly influenced by the stress redistribution during excavation, which contributes to the decrease of pore pressures close to the face and causes negative pore pressures over a short time. This effect has not been taken into account yet, but is studied within the following chapter. A comparison between the calculation results for heterogeneous rock mass and the monitoring data is not reasonable because of the dominating effect of the drainage drilling.

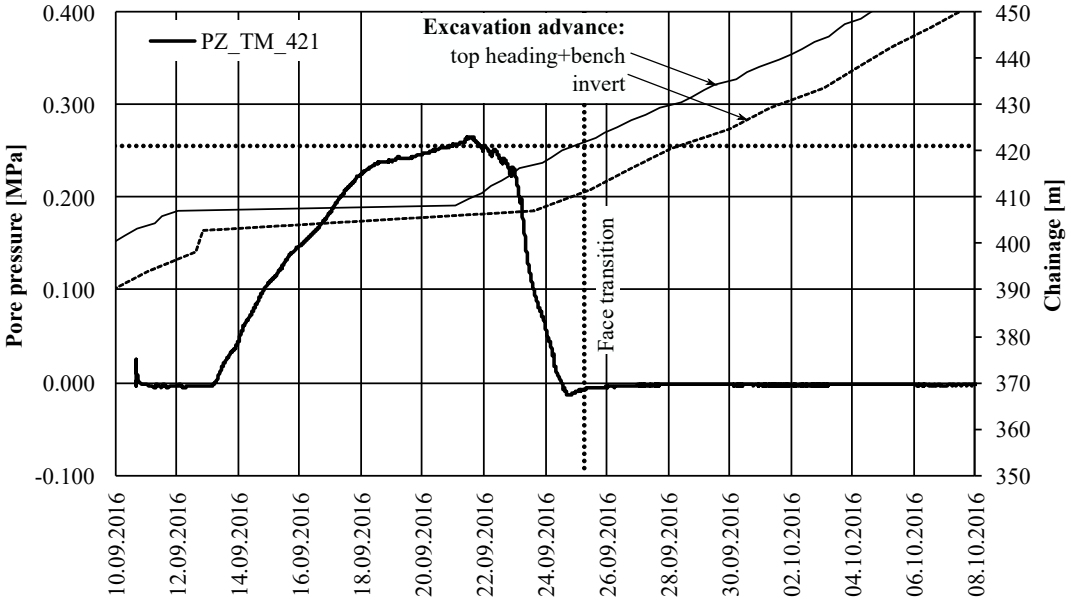

Figure 6.29: Time history of pore pressure in piezometer PZ TM 421

6.7 Summary

The main findings from the studies presented within this chapter are summarized as follows:

- In homogeneous rock mass, the hydraulic head field is mainly controlled by the rock mass permeability, the advance rate and the tunnel diameter. Transient conditions evolve in case of hydraulic conductivities of $\leq 10^{-8}$ m/s. The distribution of the hydraulic heads ahead of the face can adequately be estimated using the approximation function as per Equation 6.7.
- In heterogeneous rock mass, the hydraulic heads primarily depend on the contrast between fault rock and host rock permeability, and on the fault zone width. In case of a hydraulic contrast of two orders of magnitude or higher, a thickness in the range of decimetres to metres can cause a hydraulic head in the range of the initial head when entering more permeable rock mass. Similarly to homogeneous rock mass, an approximation function is provided to estimate the maximum hydraulic head as a function of hydraulic contrast and fault zone width (Equation 6.10). However, the use of this function should be limited to cases in which the hydraulic properties and the geological situation are sufficiently known. In all other cases, the conservative assumption of the initial head acting at the transition to the more permeable rock mass is recommended.
- The formation of an excavation damage zone (EDZ) with increased permeability yields lower hydraulic gradients and is therefore considered favourable for tunnel stability.
- Pore pressures and stresses do interact, at least to a certain extent. In other words, the hydraulic head field may depend on the stress level and the mechanical parameters of the rock mass. This effect is investigated in the following chapter.

7 Interaction of stress and pore pressure

During tunnel excavation and the consequent stress redistribution, a change in pore pressure occurs, provided that the differential hydraulic head cannot be equalized by seepage flow fast enough, that is in rock mass with comparatively low permeability. In such cases, stresses and pore pressures interact. This interaction is fundamentally described by the three-dimensional consolidation theory formulated by Biot (1941). A change in pore pressure will affect the effective stresses and volumetric strains. Vice versa, a change in the effective stress field causes a change in pore pressure. For rock mass with high stiffness, and consequently low changes in volumetric strains, this effect may be considered negligible, whereas in cases of weak rock mass with low permeability, the interaction of deformation and pore pressure may play a decisive role. The influence of mechanical-hydraulic interaction on stresses and pore pressures is investigated in a numerical parametric study.

7.1 Numerical model

The calculation model basically is identical to the model described in chapter 6. Similarly to the calculations presented in chapter 6, a step-by-step excavation with a round length of 1 m is modelled. This means that the change in volumetric strain (due to excavation of the next round) occurs in an infinitely small time step. Over the time required for completion of one round (depending on the advance rate), excess pore pressures can equalize by fluid flow.

Coupled analyses with FLAC3D are based on Biot theory. The process of fluid flow is divided into n steps, during which fluid flow can occur until either the steady state is reached or the total flow time exceeds the preset limit (i.e. the time required for excavation of one round). During each fluid flow step, the mechanical module of FLAC3D is executed in substeps until equilibrium is reached or a given number of iterations has been performed.

The rock mass parameters used for the objective sensitivity study are based on the results of laboratory tests from the Semmering base tunnel (ÖBB Infrastruktur AG, 2019) and should reflect the typical range of mechanical properties of faulted rock mass. Four different rock mass types with varying strength and stiffness parameters are defined, (see Table 7.1). Linear elastic - perfectly plastic material behaviour with Mohr-Coulomb (MC) failure criterion and tension cut-off is presumed.

Rock mass parameter set	Specific weight [kN/m^3]	E-modulus [MPa]	Cohesion [MPa]	Friction angle [°]	Poisson's ratio [-]	Porosity [-]	Hydraulic conductivity [m/s]
A	25	1000	0.4	26	0.25	0.25	10^{-6} - 10^{-10}
B	25	2000	0.8	26	0.25	0.25	
C	25	4000	1.6	30	0.25	0.25	
D	25	1700	0.08	30	0.20	0.25	

Table 7.1: Material parameters used for sensitivity analysis of interaction of stresses and pore pressure

For fault material consisting mainly of phyllites and schists, lab testing during the exploration campaign at the Semmering base tunnel revealed a correlation between shear strength and

stress level (Goricki & Pimentel, 2013). The deformation parameters furthermore showed a high dependency on stress level and loading history (i.e. the sequence of unloading and reloading cycles). To adequately model these dependencies, the plastic-hardening model (PH) developed by Schanz et al. (1999) is used complementary. This model allows to consider stress - strain dependent stiffness and shear strength. In the stiffness model, distinction is made between unloading and re-loading. The yield surface in the PH model is not fixed in principal stress space, but can expand due to plastic strain (hardening). Distinction is made between shear hardening and compression hardening (Schanz et al., 1999).

For calibrating the PH model, results of a consolidated drained (CD) triaxial test with three load stages at different confining stresses were available (ÖBB Infrastruktur AG, 2019). The triaxial test is modelled with FLAC3D using the PH model. Figure 7.1 shows the calculated deviatoric stresses versus the axial strains for the numerical model (dotted line, parameters acc. to Table 7.2) in comparison to the results of the lab test (continuous line). For reference, calculations with comparable strength and stiffness parameters assuming linear elastic - perfectly plastic material behaviour (MC) are conducted as well (parameter set D in Table 7.1).

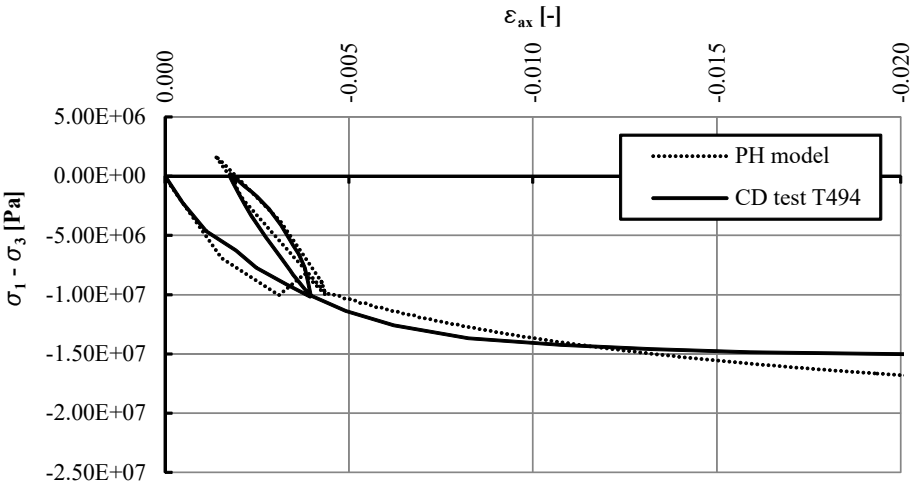

Figure 7.1: Comparison of deviatoric stress $\sigma 1$ - $\sigma 3$ versus axial strain for lab test T494 and PH model in FLAC3D

Specific weight	γ	[kN/m^3]	25
Reference secant stiffness	E_{50}^{ref}	[GPa]	1.7
Unloading - reloading stiffness	E_{ur}^{ref}	[GPa]	3.5
Initial stiffness	E_0^{ref}	[GPa]	1.0
Reference pressure	p^{ref}	[MPa]	10
Exponent	m	[-]	0.9
shear strain	γ_{70}	[-]	$1.5 \cdot 10^{-4}$
Cohesion	c	[MPa]	0.08
Friction angle	ϕ	[°]	30

Table 7.2: Parameters used for plastic hardening model, rock mass parameter set D

A porous medium essentially consists of three phases: matrix, fluid and gas (Coussy, 2004). Below the groundwater table, usually fully saturated conditions are assumed and the gas phase is not considered. The fluid normally contains a certain amount of trapped air. As long as the air is dissolved in the fluid, its impact on the fluid bulk modulus is negligible

(Fredlund & Rahardjo, 1993). However, due to stress relief during excavation the trapped air precipitates and a partially saturated state develops (see chapter 2). The numerical formulation in FLAC3D does not allow for consideration of partially saturated conditions (Itasca Consulting Group, Inc., 2017). In case of a saturation <1 the pore pressure would immediately go to zero. To overcome these deficits, a reduced bulk modulus of the fluid is assumed to consider the effect of trapped air and to avoid unrealistically high negative pore pressures. For all analyses, a fluid bulk modulus of 100 MPa is assumed (pure water: approx. 2 GPa). This corresponds to a content of trapped air of approx. 1 % void volume (Fredlund & Rahardjo, 1993).

The conducted sensitivity analysis comprises calculations with the Mohr-Coulomb (MC) model for the parameter sets A - D (Table 7.1) and calculations with the plastic-hardening (PH) model (Table 7.2). Hydraulic conductivities are varied between 10^{-6} - 10^{-10} m/s. The tunnel diameter is equal to 10 m in all calculations, support measures are not considered. To avoid an inordinate size of the plastic zone, a moderate primary stress level of 5 MPa and an initial pore pressure of 2 MPa are assumed. Additionally, all calculations are conducted without consideration of groundwater ('dry') in terms of total stresses for reference.

7.2 Homogeneous rock mass

7.2.1 Parametric study

Figure 7.2 shows the compiled results of the parametric study for the evaluation point at the tunnel axis. Parameter sets yielding unrealistically high displacements (in the range of > 1 m) are omitted in the evaluation. The difference in the stress distribution for different strength parameters becomes evident by looking at the analytical description of the objective problem (see chapter 2, Equations 2.21 - 2.24). The description of results is therefore limited to the most relevant aspects.

Figure 7.2a and 7.2b show the major principal stresses in terms of total and effective stresses. The minor principal stresses are displayed in Figure 7.2c and 7.2d. The black lines refer to calculations without consideration of groundwater ('dry'), whereas the coloured lines are obtained in fully coupled analyses. Figure 7.2e shows the corresponding pore pressure distributions. The black lines refer to the results of fluid flow calculations (as described in chapter 6).

The major principal stresses (oriented vertically in vicinity of the face) show a pronounced peak at a distance of 5 - 10 m to the face for parameter sets A and B (Figure 7.2a). This peak marks the transition from the plastic to the elastic domain and corresponds to the extend of the plastic zone developing ahead of the face. In case of parameter set C, this peak occurs at a distance of 2 - 3 m to the face, however less pronounced. The stress distribution obtained with the PH model deviates significantly from all other calculations and shows a rather smooth increase to the primary stress level at a distance of approx. 12 m ahead of the face. For this constitutive model the yield surfaces is related to plastic strain (and not to principal stress space). The transition from the elastic to the plastic domain is therefore shifted further away from the face. The effective stresses (Figure 7.2b) reach a plateau between 2 - 5 m ahead of the face for parameter sets A and B, at which no increase of effective stresses occurs. For parameter set C and the calculations using the PH model, a similar behaviour cannot be identified.

The evaluation for the minor principal stresses (oriented parallel to the tunnel axis in vicinity of the face) reveals, that the effective stresses go to zero (tensile stresses are ruled out in the

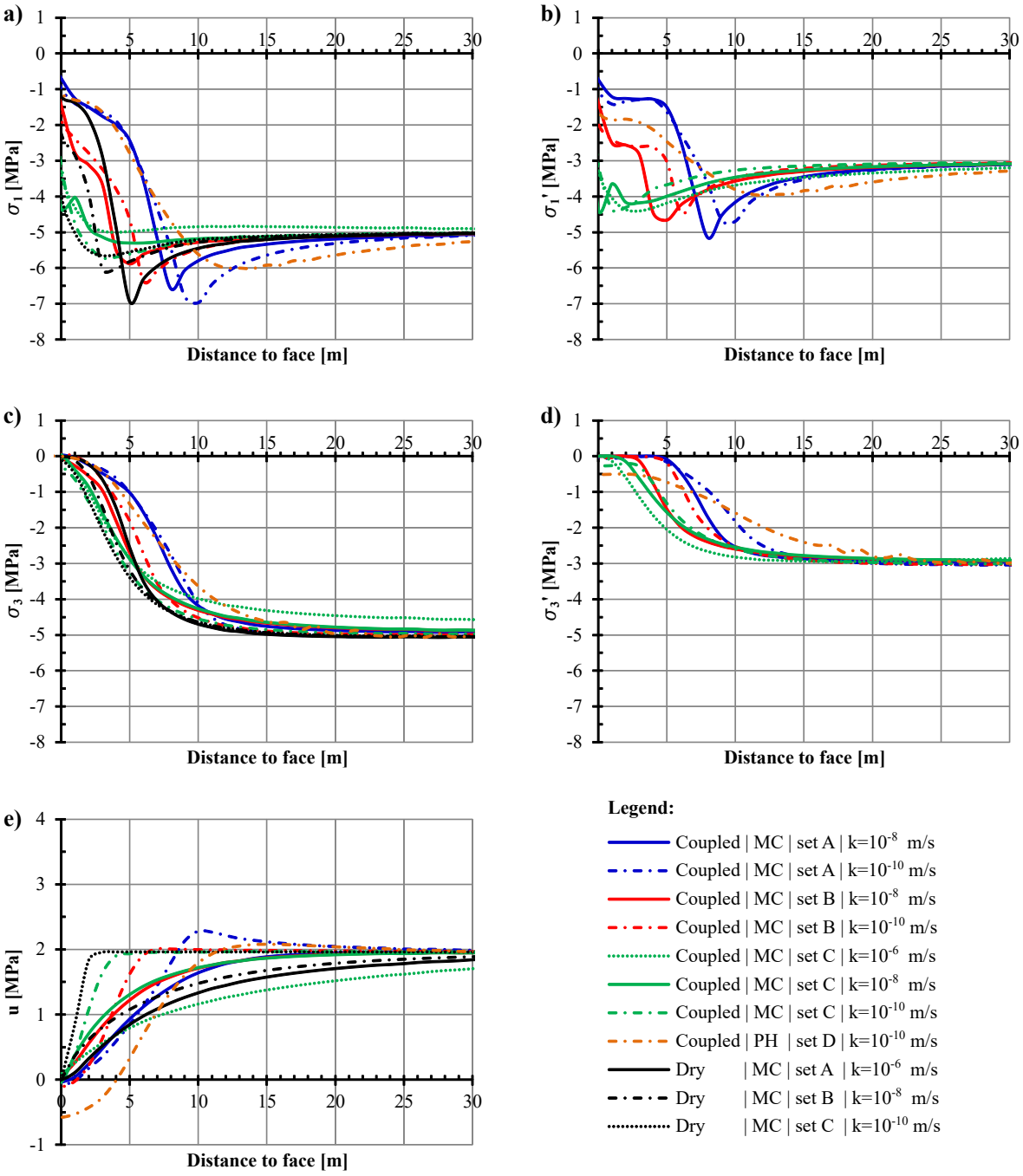

Figure 7.2: Compiled results of the parametric study, evaluation at the tunnel axis: a) major principal stress (total); b) major principal stress (effective); c) minor principal stress (total); d) minor principal stress (effective); e) pore pressure

calculations by the tension cut-off) in a zone with an extent of several metres ahead of the tunnel face (Figure 7.2d). The extend varies from 5 m (set A) to 2 m (set C). Again, results from the PH model deviate significantly from results obtained with MC model. In case of the PH model, a zone with zero effective stresses does not occur, which essentially can be traced to negative pore pressures, as shown later. Generally, the stress distribution differs within each parameter set depending on the respective rock mass permeability.

The pore pressure distribution (Figure 7.2e) obtained by coupled analyses (coloured lines) generally deviates from the results of the fluid flow calculations (black lines). Negative pore pressures occur in a zone close to the face using parameter sets A, B and the PH model. In case of the parameter sets A and B, the extent of this zone is limited to 2 m, in case of the PH model, it extends up to approx. 5 m. The calculated negative pore pressures are in a range of ≤ 0.1 MPa, despite in case of the PH model, which yields a negative pore pressure of approx. 0.55 MPa. In case of weak rock mass with low permeability (parameter sets A and B, $k = 10^{-10}$ m/s), the maximum calculated pore pressure exceeds the initial pore pressure at a distance of 7 - 10 m ahead of the face. Using parameter set C, no negative pore pressures are calculated.

7.2.2 Discussion

The calculated stress distribution is exemplarily elaborated for parameter set A and a hydraulic conductivity of $k = 10^{-8}$ m/s (Figure 7.3). Generally, excavation induces stress redistribution ahead of the face. The major principal stresses form an arch around the tunnel face, causing stress concentration ahead of the face. When the stress state exceeds the bearing capacity of the rock mass, a plastic zone forms ahead of the face and the stresses are re-distributed further ahead from the face. The maximum major principal stresses occur at the transition from the plastic to the elastic domain. When groundwater is present and rock mass permeability is low, changes in total stresses are compensated by pore pressures (at least partly) and the effective stresses, and consequently the shear resistance, are reduced. Thus, the extent of the plastic zone increases and the maximum major principal stresses occur in greater distance to the tunnel face. Close to the face, the minor principal effective stresses go to zero and a hemispherical zone close to the tunnel face fails in tension.

The extent of the plastic zone does not only depend on the mechanical properties and the stress level, but also on the permeability of the rock mass. In case of higher permeabilities, excess pore pressures can equalize by seepage to a certain extend. In case of low permeability, the change in total stresses (due to excavation) is compensated primarily by the increase of pore pressure and the effective stresses are reduced consequently. Therefore, cases with lower permeability generally yield a larger plastic zone, as indicated by the location of the peak of the maximum major principal stresses, displayed in Figure 7.2a. The stress concentration at the transition to the elastic domain may produce pore pressures that exceed the initial value. At the same time, stress relief close to the face may create negative pore pressures close to the face, which increases the effective stresses and thus act favourably for tunnel stability. The magnitude of negative pore pressures is controlled by strength and deformation properties of the rock mass, by the permeability and by the portion of air dissolved in the fluid, as explained previously. The lower the strength and deformation properties and the lower the permeability, the higher the negative pore pressures. No negative pore pressures are calculated for a hydraulic conductivity of $k = 10^{-6}$ m/s.

The essentially different stress distribution when using the PH model is primarily traced back to the low stiffness of the rock mass close to the excavation, since the unloading - reloading stiffness E_{ur} depends on the minor principal stress σ'_3 (Schanz et al., 1999). The latter is low

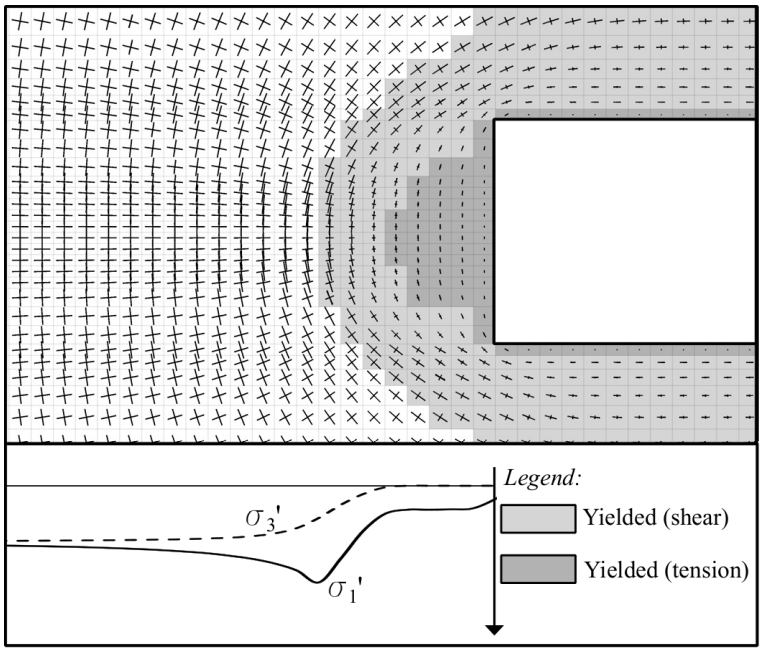

Figure 7.3: Longitudinal section of stress tensors and plastic zone (top) and qualitative distribution of effective stresses ahead of the face (bottom) for parameter set A, $k = 10^{-8}$ m/s

close to the face. Domains with higher stiffness, far away from the face, attract the stresses and yield a stress redistribution (arching) further into the rock mass. This also results in a larger plastic zone. Close to the face, positive volumetric strains (extension) occur and consequently negative pore pressures are generated.

As Figure 7.2e shows, the hydraulic-mechanical coupling may significantly influence the hydraulic head field. For low-permeability rock mass and low strength and stiffness properties, the hydraulic head field changes significantly due to the occurrence of negative pore pressures in vicinity of the face. The magnitude of the maximum hydraulic gradient remains approximately the same as calculated in the fluid flow calculations, but it occurs further away from the face. These findings may affect the applicability of the analytical estimation of the hydraulic head field presented in chapter 6 in case of low-permeability rock mass. However, the presented equations can still serve as a conservative approach for engineering applications, neglecting the stabilizing effect of negative pore pressures. For higher permeabilities and mechanical parameters, the deviation from the results of fluid flow calculations is considered negligible with respect to the ambivalent and inevitable uncertainties in parameter determination for deep tunnels.

During literature review (see chapter 2), no analytical solution could be found which adequately describes the complex interaction of stresses and pore pressures ahead of the face. A superposition of solutions formulated in total stresses (e.g. Kolymbas (1998)) and pore pressure distributions based on fluid flow calculations (e.g. Equation 6.7) would return negative (tensile) effective stresses close to the face, which does not make sense from a mechanical point of view. To adequately assess the stress distribution in weak rock mass with low permeability, three-dimensional numerical analyses with hydraulic-mechanical coupling are without alternative, at least at the time being.

7.3 Heterogeneous rock mass

The results presented above emphasize the complexity of stress and pore pressure interaction in homogeneous rock mass. For heterogeneous rock mass, the number of influencing factors further increases, e.g. by the spatial orientation of the fault zone and its extent as well as the mechanical and hydraulic rock mass properties of the fault zone and their ratio compared to the host rock. In fact, the problem of the stress field in heterogeneous rock mass is not yet fully understood for dry conditions. Grossauer (2001) analysed the impact of heterogeneous rock mass on stress field and tunnel displacements. For elastic conditions, he proposed a correlation for the increase of the major principal stresses in the host rock when approaching a fault zone, considering the fault zone length and the stiffness contrast between fault and host rock. For elasto-plastic material behaviour, such a correlation could not be established. If possible at all, a consistent analytical description of the stress - pore pressure interaction in heterogeneous rock mass would go beyond the scope of this thesis.

Considerations on the stress distribution in heterogeneous rock mass are elaborated based on a case study from the Semmering base tunnel. A major collapse of the tunnel face with several hundred cubic metres of debris occurred when approaching an approx. 5 m thick damage zone within phyllites and schists of the Greywacke zone. Figure 7.4 shows the geotechnical interpretation of this event. The collapse is traced back to a stress concentration in the host rock when approaching the damage zone, which caused overloading of the rock mass ahead of the tunnel face. Due to loss of confinement stresses, blocks and slabs could slide along the foliation subsequently and caused a progressive overbreak, finally resulting in a large scale collapse of the tunnel (Gschwandtner et al., 2019).

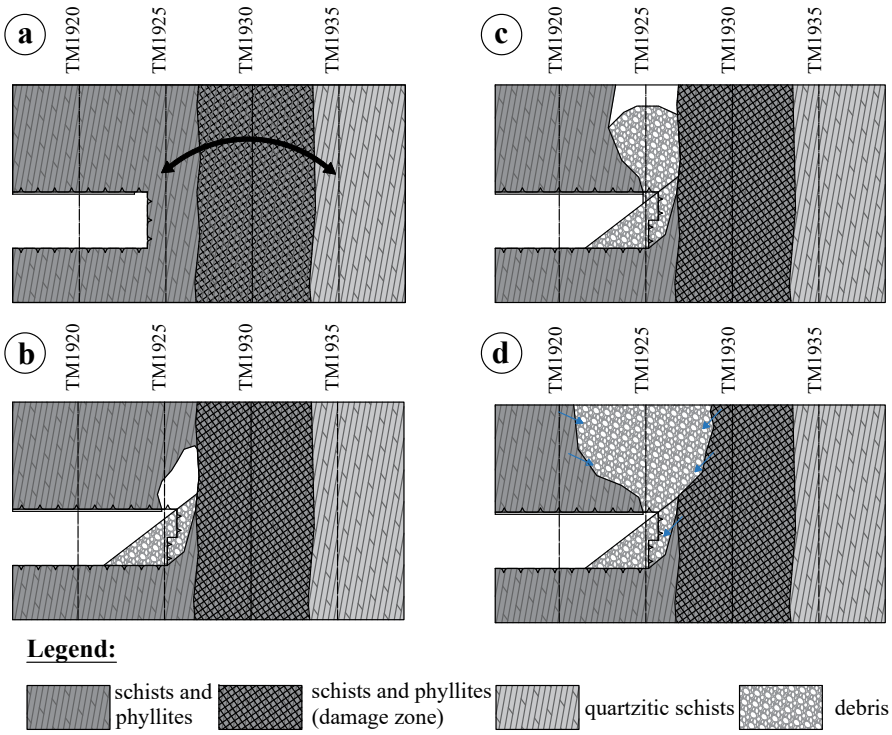

Figure 7.4: Geotechnical interpretation of collapse at chainage 1926, Semmering base tunnel: (a): stress concentration in competent rock mass ahead of and behind damage zone; (b) initial collapse during excavation; (c): continuous relaxation of rock mass, falling of loose material into collapse chimney; (d): groundwater ingress into collapsed material (Gschwandtner et al., 2019)

Before and immediately after the collapse, no significant groundwater inflow could be observed. Consequently, groundwater is not considered to have a relevant impact on the actual failure mechanisms. However, increasing seepage from the debris during the first few days after the collapse indicated the presence of groundwater in the surrounding rock mass. With numerical calculations the potential impact of groundwater on the stress distribution is investigated. The rock mass parameters (see Table 7.3) are based on the calculation values for the respective rock mass types defined during the design phase of the Semmering base tunnel (ÖBB Infrastruktur AG, 2019). Tunnel support is not considered in the analyses. For sake of simplicity, a circular tunnel with equivalent cross section is investigated instead of the actual, horseshoe-shaped tunnel. Both, the case of a low-permeability (LPFZ) and a high-permeability fault zone (HPFZ), are analysed in calculations with full mechanical-hydraulic coupling as described above. For reference, an additional analysis is performed without consideration of groundwater ('dry').

Parameter		Unit	Host rock	Fault zone
Specific weight	γ	kN/m^3	25	25
Young's modulus	E	MPa	4000	2000
Poisson's ratio	ν_p	-	0.25	0.27
Porosity	n	-	0.20	0.20
Friction angle	ϕ	^{o}	25	22
Cohesion	c	MPa	1.20	0.10
Hydraulic conductivity	k	m/s	10^{-7}	10^{-5} — 10^{-9}
Primary stress	σ_0	MPa	1.80	
Lateral pressure coeff.	K_0	-	0.8	
Tunnel diameter	D	m	10	

Table 7.3: Summary of calculation parameters for case study Semmering base tunnel

The calculated stresses and pore pressures for these cases are displayed in Figure 7.5, which shows the state lines of total and effective stresses as well as the pore pressure distribution at the tunnel axis for selected calculation steps. All values are normalized to their initial value (σ_0 and p_0 respectively). At chainage '-10', that is 10 m ahead of the damage zone, the major principal stresses in the 'dry' calculation (without consideration of groundwater) reach approx. 1.2 times the initial value at a distance of 3 m to the tunnel face. This stress concentration can be traced back to the arching effect ahead of the tunnel face (see section 7.2). A similar peak can also be identified in the effective stresses for LPFZ and the HPFZ. However, in the latter cases the increase in the major principal stresses is approx. 1.4 times the initial value. The minor principal stresses (i.e. parallel to the tunnel axis) in dry conditions increase continuously to their initial value. In case of the LPFZ, the effective stresses increase to approx. 1.2 times the initial value at the transition to the damage zone. This increase in effective stresses is caused by the comparatively low pore pressure in the region, because groundwater drawdown occurs ahead of the damage zone. In case of the HPFZ, an approx. 2.5 m thick zone with zero effective stress develops ahead of the face, because the change in total stress is compensated by the pore pressure. Groundwater drawdown in this case does not occur, since the rock mass ahead of the damage zone is continuously re-charged from the damage zone, which acts as a conduit.

At a distance of 5 m to the damage zone the situation basically remains unchanged for dry conditions. No further increase in the major principal stresses is recorded. This means that the damage zone at this point does not yet effect the stress field. This also holds for the major principal effective stresses in case of LPFZ and HPFZ. The jagged line for HPFZ is caused

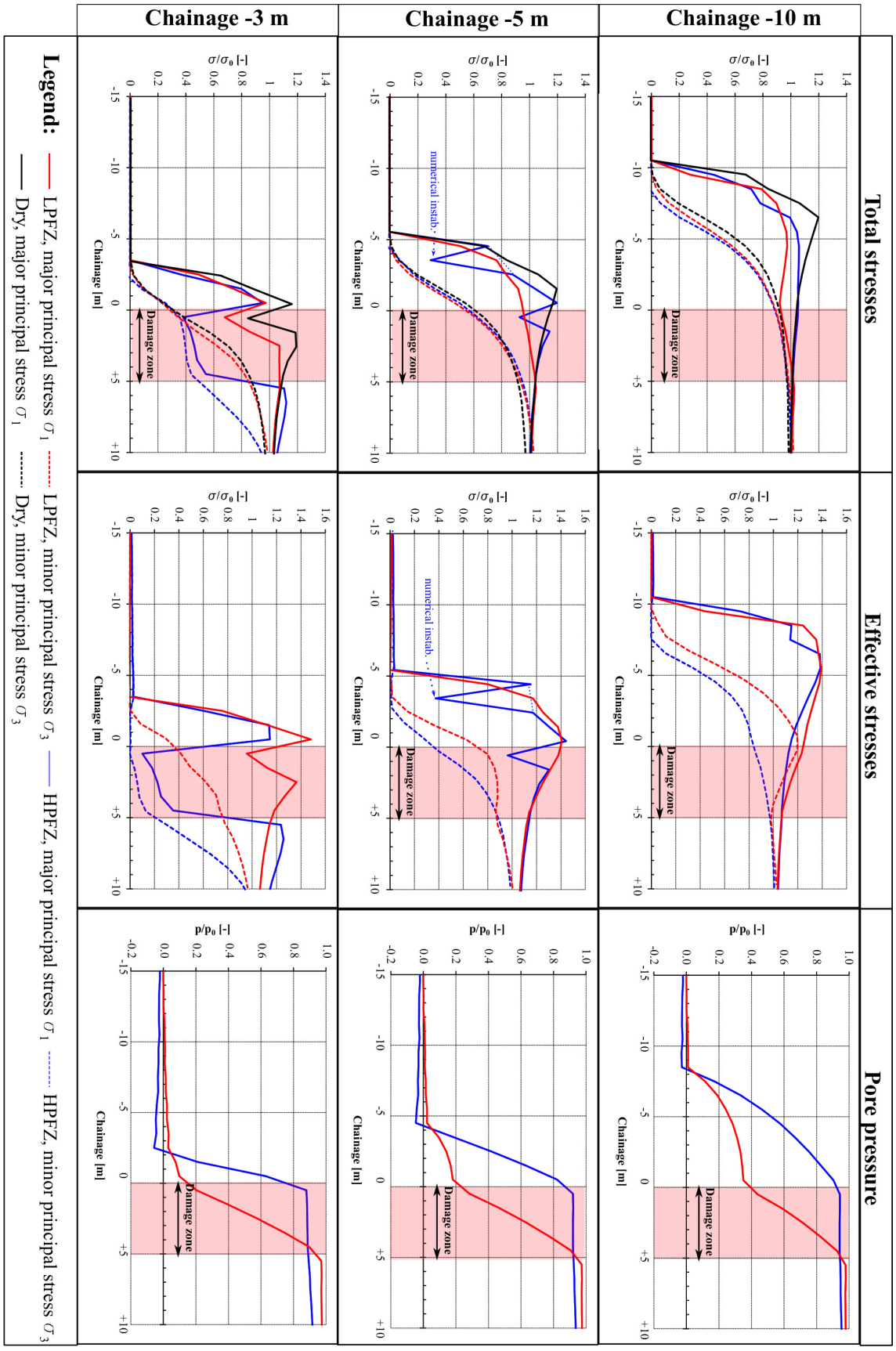

Figure 7.5: Stress state and pore pressure distribution at tunnel axis for selected chainages when approaching a 5 m thick damage zone

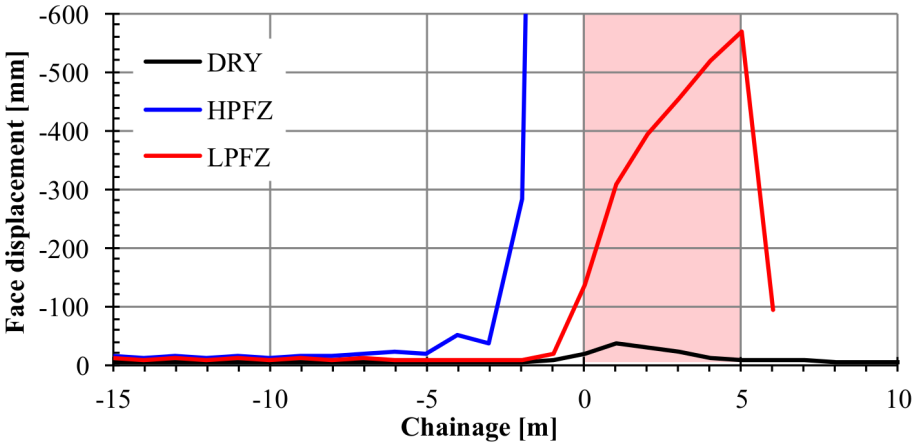

Figure 7.6: Longitudinal displacement of tunnel face at tunnel axis (positive in direction of excavation)

by numerical instabilities at the corresponding calculation steps and should be ignored. The evaluation of the minor principal effective stresses shows the formation of an unconfined zone (i.e. zero effective stress in one direction) with a thickness of approx. 2 m in case of the LPFZ. In case of the HPFZ, the size of the unconfined zone increases to approx. 3 m.

At chainage '-3', the major principal stresses for the 'dry' case deviate significantly from the former stages. While the peak value remains at the same level as before (approx. 1.2 times the initial stress), the rock mass at the transition to the damage zone is unloaded and a second peak in the middle of the damage zone develops. This stress distribution indicates the initiation of an arching effect. Stresses are re-distributed from the weak rock mass ahead of the face to more competent or better confined areas, that is the host rock ahead of the face and the damage zone at greater distance to the face, where confinement stresses (in longitudinal direction) are higher. The calculation for the LPFZ basically shows a similar stress distribution. However, the effective major principal stresses are slightly higher than in the stages before (1.5 times σ_0). The case of HPFZ yields an essentially different stress distribution. Confinement stresses (σ_3) within the damage zone are close to zero. Consequently, the rock mass within the damage zone exhibits low shear strength and the stresses are re-distributed to the host rock behind the damage zone, as indicated by the increase of the major principal stresses in this area. The unconfined zone ahead of the face increases to approx. 5 m. From chainage '-2', excessive face displacements (> 300 cm) occur in case of the HPFZ (see Figure 7.6), because a large-scale tensile failure occurs in the rock mass ahead of the face, which is consequently pushed into the tunnel by seepage forces. The calculation for the HPFZ is therefore stopped at this stage.

In the damage zone, the case of a LPFZ yields significantly higher face displacements compared to the 'dry' calculation due to the effect of seepage forces and reduced effective stresses. Face displacements continuously increase throughout the fault zone to a peak value of approx. 57 cm against the direction of excavation, immediately before leaving the damage zone. The distribution of face displacements indicates that similar conditions occur when entering a HPFZ and when leaving a LPFZ. In the latter case, the calculated displacements remain in a reasonable range. However, the calculation is conducted with a linear elastic - perfectly plastic constitutive law and stable conditions may not necessarily prevail in reality. Rather, the high displacements may rather result in a loss of shear strength (strain softening) and an increase in permeability. Furthermore, water ingress from behind the fault zone may cause further deterioration of the rock mass.

This exemplary study shows that the arching effect, that is the stress redistribution from the weak rock mass to more competent or better confined areas, occurring in the vicinity of fault zones, is influenced by the pore pressure distribution within the fault zone. If the pore pressure remains on a high level at the time of excavation (e.g. in high-permeability fault zones or in the host rock behind low-permeability layers), shear strength in these zones is low (due to lack of confinement stresses) and the arching occurs over further distance. At the same time, the major principal stresses close to the face are comparatively low and the minor principal stresses reduce to zero (unless the rock mass exhibits a certain tensile strength).

7.4 Summary

The main findings from the calculations presented within this chapter on the distribution of effective stresses are summarized as follows:

- The major principal stresses reach their maximum at the transition from the plastic to the elastic domain (provided that rock mass strength is exceeded). The stress level close to the face is comparatively low. A part of the total stresses may additionally be compensated by the pore pressure, leading to a further reduction of effective stresses and of shear strength.
- The minor principal stresses - or confinement stresses - close to the face are zero (or tensile stresses occur in case the rock mass exhibits a certain tensile strength). The extend of this poorly confined zone depends on the mechanical and hydraulic properties and may reach up to 0.5 times the tunnel diameter.
- The stress distribution described above yields a primarily uniaxial loading of the rock mass just ahead of the face. The level of loading (in other words the magnitude of the major principal stress) depends on the effective unconfined shear strength of the rock mass. In case the shear strength close to the face is exceeded, stresses are re-distributed further into the rock mass.
- The presence of a fault zone with different hydraulic and / or mechanical properties additionally influences the stress distribution. When approaching a zone with high pore pressure (e.g. a fault zone with high permeability or a water-bearing rock mass behind a low-permeability layer), the extend of the poorly confined zone may increase significantly.
- High hydraulic gradients occur in this poorly confined zone. Furthermore, the confinement stresses acting in the same direction as the main seepage forces (i.e. parallel to the tunnel axis) are zero. Consequently, this zone is particularly prone to failure induced by seepage forces.
- The most critical situations arise, when the excavation reaches zones with significantly higher permeability. In these cases, high hydraulic gradients, high inflow rates and poorly confined rock mass may occur simultaneously.
- In case of low permeability and weak rock mass, negative pore pressures can be generated, which act favourably on tunnel stability. However, due to the effects of dissolved air in the fluid, in reality the magnitude of negative pore pressures is limited.
- An adequate assessment of the stress field can only be obtained by three-dimensional, fully coupled numerical analyses.

- As an engineering approach, a hemispherical zone free of stresses ahead of the face is presumed for further analysis. This assumption reflects an idealized model of the poorly confined zone, which has been identified in numerical analyses.

8 Ground and system behaviour

8.1 General

The Austrian Society for Geomechanics released a guideline for the geotechnical design of underground structures (Austrian Society for Geomechanics, 2010). The proposed procedure foresees to first determine the *ground behaviour*, i.e. the reaction of the ground to the excavation without consideration of support measures. In a second step, the ground behaviour is assigned to one or more *ground behaviour types* as per Table 8.1, depending on failure modes and displacement characteristics. Based on this categorization, a suitable tunnelling concept is developed, support measures are assigned and the *system behaviour*, i.e. the behaviour resulting from the interaction of ground, excavation and support, is assessed.

Groundwater presence may contribute to several failure modes and behaviour types in various ways:

- Interaction of stresses and pore pressure affects the stress distribution and facilitates shear failure by reducing the effective stresses;
- Seepage forces may add a destabilizing component to slabs, blocks or other potential failure bodies;
- Seepage forces may cause wash-out of particles from the rock mass or from joint fillings;
- Groundwater may trigger a chemical reaction (swelling);
- Groundwater may contribute to the alteration of mechanical properties of the rock mass.

8.2 Hydraulic failure modes

The ground behaviour types specified in Austrian Society for Geomechanics (2010) (see Table 8.1) cover mechanical failure modes within the rock mass, but lack definitions for hydraulic failure modes (i.e. failure modes predominantly controlled by seepage). Particularly for *flowing ground* (behaviour type 9) as the most prominent ground behaviour type in water-bearing rock mass, only the behaviour subsequent to failure but not the actual failure mechanism is specified. Goricki (2003) defines flowing ground as tensile failure of the particle-to-particle bonding or loss of cohesion. In EN 1997-1 (2014), four modes of hydraulic ground failure induced by pore pressure or seepage are distinguished:

- failure by uplift (buoyancy);
- failure by heave;
- failure by internal erosion;
- failure by piping.

Basic categories of behaviour types (BT)		Description of potential failure modes/mechanisms during excavation of the unsupported ground
1	Stable	Stable ground with the potential of small local gravity induced falling or sliding blocks
2	Potential of discontinuity controlled block fall	Voluminous discontinuity controlled, gravity induced falling and sliding of blocks, occasional local shear failure on discontinuities
3	Shallow failure	Shallow stress induced failure in combination with discontinuity and gravity controlled failure
4	Voluminous stress induced failure	Stress induced failure invloving large ground volumes and large deformation
5	Rock burst	Sudden and violent failure of the rock mass, caused by highly stressed brittle rocks and the rapid release of accumulated strain energy
6	Buckling	Buckling of rocks with a narrowly spaced discontinuity set, frequently associated with shear failure
7	Crown failure	Voluminous overbreaks in the crown with progressive shear failure
8	Ravelling ground	Ravelling of dry or moist, intensely fractured, poorly interlocked rocks or soil with low cohesion
9	Flowing ground	Flow of intensely fractured, poorly interlocked rocks or soil with low cohesion
10	Swelling ground	Time dependent volume increase of the ground by physical-chemical reaction of ground and water in combination with stress relief
11	Ground with frequently changing deformation characteristics	Combination of several behaviours with strong local variations of stresses and deformations over longer sections due to heterogeneous ground (i.e. in heterogeneous fault zones; block-in-matrix rock, tectonic melanges)

Table 8.1: Ground behaviour types according to Austrian Society for Geomechanics (2010)

These failure modes reflect mechanisms typical for shallow structures in soil-like material. For deep tunnels in rock, the respective definitions require certain adaptions. The definitions according to EN 1997-1 (2014) are therefore compared to the boundary conditions in deep tunnels. To avoid misconceptions, derived but modified failure modes are re-named.

Failure by uplift according to EN 1997-1 (2014) occurs, when the pore pressure under an impermeable structure or a low-permeability layer becomes larger than the mean overburden pressure. For stability of deep tunnels this failure mode is not of particular relevance. As shown in chapter 6, the highest hydraulic gradients usually occur in the vicinity of the face. The maximum seepage forces are oriented perpendicular to the face. These seepage forces can facilitate failure in the ground ahead of the tunnel face, e.g. when a low-permeability layer hinders seepage flow towards the tunnel. In other words, the rock mass forms a 'plug', which is then pushed into the tunnel by seepage forces (see Figure 8.1a). This failure mode was reported by Brandtner & Lenz (2017) (see also Figure 3.2). For all further considerations, this failure mode is referred to as *plug failure*.

Failure by heave occurs when upwards-directed seepage forces act against the weight of the soil, reducing vertical effective stresses to zero (EN 1997-1, 2014). Soil particles are then lifted away by the seepage flow and failure occurs ('boiling'). In other publications the term *liquefaction* is used to describe these conditions (Youd, 1973; Wang, 1981). This failure mode can also occur in deep tunnels, as reported by Schwarz et al. (2006) for instance. However, even more relevant than vertical seepage through the invert is the case of horizontal seepage towards the tunnel face. Effective stresses in horizontal direction are zero at the tunnel face (except in case an active pressure is applied to the face) and increase with increasing distance to the face. In case of high hydraulic gradients, the effective stresses decrease to zero up to several metres ahead of the face, as shown in chapter 7. In case the rock mass exhibits a certain tensile strength, tension cracks are formed (see Figure 8.1a), otherwise the rock mass disintegrates by loss of particle bonding, which corresponds to the failure mode of flowing ground as defined by Goricki (2003). Although basically describing the same mechanical conditions as failure by heave, this term would be misleading with respect to face stability. Rather, the term *cracking* is used to describe conditions where the actual stress level exceeds the tensile strength of the rock mass. Cracking does not necessarily represent unstable conditions. In fact, the rock mass adjacent to the cracks may be stable, e.g. due to shear and tensile strength or due to support measures. However, the combination of newly formed cracks and seepage can trigger regressive erosion or it can lead to an increase of the water content (in cohesive material) and finally the loss of rock mass interlocking or particle bond, as shown by Wudtke & Witt (2010) and Wudtke (2014). They conducted physical model tests for a construction pit subject to seepage, which causes similar conditions as seepage at a tunnel face.

Internal erosion (suffosion) is produced by transport of particles within a soil stratum, at the interface of soil strata, or at the interface between the soil and the structure due to seepage flow (EN 1997-1, 2014). Finally, this process may result in regressive erosion, an increase of voids and a collapse of the soil structure. This failure mode can basically occur in any porous medium subject to seepage flow and is therefore also relevant for tunnels in weak rock without any further adaptions required (see Figure 8.1b).

Piping is defined as a particular form of failure by internal erosion, where the erosion process starts at the surface and regresses until a pipe-shaped channel is formed (EN 1997-1, 2014). In tunnelling, the analogue occurs in case of regressive erosion along discrete features which provide a free surface, such as cracks, joints, karst voids or boreholes (see Figure 8.1c). In such features, high flow velocities can occur. The shape of the initial erosion channel is

defined by the boundaries of the feature, which may also change in case of regressive erosion.

Based on the considerations above, the relevant hydraulic failure modes in deep tunnels are as follows (see Figure 8.1):

- Plug failure;
- Cracking;
- Internal erosion;
- Piping.

While plug failure and cracking are essentially controlled by the seepage forces acting on the rock mass ahead of the tunnel face and the effective stress field in this region, erosion processes such as piping and internal erosion predominately depend on the seepage velocity. None of these failure modes does inevitably lead to a collapse of the tunnel. For example, an overbreak due to plug failure may be limited - or in other words 'self-stabilizing' - by the effect of stress redistribution (arching) around the formed cavity. In this case, the plug ahead of the face may displace to a certain extent, but then stabilize by shear resistance of the ground or of the support measures at the tunnel face (e.g. face bolting). However, the displacement of the plug may increase the ground permeability, thus affecting the hydraulic head field, and allowing for piping or internal erosion at the interface of the plug and the surrounding rock mass due to intensified seepage. The described failure modes rather represent the state of initiation of a failure process (consisting of one particular or a sequence of several mechanisms), which in the worst case can lead to a collapse of the tunnel, or at least to conditions under which the excavation process has to be stopped (e.g. mud or water inflows). During this process, boundary conditions can change over time, e.g. due to limited groundwater re-charge from the surrounding rock mass or due to mitigation measures taken. A general description of this complex process of failure is impossible. Therefore, the thesis at hand focuses on identification of the initial failure mode, potential collapse scenarios and potential mitigation measures. The actually required mitigation measures for specific conditions, thresholds for their timely application and monitoring devices for verifying their adequacy have to be defined specifically for each project.

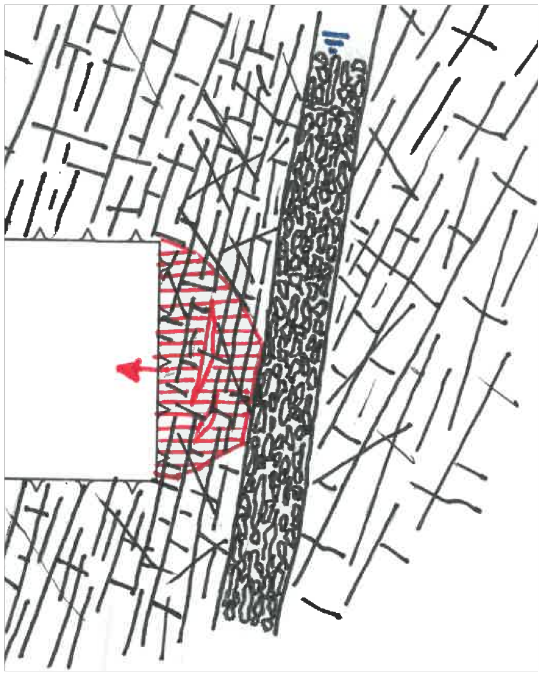

a) Plug failure / cracking

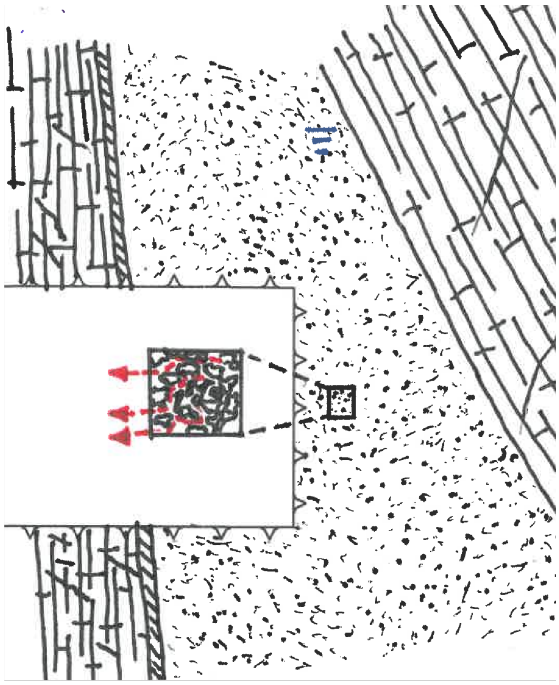

b) Internal erosion

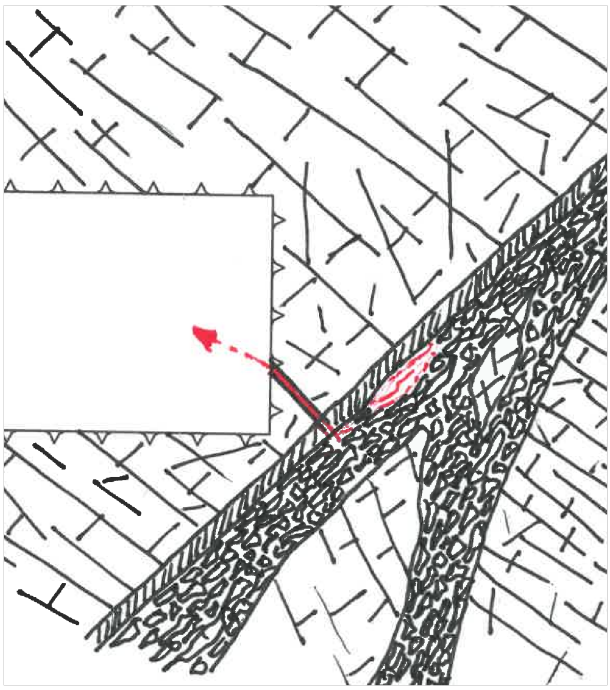

c) Piping

Figure 8.1: Potential mechanisms for flowing ground: a) plug failure and cracking ; b) internal erosion; c) piping

8.3 Plug failure and cracking

8.3.1 Calculation model

Analysis of the failure modes plug failure and cracking requires consideration of seepage forces and effective stress conditions ahead of the tunnel face. During literature review, several analysis models for face stability under seepage flow conditions were identified (see chapter 2). Anagnostou & Kovári (1994) postulated a wedge-and-prism failure mode. Lee et al. (2003) investigated a combination of two cones (see Figure 2.2). In both methods, the failure bodies are assumed monolithic, without checking the internal equilibrium (despite in the connection of the two bodies). However, the results of numerical analyses presented in chapter 7 and a case history from the Semmering base tunnel (Brandtner & Lenz, 2017) indicate a bullet-shaped to hemispherical failure body and the potential formation of tension cracks within this body. The hemispherical shape is traced back to the stress field, which forms an arch around the tunnel face, as shown in Figure 7.3. A numerical back-analysis of the face collapse described in Brandtner & Lenz (2017) is performed to verify the shape of the failure body. Figure 8.2 shows the distribution of the longitudinal displacements of the face and ahead of the face at the stage, when the plug fails and face displacements increase disproportionately. Up to this stage, face displacements are in a range of 2 cm against the direction of excavation, which is considered the 'normal range' of displacement in the objective case, for reference. The iso-surface 'long. disp. =-0.02 m' exhibits an almost hemispherical shape, whereas the iso-surfaces representing larger displacements are rather bullet-shaped, which corresponds to the actual shape of the failed rock mass, as shown on the lower left of Figure 8.2. The vertical displacements at the face and ahead of the face respectively are in a range of ≤ 10 cm and do not show any indications for the formation of a second failure body, such as a chimney-type failure in the crown, subsequent to displacement of the plug.

The calculation model developed for analysing plug and cracking failure is based on following presumptions (see Figure 8.3):

- A hemispherical failure surface is presumed. The radius of the hemisphere is equal to the tunnel radius.
- The method of slices is applied to check internal equilibrium within the failure body and thus to identify formation of (vertical) tension cracks. For this purpose, the failure body is divided into n vertical slices.
- The hemisphere is considered free of stresses, self-weight of the failure body is neglected in the analysis.
- Since no effective stresses occur in the failure body or along the failure surface, the friction angle does not affect the results.
- Cohesion and tensile strength may act as retaining forces in the failure surface and at the interface of two adjacent slices. Furthermore, a support force, e.g. resulting from face bolting, can be considered (provided that the face bolts extend beyond the failure body).
- Cohesion is acting in the lower half of the hemisphere only. This restriction accounts for detaching of the failure body from the surrounding rock mass by gravity and subsequent loss of cohesion in the upper half.
- Seepage forces due to a hydraulic gradient are acting as destabilizing forces on the failure body. They act in horizontal direction (i.e. perpendicular to the face) only. A uniform distribution of the seepage forces over the tunnel face is presumed.

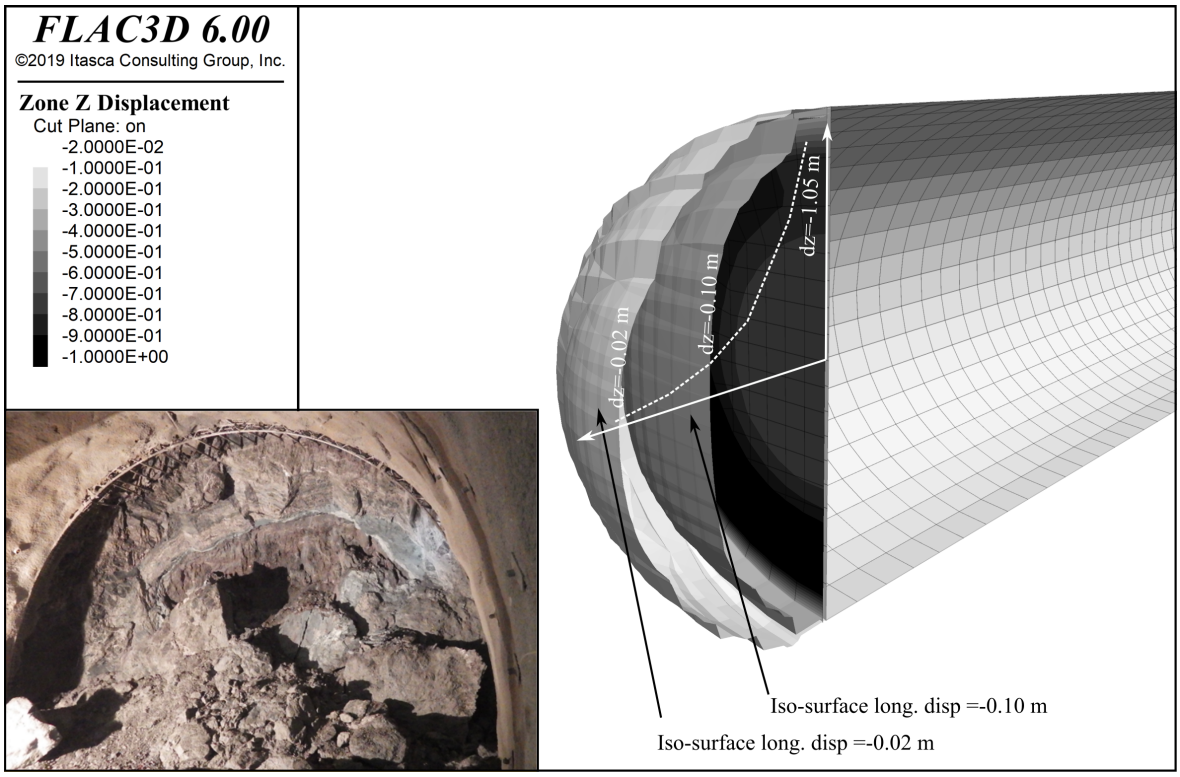

Figure 8.2: Numerical analysis: contour plot of longitudinal face displacements 3 m ahead of a high-permeability fault zone (immediately before failure) and photo of the case history at the Heuberg fault, Semmering base tunnel (ÖBB Infrastruktur AG, 2019)

- In case of homogeneous rock mass, the hydraulic head and gradient can be calculated by the equations presented in chapter 6. For heterogeneous rock mass, a uniform hydraulic head is assumed ahead of the face. To avoid unrealistic hydraulic gradients in heterogeneous rock mass, a linear increase to the initial head is assumed within a longitudinal distance from $x = 0$ to $x = D/10$. The distribution of hydraulic heads is schematically indicated by dotted lines in Figure 8.3.
- The limit state is computed for each slice by formulating the equilibrium in horizontal direction. Equilibrium in vertical direction is not investigated, because no forces act in vertical direction. Moment equilibrium is preconditioned. The latter condition is violated in case of no (or very low) cohesion. However, for the typical range of cohesion in fault rocks (see chapter 5) this condition is satisfied.
- Equilibrium in horizontal direction is checked for each series of adjacent slices, starting with the slice most distant to the face at $x = R$.
- If equilibrium for slice n is not satisfied, the differential force to the limit equilibrium is acting as additional destabilizing force H_{trans} on the slice $n + 1$ (i.e. $H_{trans,n}$ is positive).
- If tension occurs between two adjacent slices (i.e $H_{trans,n}$ becomes zero or negative), a tension crack is considered at the respective position. Equilibrium of the remaining part (slice $n + 1$ until face) is checked to distinguish between cracking (equilibrium satisfied for the remaining part of the plug) and plug failure with tension crack (equilibrium not satisfied for the remaining part).

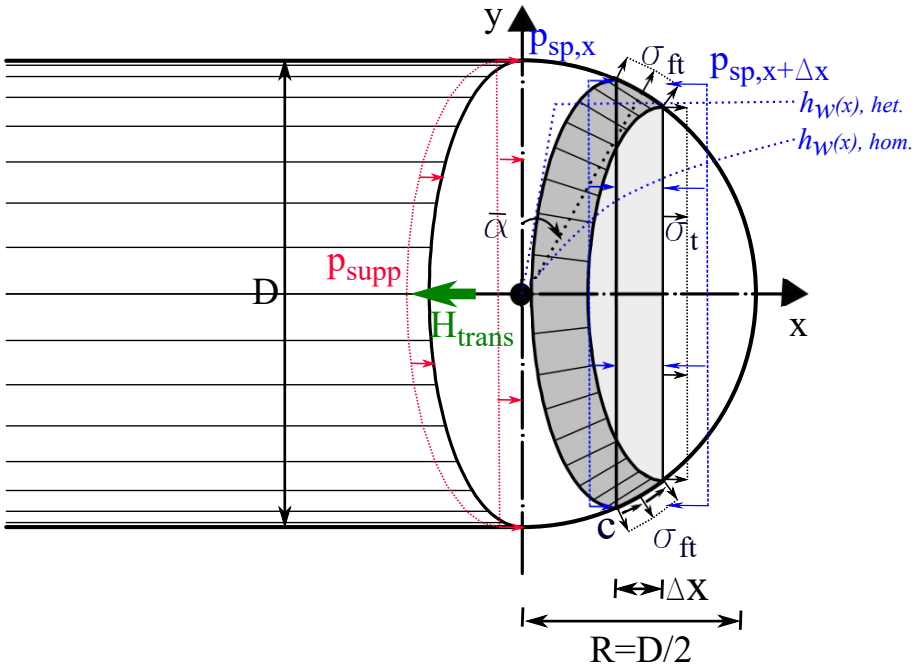

Figure 8.3: Calculation model for face stability analysis with corresponding actions and resistances: σ_{ft}...tensile strength of rock mass; c...rock mass cohesion; p_{sp}...fluid pressure due to hydraulic head h_w; p_{supp}...support pressure on tunnel face

For small values of Δx, the shape of the slices can be approximated by a cone segment. With the above-mentioned assumptions, limit equilibrium can be formulated for slice n as follows:

Geometrical definitions:

$$\bar{x} = x + \frac{\Delta x}{2} \tag{8.1}$$

$$\bar{y} = \sqrt{R^2 - \bar{x}^2} \tag{8.2}$$

$$\bar{\alpha} = \arcsin \frac{\bar{x}}{R} \tag{8.3}$$

$$A_{shell} = 2\pi \cdot \frac{\bar{y}}{cos\bar{\alpha}} \cdot \Delta x \tag{8.4}$$

Stabilizing forces, slice n:

Cohesive force:	$C_h = c \cdot \frac{A_{shell}}{2} \cdot \cos\bar{\alpha}$	(8.5)
Tensile force at shell:	$T_{h,shell} = \sigma_{ft} \cdot A_{shell} \cdot \sin\bar{\alpha}$	(8.6)
Tensile force at slice interface:	$T_{slice} = \sigma_{ft} \cdot \left(R^2 - (x + \Delta x)^2\right) \cdot \pi$	(8.7)
Support force:	$F_{supp} = p_{supp} \cdot R^2 \cdot \pi$	(8.8)

where:
c = Cohesion [MPa]
A_{shell} = Area of hemisphere shell [m^2]
σ_{ft} = Tensile strength of rock mass [MPa]
R = Tunnel radius [m]
p_{supp} = Support pressure at face [MPa]

Destabilizing forces (seepage force), slice n:

$$F_{seepage} = \gamma_w \cdot \left[h_x \cdot (R^2 - x^2) \cdot \pi - h_{x+\Delta x} \cdot \left(R^2 - (x + \Delta x)^2\right) \cdot \pi - h_{x+\Delta x/2} \cdot A_{shell}\right] \quad (8.9)$$

where: γ_w = Specific weight of fluid [MN/m^3]
h_x = Hydraulic head at distance x to the face [m]

The hydraulic head h_x can be calculated according to Equation 6.7 for homogeneous rock mass and Equation 6.10 for heterogeneous rock mass.

Formulation of equilibrium in horizontal direction, slice n:

$$\sum H = -F_{seepage} + C_h + T_{h,Shell} + T_{slice} + H_{trans,n} + H_{trans,n-1} = 0 \quad (8.10)$$

$$H_{trans,n} = F_{seepage} - C_h - T_{h,Shell} - T_{slice} - H_{trans,n-1} \quad (8.11)$$

When $H_{trans,n}$ is positive, it acts as additional destabilizing force on slice n+1. When $H_{trans,n}$ is zero or negative, that is when slices 1 to n are in equilibrium, no force is transferred to slide $n + 1$ and a tension crack is considered at the respective position. In the latter case, external equilibrium of the failure body is only analysed for slices $n + 1$ to m.

External equilibrium, that is equilibrium of the entire hemisphere (in case H_{trans} always remains positive) or the remaining part of the hemisphere (in case a tension crack occurs) is given when the following condition is satisfied. The index n' refers to the slice, where H_{trans} returns a positive value for the first time:

$$\sum_{n'}^{m} \text{Stabilizing forces} \geq \sum_{n'}^{m} \text{Destabilizing forces} + \sum_{n'}^{m} H_{trans(+)} - F_{supp} \quad (8.12)$$

As obvious from Equation 8.12, the support force F_{supp} resulting from face support is solely considered for overall stability and not for the stability of single slices. This approach assumes that face bolts in conventional excavation are usually not pre-stressed ('passive') and require a certain displacement for activation. Therefore, face bolts do not provoke a contact force between two slices, but act only on the entire failure body in case it detaches from the failure surface. In fact, face bolts are fully grouted and therefore may also contribute to the contact forces between two slices. However, this effect is not considered in the analysis.

8.3.2 Verification of calculation model

To verify the developed calculation model described above, fully-coupled numerical analyses are performed for three parameter sets in homogeneous rock mass with varying shear strength and permeability (see Table 8.2). Using the limit equilibrium approach described above, the critical hydraulic head (i.e. the hydraulic head at which limit equilibrium is reached) is 91 m for parameter sets 1 and 2 and 63 m for set 3.

In order to assess the limit state in numerical analyses, a series of calculations with varying stress level and initial hydraulic head is performed for each parameter set. The initial hydraulic head is considered equal to the overburden. In Figure 8.4, the longitudinal displacements of the face (at tunnel axis) are plotted versus the initial hydraulic head. Up to a certain hydraulic head, an approx. linear correlation between the displacements of the face

Parameter set			1	2	3
Lateral pressure coefficient	K_0	[-]	1.0	1.0	1.0
Friction angle	ϕ	[°]	26	35	26
Cohesion	c	[MPa]	0.8	0.8	0.4
Effective weight	γ'	[kN/m^3]	25	25	25
Young's modulus	E	[MPa]	2000	2000	1000
Poisson's ratio	ν_p	[-]	0.25	0.25	0.25
Hydraulic conductivity	k	[m/s]	10^{-8}	10^{-8}	10^{-6}

Table 8.2: Parameter combinations for the verification of the face stability model

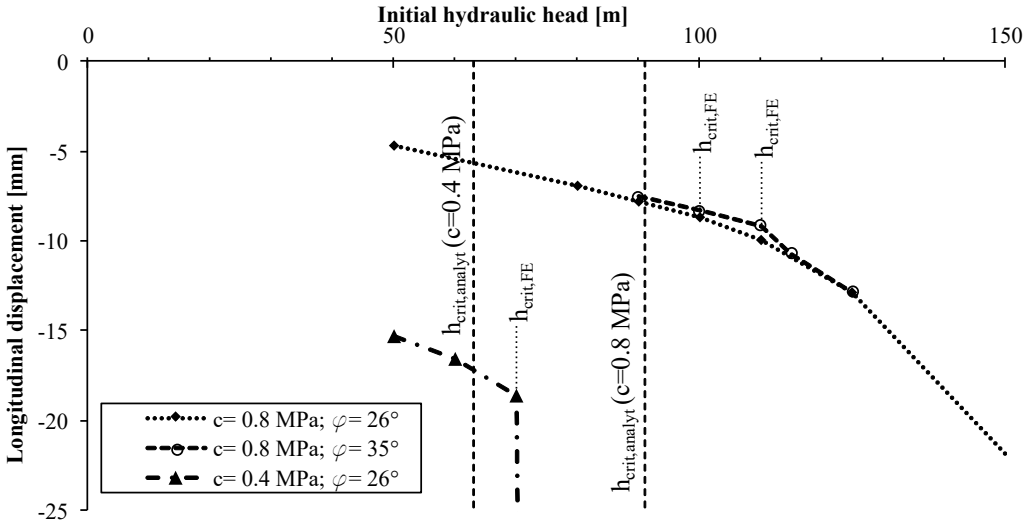

Figure 8.4: Longitudinal displacement of the tunnel face versus the initial hydraulic head for parameter combinations acc. to Table 8.2

and the hydraulic head can be observed. Beyond this level, the displacements increase disproportionately. The hydraulic head at which the displacement curve deviates from a linear trend is considered critical for the respective calculation.

The displacement curves for set 1 and set 3 show a distinct bend at 100 m and 70 m hydraulic head respectively. In competent rock mass (parameter set 2), the transition is rather smooth with a continuous increase of face displacements with increasing hydraulic head. In the latter case, the deviation from a linear progress occurs at a hydraulic head of approx. 110 m.

The critical hydraulic heads calculated in the numerical analyses are 10-20 % higher than from the limit equilibrium calculations. This difference can be explained primarily by the portion of mobilized friction ahead of the face, which is not considered in the analytical calculations. Due to the higher friction angle, the critical hydraulic head for set 2 is 10 % higher compared to set 3 at the same cohesion. The verification study shows that the analytical calculation yields critical hydraulic heads on the safe side, but in the same order of magnitude as the numerical analyses.

8.3.3 Parametric study

For the three material types CGF, MGF and FGF described in chapter 5 (see Table 5.1), the critical hydraulic heads for plug failure and cracking in both, homogeneous rock mass and

heterogeneous rock mass, are determined using the analytical calculation model described above. The case of heterogeneous rock mass refers to a high-permeability fault with a thickness of 10 m and a permeability contrast of two orders of magnitude. The tunnel diameter is 10 m and the advance rate 4 m/d in all calculations. For reference, the critical hydraulic head without consideration of tensile strength is computed. Additionally, the impact of tensile strength of the rock mass is evaluated. The tensile strength is calculated from the shear strength as follows: $\sigma_t = \frac{c'}{tan\phi'}$ (assuming an extension of the MC criterion to the tension side). Finally, the effect of a support force of 2 MN (representing 10 face bolts with a capacity of 200 kN each) is investigated.

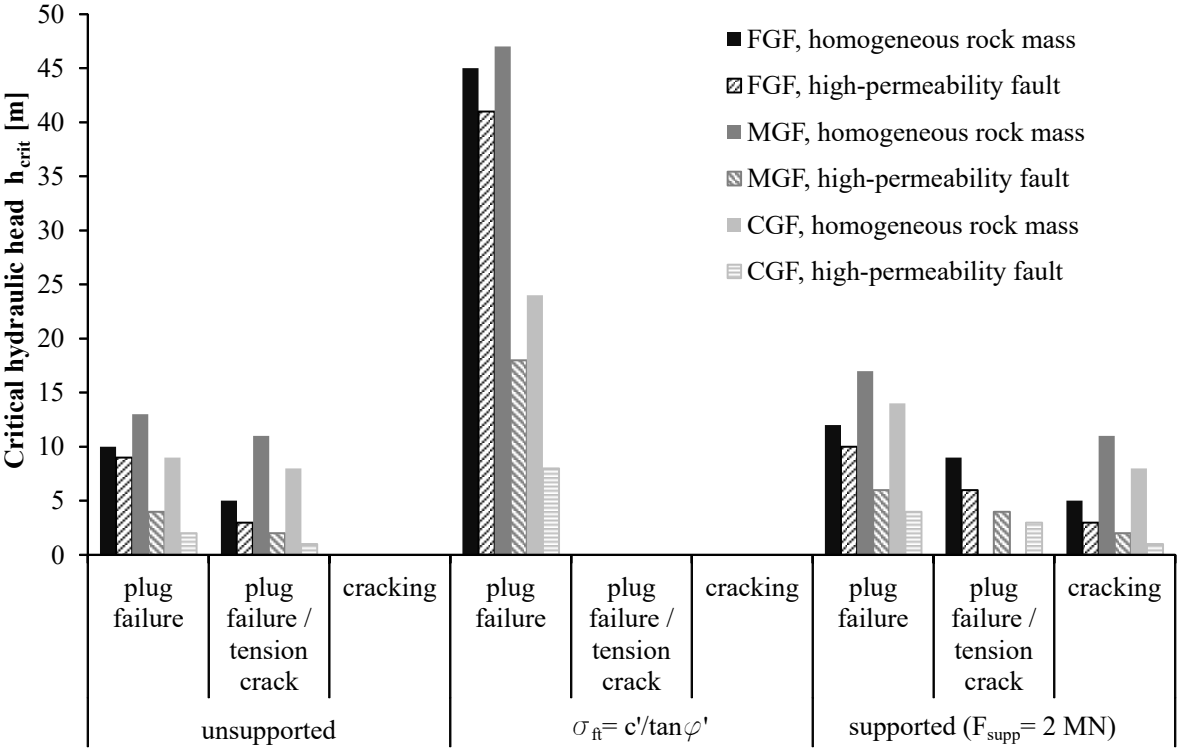

Figure 8.5: Critical hydraulic head for plug failure and cracking in homogeneous rock mass: FGF...fine grained fault material; MGF...medium grained fault material; CGF...coarse grained fault material

Figure 8.5 shows the compiled results of the analyses in form of the critical hydraulic head for the various conditions investigated. For the unsupported case without tensile strength, the critical hydraulic head for plug failure is in a range of 2 - 13 m. When considering a tension crack in the plug, the critical head decreases to 1 - 11 m. Cracking (i.e. tension occurs in the plug but both sides of the plug are in equilibrium) does not occur under the presumed conditions. When considering tensile strength, the calculated critical heads are approx. 5 times higher and a tension crack does not form within the plug.

When considering support force of 2 MN, the critical hydraulic head for plug failure increases to approx. 3 - 17 m. At the same time, cracking may occur at lower heads (1 - 11 m).

For homogeneous conditions, the critical hydraulic head not only depends on the strength parameters, but also on the hydraulic head field ahead of the face and thus on the permeability. Higher permeabilities yield lower hydraulic gradients and are therefore more favourable regarding the objective failure modes. Therefore, the calculation for FGF gives the lowest critical heads. In case of heterogeneous rock mass, the critical head solely depends on cohesion and tensile strength of the rock mass. Due to the low cohesion and tensile strength of

CGF material, this material type gives the lowest critical hydraulic heads and is most susceptible to the investigated failure modes. Generally, plug failure with formation of a tension crack turns out more critical than failure of the entire plug (at zero tensile strength). This outlines the necessity of a calculation model capable of considering this effect.

Generally, the critical hydraulic heads for plug failure and cracking are low compared to the typical overburden and groundwater level in deep tunnels. This emphasizes the requirement of adequate drainage measures for such conditions. The applicability of drainage pipes in fault zones was investigated by Zingg & Anagnostou (2012) and Zingg (2016), who showed that drainage measures can reduce the hydraulic head ahead of the face to approx. 10 % of the initial value.

The results furthermore underline the influence of the tensile strength on face stability. As soon as a tensile strength is considered, the critical hydraulic gradients increase to a multiple value than without consideration of tensile strength. Nevertheless, from an engineering point of view it may not be advisable to rely on the tensile strength of the rock mass due to two aspects: Generally, tensile strength of rock mass is hard to determine and particularly sensitive to heterogeneities such as existing cracks and discontinuities. Hardly any empirical data or relationships exist on the tensile strength. Furthermore, tensile strength can be affected and reduced by fluid flow (e.g. by wash-out of gypsum cementation) or excavation effects (e.g. by formation of new cracks due to blasting).

At the same time, this study points out the potential benefits of ground improvement by grouting. When a certain tensile strength (and at the same time an increase of cohesion) can be provided by grouting, the resistance of the rock mass against plug failure increases significantly. As a basis for grouting design, a nomogram is established, which shows the critical hydraulic head for plug failure and cracking as a function of rock mass cohesion (Figure 8.6). To be on the safe side, the effect of tensile strength is not considered for these calculations. The critical hydraulic head increases more or less linearly with increasing cohesion. Minor deviations from the linear trend result from a change of failure mode (e.g. from plug failure with tension crack to cracking), but are hardly visible in the displayed scale. The nomogram allows for a fast assessment of the rock mass cohesion required to provide stable conditions at a given hydraulic head.

The effect of conventional face support, such as rock bolts, does not raise the critical hydraulic head significantly. Even though the resistance to plug failure slightly increases by bolting, cracking can already occur at lower hydraulic heads, which can trigger erosion and further deterioration of the rock mass quality. Such support measures are therefore not suitable to prevent face instabilities under seepage flow.

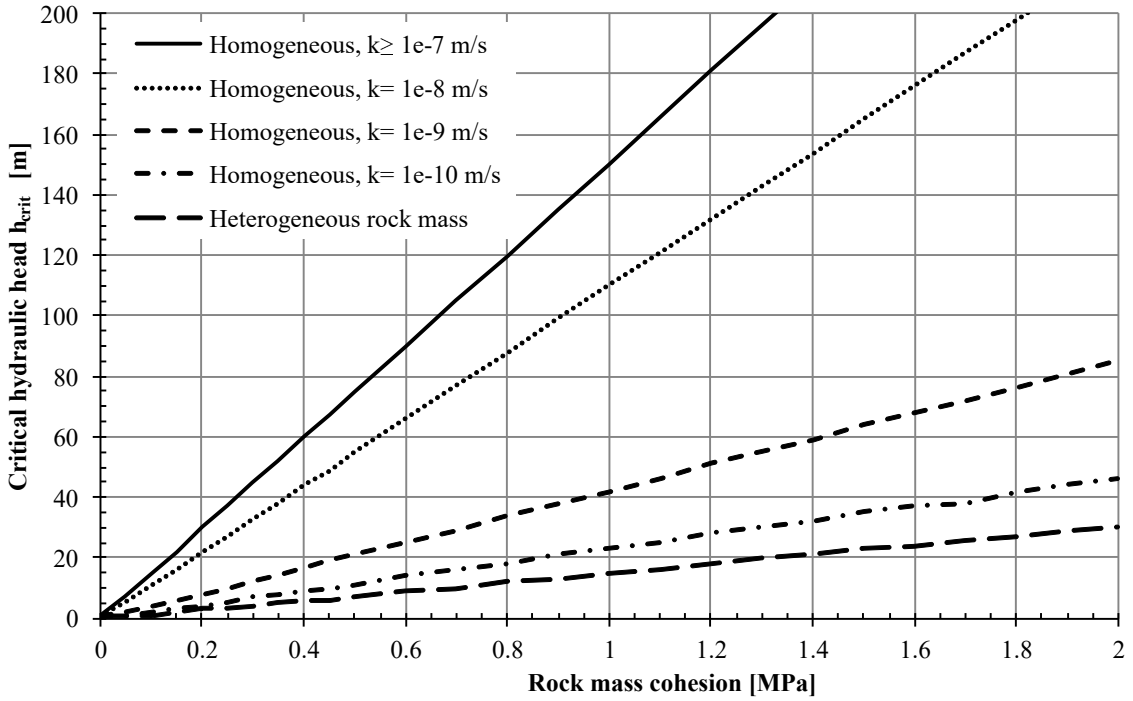

Figure 8.6: Critical hydraulic gradients for plug failure and cracking plotted against rock mass cohesion for both, homogeneous and heterogeneous rock mass (D=10 m)

8.4 Erosion

Within this section, a distinction is made between internal erosion (suffosion), where particle flow occurs within the soil stratum, and piping along already existing features in the rock mass, such as cracks, joints or boreholes.

8.4.1 Calculation model

8.4.1.1 Internal erosion

Internal erosion is a well-known effect in geotechnical engineering, e.g. in the construction of dams, embankments and pits. The limit state for this failure mode is reached when single, fine-grained particles are washed out of the ground matrix by seepage forces. This state not only depends on the hydraulic gradient and the effective shear strength of the ground, but also on the internal structure represented by the grain size distribution. According to EN 1997-1 (2014), filter criteria should be applied to limit the danger of material transport by internal erosion. In case the filter criteria are not met, additional hydraulic criteria should be applied (Saucke, 2006). A compilation of hydraulic criteria targeting internal erosion is provided in Wudtke (2014). The respective equations for evaluating the factor of safety η against internal erosion are summarized below:

Rehfeld (1967):

$$\eta = \frac{1.5 \cdot c}{d_p \cdot (i \cdot \gamma_w - \gamma') \cdot tan\phi} \tag{8.13}$$

Davidenkoff (1976):

$$\eta = \frac{6 \cdot c}{d_p \cdot (i \cdot \gamma_w - \gamma') \cdot tan\phi} \tag{8.14}$$

Müllner (1991):

$$\eta = \frac{6.2 \cdot c}{d_p \cdot i \cdot \gamma_w} \tag{8.15}$$

Zou (2000):

$$\eta = \frac{4 \cdot c + (\sigma_{x0} - i \cdot \gamma_w \cdot d_p) \cdot tan\phi}{2 \cdot \xi \cdot p + (i \cdot \frac{\gamma_w}{T_1} - \gamma')} \tag{8.16}$$

where: η = Factor of safety [-]
c = Effective cohesion [MPa]
ϕ = Effective friction angle [^{o}]
d_p = Equivalent pore diameter [mm]
γ_w = Specific weight of water [MN/m^3]
γ' = Specific dry weight of ground [MN/m^3]
i = Effective hydraulic gradient [-]
σ_{x0} = Lateral stress [MPa]
T_1 = Fabric factor [-]
$\xi \cdot p$ = Shear stress at erosion channel [MPa]

The equations listed above can be reformulated for the limit equilibrium ($\eta = 1.0$). Thus, the critical hydraulic gradient i_{crit} for internal erosion can be evaluated. The equivalent pore diameter can be calculated from the grain size distribution, e.g. as proposed by Busch et al. (1993):

$$d_p = 0.455 \cdot \sqrt[6]{U} \cdot e \cdot d_{17} \tag{8.17}$$

where: d_p = Equivalent pore diameter [mm]
U = Coefficient of uniformity [-]
e = Void ratio [-]
d_{17} = Grain size at 17 mass-% of sieving [mm]

Assuming a linear distribution in semi-logarithmic scale between d_{10} and d_{60}, the grain size d_{17} can be estimated by following equation from the more common values at 10 % and 60 % of sieving (Wudtke, 2014):

$$d_{17} \approx d_{10} \cdot U^{\frac{7}{50}} \approx \frac{d_{60}}{U^{\frac{43}{50}}} \tag{8.18}$$

Busch et al. (1993) propose an equation for the critical hydraulic gradient in coarse grained material, considering also the angle between seepage and gravity and the permeability of the ground:

$$i_{crit} = \phi_0 \cdot \sqrt{\frac{n \cdot g \cdot d_s^2}{\nu \cdot k}} \tag{8.19}$$

With:

$$\phi_0 = 0.6 \cdot (\frac{\rho_d}{\rho_w} - 1) \cdot a^* \cdot sin(30 + \frac{\alpha}{8}) \tag{8.20}$$

$$a^* = 0.82 - 1.8 \cdot n + 0.0062 \cdot (U - 5) \tag{8.21}$$

$$d_s = 0.27 \cdot \sqrt[6]{U} \cdot \frac{n}{n-1} \cdot d_{17} \tag{8.22}$$

where: α = Angle between gravitiy and seepage vector [^{o}]
ρ_d = Specific weight of ground, dry [MN/m^3]
ρ_w = Specific weight of fluid [MN/m^3]
n = Porosity [-]
U = Coefficient of uniformity [-]
d_{17} = Grain size at 17 mass-% of sieving [mm]

For horizontal seepage, the stabilizing component of gravity cannot be taken into account. Therefore, the critical gradients are lower for cases of horizontal seepage. In tunnelling, the highest hydraulic gradients occur perpendicular to the face, that is in horizontal direction (see chapter 6). Therefore, only the decisive case of horizontal seepage flow is considered in the following sections.

The critical hydraulic head for internal erosion under various geotechnical conditions can be calculated by reformulating the equations above with respect to the critical gradient i_{crit} and combining them with the analytical formulations of the hydraulic gradient, that is Equations 6.9 and 6.10 for homogeneous and heterogeneous rock mass respectively.

8.4.1.2 Piping

In contrast to internal erosion, piping requires a discrete feature, acting as a flow channel, along which erosion occurs and regresses further into the rock mass. This feature can either be of natural origin (e.g. cracks or discontinuities in the rock mass) or it can be created artificially during excavation (e.g. boreholes or excavation-induced fractures). Piping may also occur subsequent to an initial cracking or plug failure, e.g. after a tension crack opens and thus provides both, an additional drainage surface and a flow channel. In micro scale, an erosion problem in soil or rock is characterized by the forces acting between the grains or blocks, the particle geometry and the fluid drag force acting on the particle. According to Briaud (2013), the process of erosion in soil or rock is described by following equation:

$$\frac{\dot{z}}{u} = \alpha(\frac{\tau - \tau_c}{\rho u^2})^m + \beta(\frac{\Delta\tau}{\rho u^2})^n + \gamma(\frac{\Delta\sigma}{\rho u^2})^p \tag{8.23}$$

where: $\dot{z}$ = Erosion rate [m/s]
u = Water velocity [m/s]
τ = Hydraulic shear stress [Pa]
τ_c = Threshold for critical shear stress below which no erosion occurs [Pa]
ρ = Mass density of water [kg/m^3]
$\Delta\tau$ = Turbulent fluctuation of hyraulic shear stress [Pa]
$\Delta\sigma$ = Turbulent fluctuation of net uplift normal stress [Pa]

All other quantities are parameters characterizing the soil being eroded. The parameters describing the erosion function can be determined on an experimental basis. However, since

the determination of six parameters at once is required, the above-mentioned function is rather impractical and can be simplified as follows, neglecting the influence of turbulence:

$$\frac{\dot{z}}{u} = \alpha(\frac{\tau - \tau_c}{\rho u^2})^m \tag{8.24}$$

Even when using this simplified erosion function, a consistent physical description of erosion in a porous medium remains a challenging task, because the controlling parameters may interact with each other. As soon as the critical hydraulic shear stress τ_c is exceeded, the permeability and strength of the ground is affected and changes over time. With respect to the high number of unknowns and heterogeneities in rocks and the lack of empirical data, the application of the above-mentioned equation becomes practically impossible. However, the critical hydraulic shear stress τ_c, or the velocity v_c, at which this shear stress occurs, can give a threshold under which no erosion is expected. Briaud (2013) correlates the value of v_c to the mean grain size (see Figure 8.7).

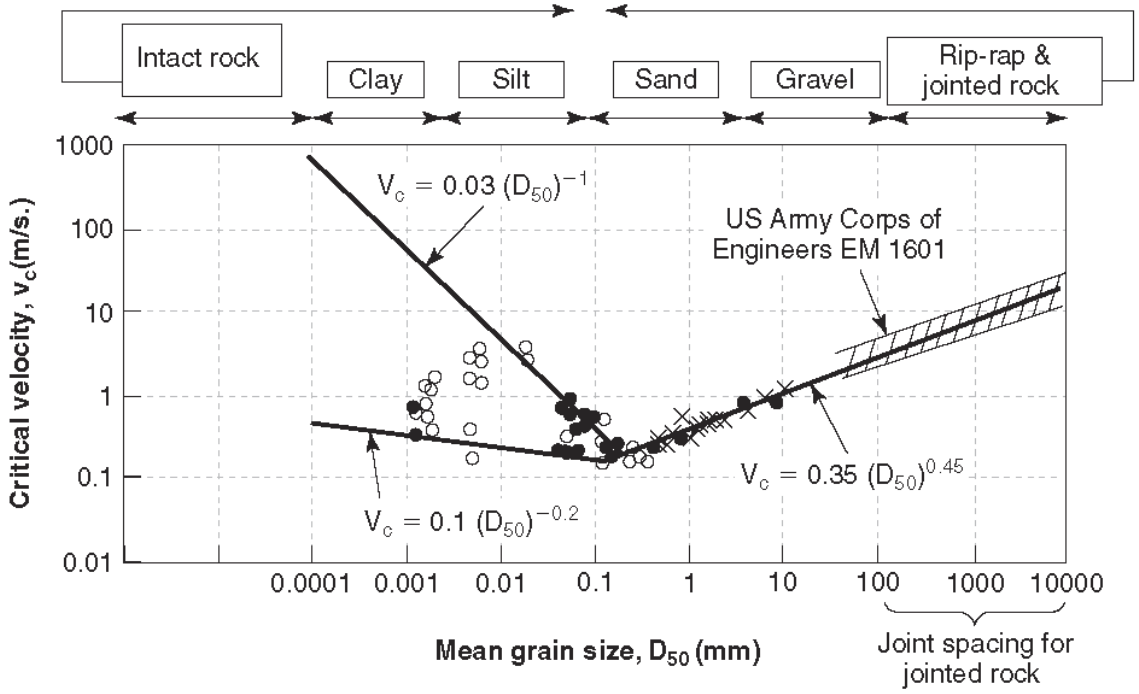

Figure 8.7: Critical velocity for erosion as a function of the mean grain size, from Briaud (2013)

In chapter 6, the concept of filter seepage is used to determine the hydraulic gradients ahead of the face. This concept presumes a fully interconnected pore network, exhibiting a large-scale permeability, and can also be applied to jointed rock mass as a strongly idealized approach (Prinz & Strauss, 2011). Since permeability of fractures and discontinuities usually is several

orders of magnitude higher than the permeability of the rock mass, fluid flow predominantly occurs along the joints. Thus, the real seepage velocity v_s in the discontinuities is significantly higher, depending on the fraction of discontinuities within the ground volume. The actual seepage velocity cannot be determined mathematically since groundwater particle flow can deviate from the one-dimensional flow in any direction. The distance velocity v_d, i.e. the velocity between two adjacent control sections, can be used as a strongly idealized lower threshold of the actual seepage velocity:

$$v_d = \frac{v_f}{n} \tag{8.25}$$

where: v_d = Distance velocity [m/s]
v_f = Filter velocity [m/s]
n = Porosity or volumetric void content [-]

Replacing the porosity by the volumetric fraction of void volume and substituting Darcy's law (Equation 2.4) for the filter velocity, an indicative value for the critical hydraulic gradient for erosion can be evaluated from the critical velocity (see Figure 8.7) and equation 8.25:

$$i_{crit} = \frac{v_{crit} \cdot n}{k} \tag{8.26}$$

where: i_{crit} = Critical hydraulic gradient [-]
v_{crit} = Critical velocity acc. to Figure 8.7 [m/s]
n = Volumetric void content [-]
k = Hydraulic conductivity [m/s]

This equation is based on the assumption of an isotropic network of discontinuities, which is fully interconnected. When Equation 8.26 is exemplarily evaluated for the material types in Table 5.1, the calculated hydraulic gradients are in a range of $3 \cdot 10^5$ - $3 \cdot 10^8$. These critical gradients appear unreasonably high compared to the typical hydraulic gradients calculated in chapter 6, particularly with respect to the case histories (chapter 3) showing that piping can occur already at comparatively low hydraulic heads. This example demonstrates that the concept of an isotropic, fully interconnected fracture network is not suitable for investigating erosion.

To evaluate fluid flow velocities through a feature (crack or borehole), a numerical fluid-flow model is established in FLAC3D. The problem layout consists of a very thin feature layer compared to tunnel dimensions. Modelling the whole tunnel and the surrounding rock mass would require a high degree of discretization and consequently long calculation times. Therefore, model dimensions are reduced to a cube with an edge length of 1 m (see Figure 8.8). Even in these reduced dimensions, modelling a layer with a thickness of < 1 mm would either require a high degree of discretization or otherwise produce distorted elements. Therefore, the feature layer is modelled with a thickness of 1 cm. Assuming that the flow velocity is proportional to the cross section of the feature, the feature conductivity ($k_{feature}$) can be scaled to the ratio of the real ($A_{feature}$) and the modelled cross section (A_{mod}). The modified feature conductivity k_{mod} to be considered in the numerical model is calculated as follows:

$$k_{mod} = k_{feature} \cdot \frac{A_{feature}}{A_{mod}} \tag{8.27}$$

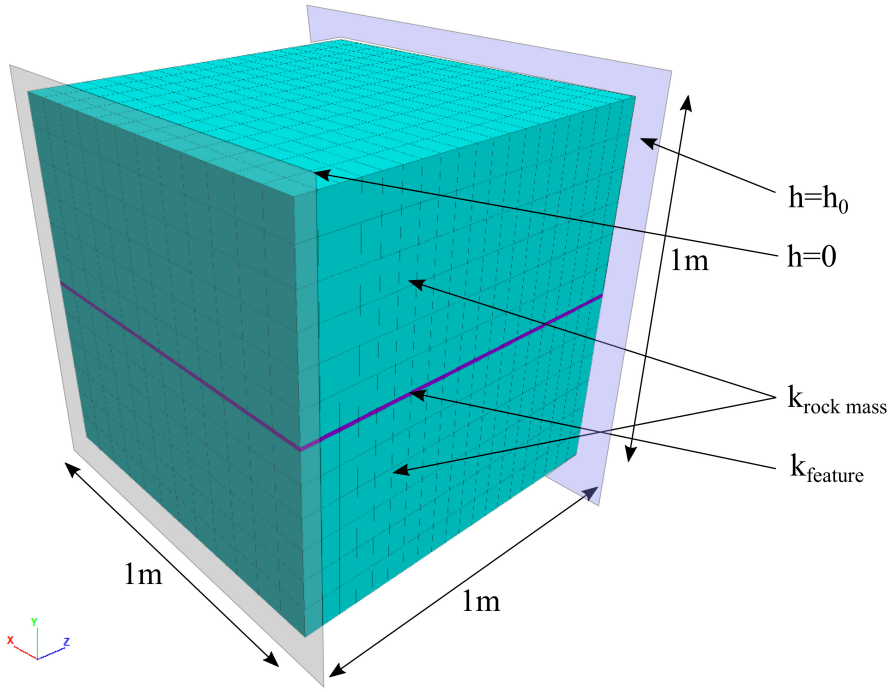

Figure 8.8: Numerical model for calculation of the flow velocities in a discrete feature

The hydraulic boundary conditions of the numerical model are defined by a fully permeable drainage face at atmospheric pressure on one side of the model, simulating the tunnel. On the other side, the pore pressure (or hydraulic head respectively) is fixed to an initial value h_0. Fluid flow is then calculated until steady-state conditions are obtained. The flow velocities are logged in real time during this process. At the beginning of the calculation, higher flow velocities occur, which decrease by dissipation of the hydraulic gradients until the steady state is reached. The calculation returns a range of flow velocities in the feature and the total time required for reaching the steady state.

For planar features, such as cracks and joints, the conductivity depends on the third power of the feature aperture. The equation of Heitfeld & Koppelberg (1981) (cited from Langguth & Voigt (2004)) is applied:

$$k_{feature} = \frac{g \cdot (2a)^2}{12\nu \cdot (1 + 8.8 \cdot (k_r/d_h)^{1.5})} \tag{8.28}$$

where: a = Aperture of feature [m]
g = Gravity [m/s^2]
ν = Kinematic viscosity of fluid [m^2/s]
k_r = Absolute roughness of feature surface [m]
$d_h = 2 \cdot 2a$ = Hydraulic diameter of feature [m]

As displayed in Figure 8.9, an aperture of 0.2 mm yields a feature conductivity of 10^{-5} m/s, which is already one order of magnitude higher than the upper range of typical permeabilities in fault zones (see chapter 5). The calculation is based on a roughness of $k_r = 6$ mm. Typical values of k_r range from 4 mm (e.g. slickensides) to 15 mm for rough joints.

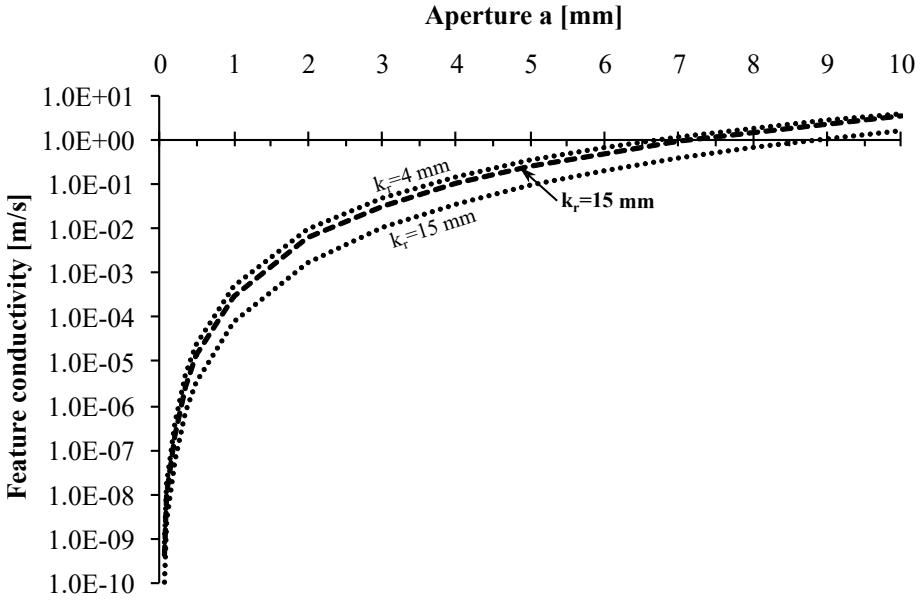

Figure 8.9: Hydraulic conductivity of a planar feature as a function of aperture according to Heitfeld & Koppelberg (1981)

For a circular feature (e.g. borehole) the conductivity can be calculated by adapting the flow equation of Prandtl-Colebrook to the concept of filter velocity, as proposed by Zingg (2016):

$$k_{feature} = -2 \cdot log\left(\frac{2.51 \cdot \nu}{d_{dr} \cdot \sqrt{2g \cdot d_{dr} \cdot i}} + \frac{k_r}{3.71 \cdot d_{dr}}\right) \cdot \sqrt{\frac{2g \cdot d_{dr}}{i}} \tag{8.29}$$

where: d_{dr} = Diameter of drainage hole [m]
ν = Kinematic viscosity of fluid [m^2/s]
k_r = Absolute roughness [m]
i = Hydraulic gradient along borehole axis [-]

Figure 8.10 shows the permeability of a circular feature for typical borehole diameters and selected hydraulic gradients. The calculation is based on a roughness of $k_r = 6\,\text{mm}$ for a smooth borehole.

In addition to the numerical calculations, the flow velocity is calculated analytically. Darcy's law with the permeabilities as per Equation 8.28 and 8.29 is used to calculate the respective flow velocities:

$$v_{feature} = k_{feature} \cdot i \tag{8.30}$$

where: $v_{feature}$ = Flow velocity in discrete feature [m/s]
$k_{feature}$ = Hydraulic conductivity of discontinuity (Eq. 8.28) or borehole (Eq. 8.29) [m/s]
i = Hydraulic gradient in feature [-]

Figure 8.11 shows the computed flow velocities in a planar feature with various aperture for both, numerical and analytical calculations. At an initial head of 100 m, the flow velocity

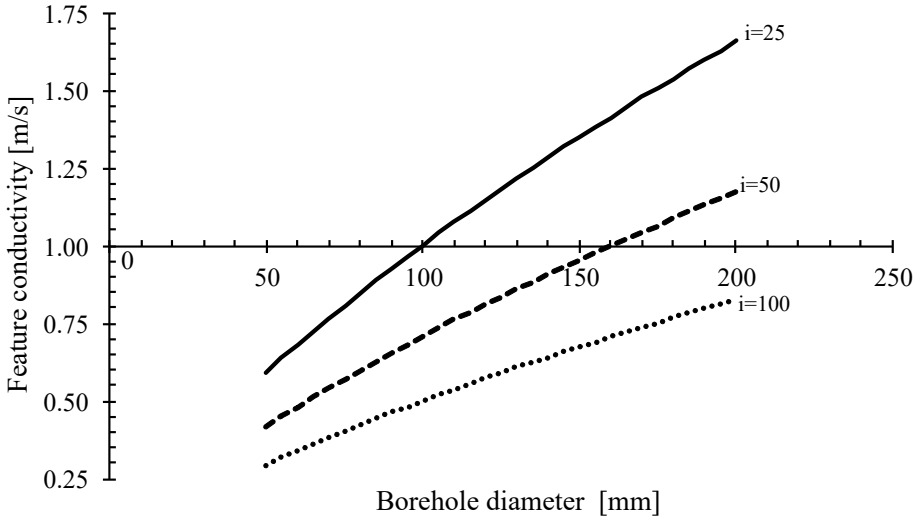

Figure 8.10: Hydraulic conductivity of a circular feature as a function of diameter for k_r = 6 mm

for a feature conductivity of 10^{-2} m/s decreases from initially 6.2 m/s to 1.7 m/s, the steady state is reached within 5 seconds. In case of a feature conductivity of $4 \cdot 10^{-3}$ m/s, the time to reach the steady state is approx. 3 minutes, flow velocity decreases from 2.0 m/s to 0.6 m/s. In case of a feature conductivity of 10^{-5} m/s, flow velocities are close to zero. The evaluation of the time required to reach the steady state shows that flow velocities higher than at steady state prevail for a short time only. Different rock mass permeabilities are modelled to investigate whether fluid flow proceeds through the feature only or whether a relevant portion also proceeds through the rock mass itself. The difference in flow velocity for a rock mass conductivity of 10^{-6} m/s and 10^{-8} m/s is approx. 8 % at steady state. This comparison indicates that the predominant part of seepage flow occurs in the feature.

The analytical calculations based on Darcy's law give flow velocities approx. 40 % lower compared to the numerical calculations. The difference can be explained by the distribution of the hydraulic gradient within the model boundaries. The analytical calculation is based on a hydraulic gradient $i = h_0/1m$. In the numerical calculations, the distribution of the gradient over the longitudinal extent of the model is not linear, but the gradient increases towards the boundary where atmospheric conditions are presumed. That is, flow velocities increase towards the face. The calculations show that flow velocities in a planar feature to a great extent depend on it's aperture. In practice, this parameter is impossible to determine reliably beforehand. A geological assessment of joint width usually is limited to assigning a certain range. From this point of view, assessing potential for piping is rather a matter of orders of magnitude. Thus, the difference between numerical and analytical calculations is acceptable from an engineering point of view. For sake of simplicity, the analytical approach as per Equation 8.30 is used for further considerations.

Boreholes exhibit permeabilities (and thus flow velocities) that are several orders of magnitude higher than those of the planar features investigated above (see Figure 8.10) and are consequently more susceptible to piping. On the other hand, boreholes can be lined or in the worst case grouted to prevent regressive erosion (provided adequate drilling and grouting equipment is available). Consequently, piping in boreholes largely depends on process-specific details. The calculation of critical hydraulic heads and gradients, presented in the following sections, is therefore limited to planar features (although the presented analytical framework basically allows for consideration of circular features as well).

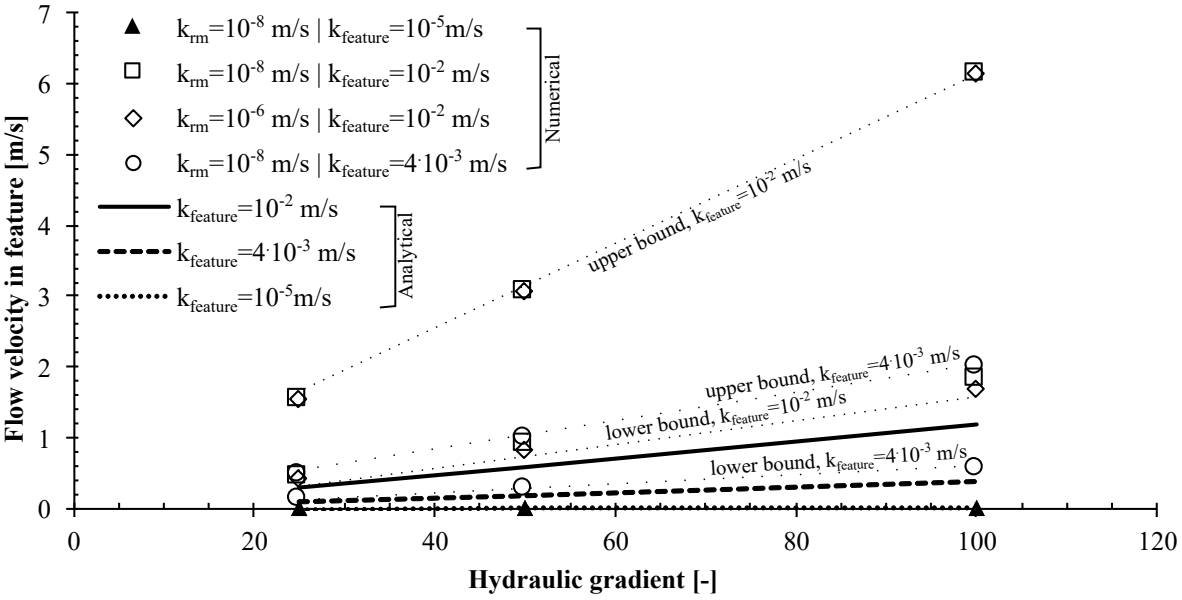

Figure 8.11: Range of flow velocities in features from numerical and analytical calculations for various hydraulic conductivities

The critical hydraulic gradient for piping is calculated from the critical velocity, under which no erosion is expected (see Figure 8.7), and the hydraulic conductivity of the respective feature:

$$i_{crit} = \frac{v_{crit}}{k_{feature}} \tag{8.31}$$

where: i_{crit} = Critical hydraulic gradient [-]
v_{crit} = Critical velocity acc. to Fig. 8.7 [m/s]
$k_{feature}$ = Hydr. conduct. of planar feature (Eq. 8.28) or borehole (Eq. 8.29) [m/s]

The critical hydraulic head for piping under various conditions can be assigned by combining the equations for the critical gradient i_{crit} above with the analytical formulations of the hydraulic gradient, that is Equation 6.9 and 6.10 for homogeneous and heterogeneous rock mass respectively.

It is acknowledged that this approach represents a strongly idealized model of the actual erosion process by several reasons:

- The critical velocity, used as a threshold for piping, is derived empirically for soils (and not for fault rocks). Particularly, effects of tensile strength (e.g. by chemical bonding) cannot be accounted for. Empirical data regarding the erosion of fault rocks could not be found in literature.
- The criterion of critical velocity does not account for mechanical strength parameters. The effects of ground improvement can therefore not be considered.
- A geological prediction of the actual feature geometry is practically impossible.
- Darcy's law is assumed for the fluid flow in the feature. Strictly, this assumption only holds for laminar flow (Prinz & Strauss (2011)).
- A constant feature permeability is assumed. In reality, piping would immediately increase the feature permeability.

- It is presumed that the small-scale permeability of the feature does not affect the hydraulic head field around the tunnel. The latter is solely controlled by the large-scale rock mass permeability. In reality, the hydraulic head field around the tunnel largely depends on the extents of the feature (i.e. persistence of the feature and length of the drainage path) and will be distorted by feature permeabilities, which are significantly higher than that of the rock mass. However, the extent and aperture of geological features cannot be determined reliably beforehand. Therefore, a more detailed assessment of the hydraulic head field including the effect of a highly permeable feature is not possible at this point.
- A constant hydraulic head is assumed on the 'wet side' of the model. In reality, this condition is not necessarily met. Rather, fluid flow through the feature would cause a transient drawdown ahead of the tunnel face and hydraulic gradients would change over time.

For a better understanding of erosion processes in fault rocks, further scientific research is essential. Experimental data of erosion in fault rocks and specific numerical analyses (e.g. modelling of particle flow) may allow to establish a suitable constitutive law to describe erosion processes more accurately. At this point, a significant research demand remains for future contributions.

8.4.2 Parametric study

For the selected material types CGF, MGF and FGF shown in Table 5.1, the critical hydraulic gradient i_{crit} for internal erosion is calculated as per Equations 8.13 - 8.16 and 8.19. The corresponding hydraulic gradients are displayed in Figure 8.12.

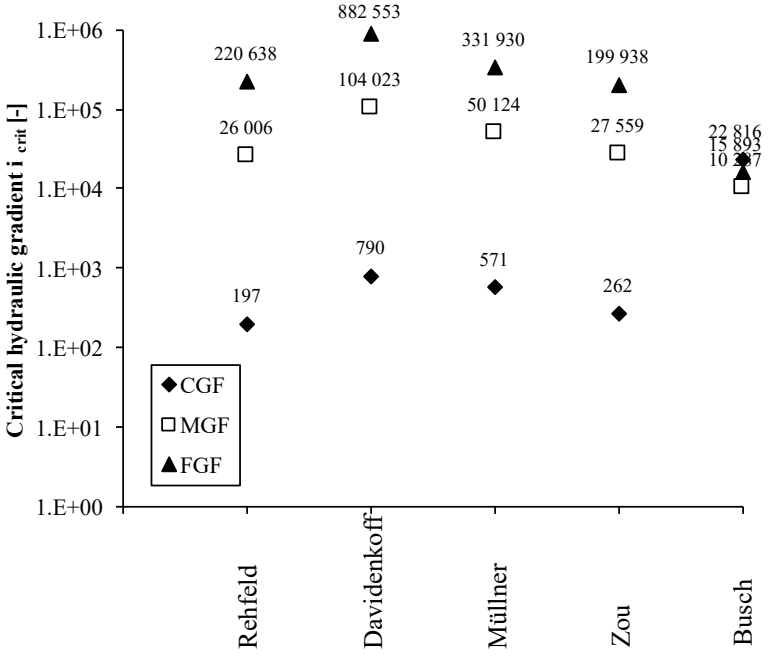

Figure 8.12: Critical hydraulic gradients for internal erosion, calculated for selected fault materials: FGF...fine-grained fault material; MGF...medium-grained fault material; CGF...coarse-grained fault material

Coarse-grained material (CGF) evidently provides the lowest resistance against internal erosion. The critical hydraulic gradients for medium- to fine-grained materials (MGF, FGF)

are higher by several orders of magnitude. In practice, internal erosion can be ruled out as potential failure mode at least for medium- to fine-grained material, since hydraulic gradients in this order of magnitude practically do not occur in conventional tunnelling. The calculations confirm the common assumption that coarse-grained materials with low (or no) cohesion are most prone to internal erosion (Sausgruber & Brandner, 2003; Sattler, 2018), whereas medium- to fine-grained materials are not particularly susceptible to this failure mode (Wudtke, 2014). For coarse-grained materials the criterion of Rehfeld (1967) (equation 8.13) gives the most conservative hydraulic gradients and is therefore applied as failure criterion in the following analyses to obtain results on the safe side.

The calculation of the critical hydraulic gradient does not allow an assignment to specific geotechnical conditions such as homogeneous rock mass with different permeabilities or heterogeneous rock mass. To allow for comparison to the previously described results for plug failure and cracking, a relation to the absolute hydraulic head is required. For homogeneous rock mass, the hydraulic gradient can be described as the first derivative of the hydraulic head field (see Equation 6.9). The critical hydraulic head for homogeneous rock mass according to Rehfeld (1967) can be calculated by following equation (with K^* and D^* according to chapter 6):

$$h_{crit} = \frac{i_{crit}}{K^* \cdot D^*} = \frac{1.5 \cdot c}{d_p \cdot \gamma_w \cdot tan\phi \cdot K^* \cdot D^*} \tag{8.32}$$

where: h_{crit} = Critical hydraulic head [m]
c = Cohesion [MPa]
d_p = Equivalent pore diameter (Eq. 8.17) [mm]
γ_w = Specific weight of fluid [MN/m^3]
ϕ = Friction angle [^{o}]
K^* = Curve fitting parameter acc. to Fig. 6.8 [-]
D^* = Curve fitting parameter acc. to Eq. 6.8 [-]

For heterogeneous rock mass, the hydraulic gradient can be evaluated by combining the criterion acc. to Rehfeld (1967) and Equation 6.10. Solving for the critical hydraulic head, the equation is re-formulated as follows (with A and B according to chapter 6):

$$h_{crit} = \frac{i_{crit}}{A \cdot (1 - e^{-B \cdot t})} = \frac{1.5 \cdot c}{d_p \cdot \gamma_w \cdot tan\phi \cdot A \cdot (1 - e^{-B \cdot t})} \tag{8.33}$$

where: h_{crit} = Critical hydraulic head [m]
c = Cohesion [MPa]
d_p = Equivalent pore diameter (Eq. 8.17) [mm]
γ_w = Specific weight of fluid [MN/m^3]
ϕ = Friction angle [^{o}]
A, B = Curve fitting parameter acc. to Tab. 6.3 [-]

From Equations 8.32 and 8.33, the critical hydraulic heads for various geotechnical conditions are calculated. Excavation diameter and advance rate are kept constant at D = 10 m and $v_{advance}$ = 4 m/d. As elaborated above, internal erosion is particularly relevant for coarse-grained materials. Therefore, calculations are conducted for CGF material type only. Since

this material type exhibits a comparatively high permeability, the calculations for homogeneous rock mass are limited to hydraulic conductivities $\geq 10^{-7}$ m/s. For heterogeneous rock mass, different hydraulic contrasts and fault zone widths are investigated. From equations 8.32 and 8.33 it is obvious that the critical hydraulic head linearly depends on the rock mass cohesion. An increase in cohesion can for instance be achieved by grouting. To show the potential benefit of an increase in cohesion, a range of cohesion is investigated, whereas the friction angle is kept constant ($\phi = 35^o$). The results of the parametric study are shown in Figure 8.13.

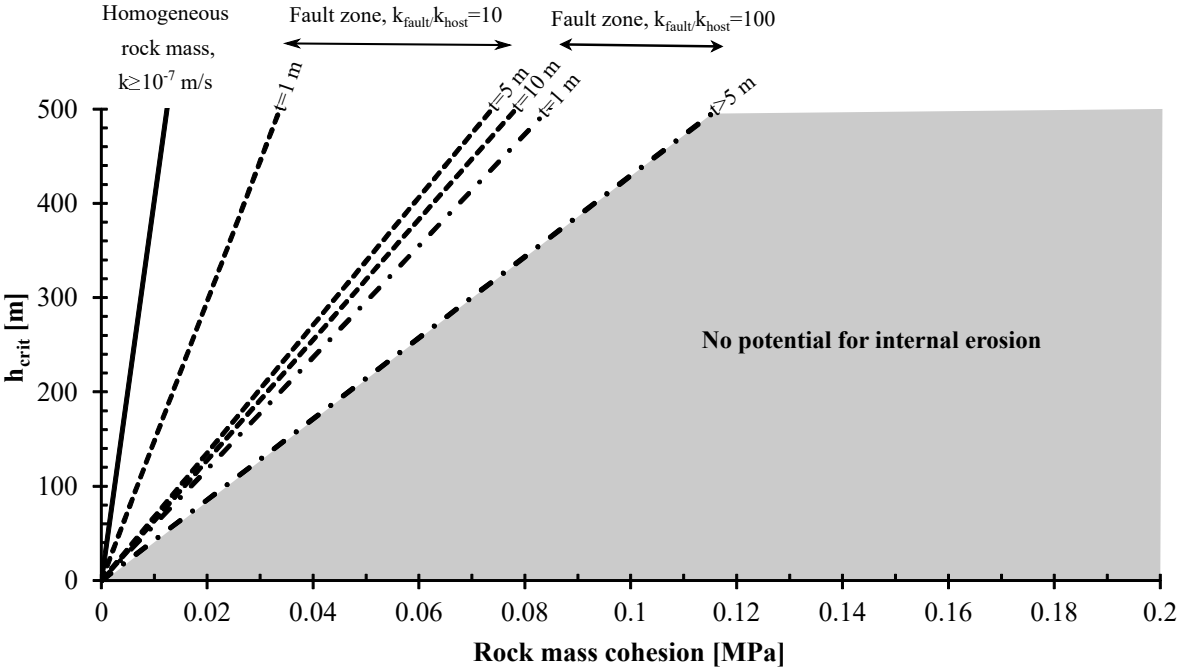

Figure 8.13: Critical hydraulic heads for internal erosion (suffosion) in homogeneous and heterogeneous rock mass in coarse-grained fault material

The critical hydraulic heads for homogeneous rock mass are comparatively high already at low values of cohesion, because hydraulic gradients are significantly lower than in heterogeneous rock mass. The most critical conditions evolve in fault zones with a thickness of more than 5 m and a permeability contrast of two orders of magnitude or higher. In such cases, the hydraulic head in the fault zone is more or less equal to the initial hydraulic head (see chapter 6). Below the critical heads for these conditions no potential for internal erosion is expected, as indicated in Figure 8.13. Strictly, the presented results are valid for one distinct material type (CGF) only. However, since mechanical parameters and grain size distribution for this material type are based on conservative assumptions, the calculated values can (carefully) be used as indicative limits for a fast assessment of potential failure modes.

The critical hydraulic heads for piping along planar features are calculated based on the critical velocities under which no erosion occurs as per Figure 8.7). The critical velocities for the investigated material types are summarized in Table 8.3.

Figure 8.14 shows the flow velocity in planar features with selected permeability in conjunction with the critical velocities as per Table 8.3. As elaborated in section 8.4.1, the lower bound of flow velocity is considered decisive, since higher velocities prevail over a short time only. For coarse-grained materials a hydraulic conductivity of $k_{feature} = 10^{-2}$ m/s or higher is required to produce flow velocities higher than v_{crit} (in reasonable ranges of hydraulic gradients). This feature conductivity corresponds to an aperture of approx. 0.5 mm. Erosion of

			CGF	MGF	FGF
Mean grain size	d_{50}	[mm]	17	0.6	0.05
Critical velocity	v_{crit}	[m/s]	1.3	0.3	0.2

Table 8.3: Critical velocities under which no erosion occurs acc. to Briaud (2013) for selected fault materials: FGF...fine-grained fault material; MGF...medium-grained fault material; CGF...coarse-grained fault material

medium- to fine-grained material may occur already at low hydraulic gradients and features of small aperture ($k_{feature} = 5 \cdot 10^{-3}$ m/s corresponds to an aperture of 0.1 mm). In features with apertures of lower orders of magnitude no relevant flow velocities can occur.

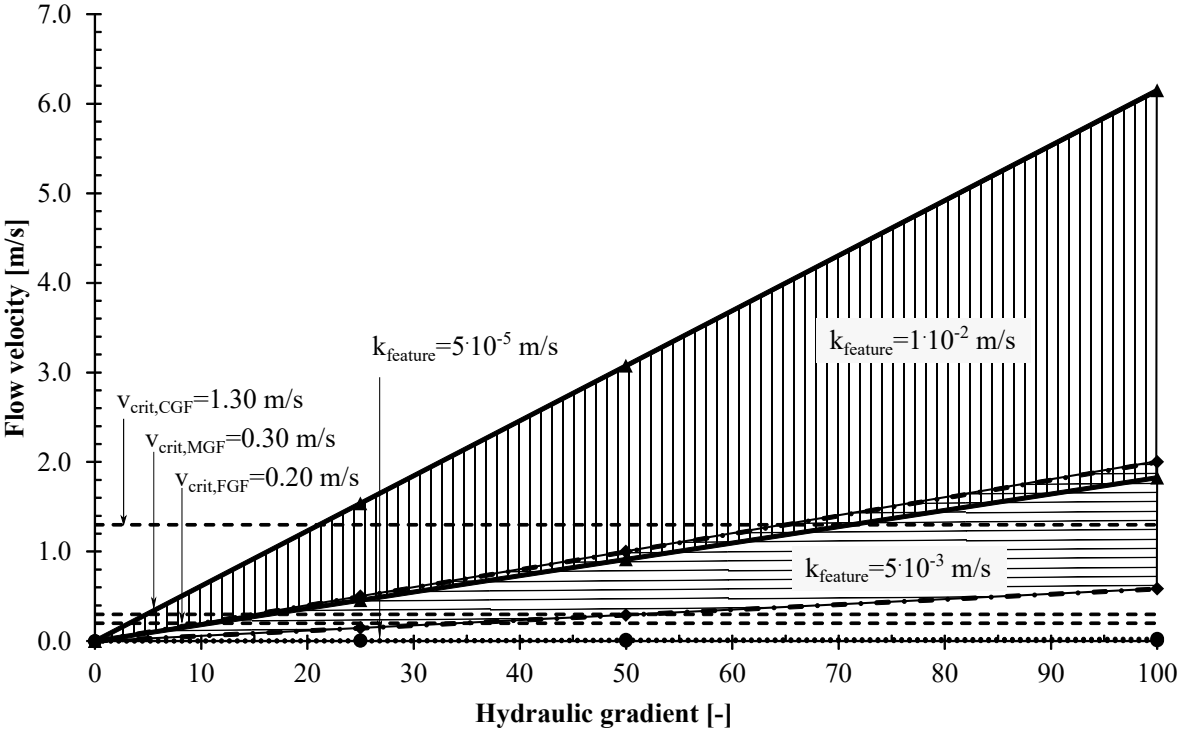

Figure 8.14: Range of flow velocities in features for various hydraulic conductivities

The critical hydraulic heads for various geotechnical conditions can be calculated by combining Equation 8.31 with Equations 6.9 and 6.10 for homogeneous and heterogeneous rock mass respectively. The application of these equations presumes that the small-scale permeability of the planar features does not affect the large-scale permeability of the rock mass and thus the large-scale distribution of hydraulic heads.

Homogeneous rock mass:

$$h_{crit} = \frac{i_{crit}}{K^* \cdot D^*} = \frac{v_{crit} \cdot 12\nu \cdot (1 + 8.8 \cdot (k_r/d_h)^{1.5})}{K^* \cdot D^* \cdot g \cdot (2a)^2} \tag{8.34}$$

Heterogeneous rock mass:

$$h_{crit} = \frac{i_{crit}}{A \cdot (1 - e^{-B \cdot t})} = \frac{v_{crit} \cdot 12\nu \cdot (1 + 8.8 \cdot (k_r/d_h)^{1.5})}{A \cdot (1 - e^{-B \cdot t}) \cdot g \cdot (2a)^2} \tag{8.35}$$

where:
h_{crit} = Critical hydraulic head [m]
v_{crit} = Critical velocity acc. to Fig. 8.7 [m/s]
a = Aperture of feature [m]
g = Gravity [m/s^2]
ν = Kinematic viscosity of fluid [m^2/s]
k_r = Absolute roughness of feature surface [m]
$d_h = 2 \cdot 2a$ = Hydraulic diameter of feature [m]
K^* = Curve fitting parameter acc. to Fig. 6.8 [-]
D^* = Curve fitting parameter acc. to Eq. 6.8 [-]
A, B = Curve fitting parameter acc. to Tab. 6.3 [-]

Figure 8.15 shows the calculated ranges of critical heads for planar features with various aperture in homogeneous and heterogeneous rock mass. All values are calculated for a tunnel diameter of D = 10 m, an excavation rate of 4 m/d and a roughness of the feature surface of $k_r = 6$ mm. The lower bound of the range is formed by the values for heterogeneous rock mass (due to higher hydraulic gradients). The upper bounds represent piping in homogeneous rock mass. Fine-grained materials are more susceptible to erosion due to the lower weight of the grains, which are thus transported by seepage more easily. In open joints (i.e. joints with an aperture of ≥ 0.5 mm) piping can already occur at low initial heads in fine- to medium-grained fault rocks, whereas in coarse-grained fault material piping occurs at hydraulic heads > 100 m. For combinations of aperture and hydraulic head below the lower bound of FGF, no relevant potential for piping is given. As elaborated for internal erosion, the calculated values are strictly valid for specific material types only. However, as representative material types are chosen, the calculated values may be (carefully) used as indicative limits for a fast assessment of the hydraulic failure mode.

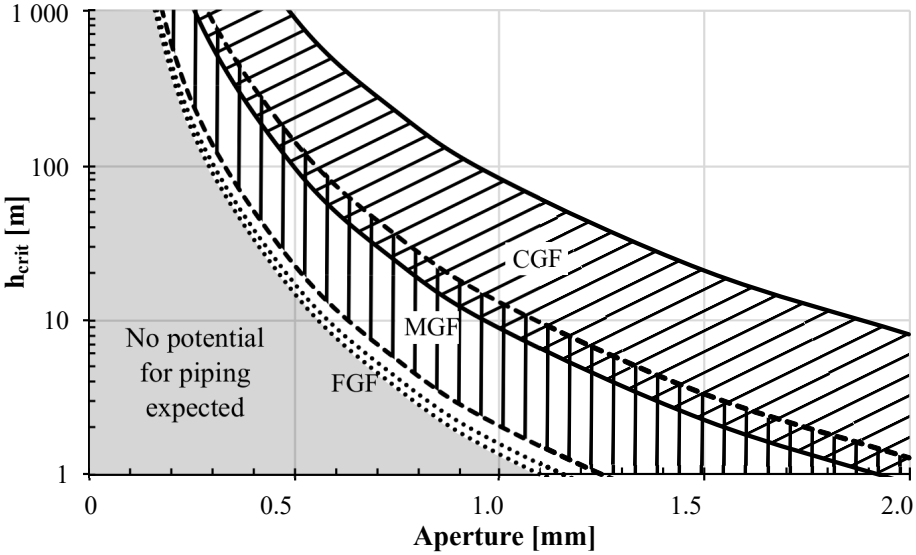

Figure 8.15: Range of critical hydraulic heads for piping along planar features: FGF...fine-grained fault material; MGF...medium-grained fault material; CGF...coarse-grained fault material

Similar to plug failure, cracking and internal erosion, possible measures to prevent or mitigate piping are drainage and grouting. The effect of grouting cannot be adequately assessed in the above-mentioned framework of equations. Grouting basically provokes a closing (or at least a reduction of aperture) of joints and thus a reduction of flow velocity. The efficiency

of grouting measures not only depends on geotechnical properties (e.g. joint aperture), but also on a number of process-specific factors, such as viscosity and composition of the grout, injection pressure, pump rate etc. A general mechanical description of this process is therefore not possible. Drainage facilitates the dissipation of high hydraulic gradients and therefore reduces the erosion potential. However, during construction it has to be assured that no erosion occurs along the borehole, e.g. by adequate, erosion-stable borehole linings, and that the borehole can be sealed in the worst case. Otherwise, the borehole itself may induce or amplify piping processes.

When comparing the two different erosion processes investigated, piping along discrete features within the rock mass occurs at significantly lower hydraulic heads than internal erosion. Particularly in fault zones, cracks and joints are omnipresent features of the rock mass (see chapter 5). Consequently, piping is the major source for severe material inflow into tunnels (flowing ground). This is also emphasized by the fact that a major part of the case histories presented in chapter 3 can be traced back to piping processes.

8.5 Comparison of failure modes

The above-mentioned analytical approaches allow for a comparison of the critical hydraulic heads for the respective hydraulic failure modes under various geotechnical conditions. This study should assist in determining the initial failure mode. The computed critical hydraulic heads for the four hydraulic failure modes described above are displayed in Figure 8.16.

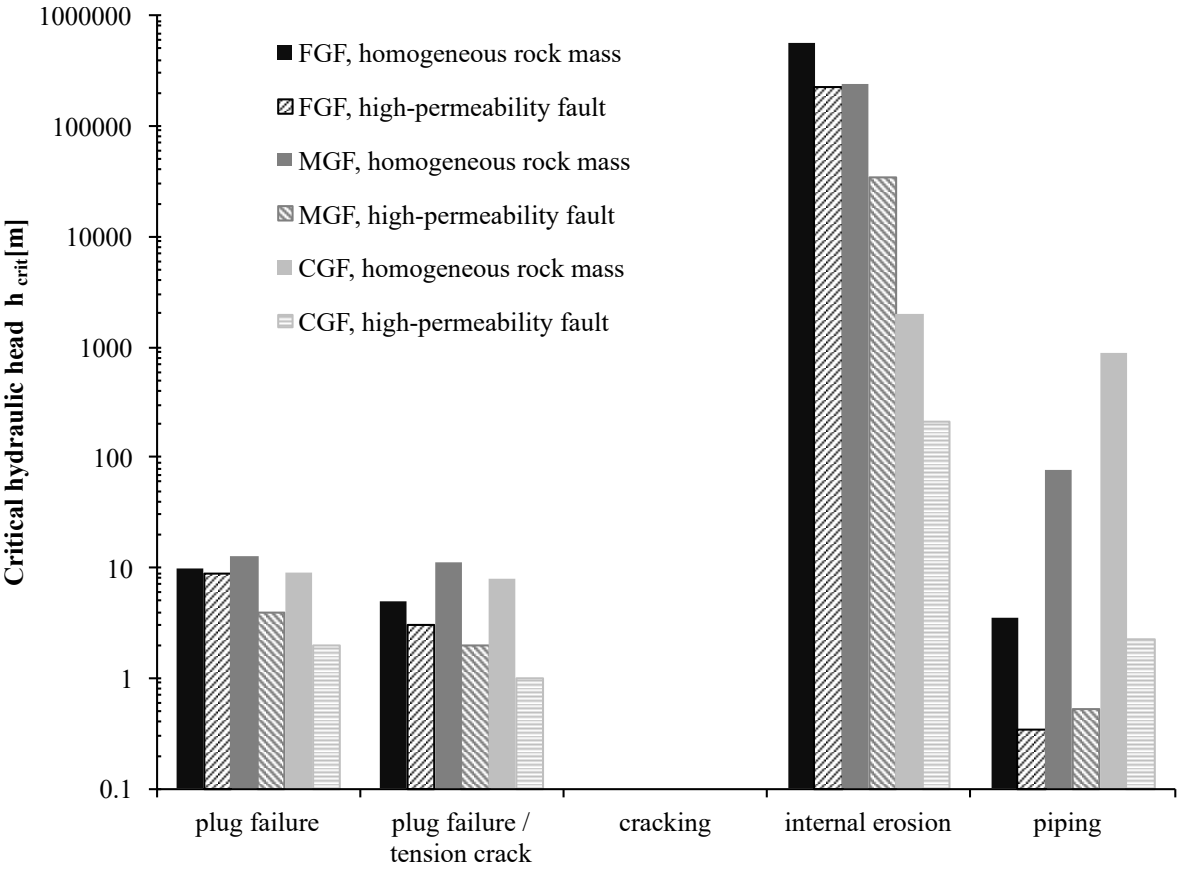

Figure 8.16: Critical hydraulic heads for hydraulic failure modes; FGF...fine-grained fault material; MGF...medium-grained fault material; CGF...coarse-grained fault material

Independently of the material type, plug failure (with consideration of a tension crack) and piping yield the lowest critical hydraulic heads. Cracking (i.e. tensile failure within the plug with both sides of the failure body remaining stable due to cohesion/tensile strength) does not occur under the assumed conditions, which can be explained by the low cohesion and the lack of tensile strength. Internal erosion can practically be ruled out as potential failure mode with respect to the high critical heads. Although a different problem layout was investigated, this finding is in line with the conclusions of Wudtke & Witt (2010) and Wudtke (2014), who showed that hydraulic failure in cohesive soils rather starts with the formation of tension cracks due to seepage forces. Internal erosion can be ruled out as the critical failure mode for soils already at low values of cohesion.

When comparing homogeneous and heterogeneous rock mass, significant differences can be observed: in homogeneous rock mass, plug failure may occur at slightly lower hydraulic heads than piping. In heterogeneous rock mass, the critical gradients for piping are significantly lower than for plug failure, at least for medium- to fine-grained material. For coarse-grained material plug failure remains the decisive failure mode. On the one hand, coarse-grained

materials exhibit low cohesion, which makes them prone to plug failure. On the other hand, the coarse grains are less sensitive to erosion because of their comparatively high weight. Generally, the critical hydraulic head for coarse grained materials is slightly higher than for medium- to fine-grained material. This apparently deviates from the common assumption that coarse-grained materials are most susceptible to hydraulic failure modes, as exemplarily postulated by Sausgruber & Brandner (2003) and Sattler (2018). However, this relation changes for higher values of cohesion: while the resistance against plug failure increases more or less linearly with cohesion (see Figure 8.6), the resistance against piping is independent of the shear strength and remains at the same level as before.

The comparison shows that there is no particular failure mode, which is decisive under any possible conditions. Rather both, plug failure and piping should be considered when analysing ground and system behaviour of a tunnel. Last but not least, the calculations once more emphasize the importance of drainage and grouting measures in the weak rock mass. The calculated critical hydraulic heads are significantly lower than the typical overburden (and thus most likely the groundwater level) of infrastructure tunnels constructed in conventional excavation. In other words, a certain potential for hydraulic failure exists in most cases of tunnels in weak and water-bearing rock mass.

8.6 Relevance of total inflow

The scenarios described above do not inevitably lead to a collapse of the tunnel. In example, particularly in low-permeability and cohesive rock mass, plug failure may occur ahead of the face without any noticeable consequences (despite increased displacement of the tunnel face). In such cases, the inflow rate, and consequently the particle transport due to erosion, is usually low. Displacement of the plug causes an immediate decrease of the seepage forces, because sufficient re-charge to fill the developing void is not provided and the low inflow rate into the tunnel does not allow a particle transport to the tunnel in a relevant extent. For an assessment whether hydraulic failure provides the potential for significant material ingress, the accumulated inflow rate can be taken as an indicative value.

The inflow rate at the tunnel face can be estimated from the calculations presented in chapter 6. In all calculations inflow rates at the tunnel face are logged. The evaluation of inflow rates is limited to the case of heterogeneous rock mass as the more relevant case. Figure 8.17 shows the inflow rate normalized by the initial hydraulic head, $\nu = q/h_0$, as a function of the transmissivity T of the fault zone. Since inflow rates vary when tunnelling through the fault zone (depending on the face position), both, the maximum inflow rate and the average value are evaluated.

A conservative assumption for the upper limit of the inflow rate in high-permeability fault zones (HPFZ) can be obtained by the exponential function shown in Figure 8.17. The accumulated inflow at the face furthermore depends on the face area and consequently on the tunnel diameter. The values presented in Figure 8.17 are based on a reference diameter $D_{ref} = 10\,\mathrm{m}$ and can be scaled to other diameters. The actual accumulated inflow at the tunnel face is calculated according to following equation:

$$q = 254 \cdot T^{0.82} \cdot h_0 \cdot \frac{D^2}{D_{ref}^2} \tag{8.36}$$

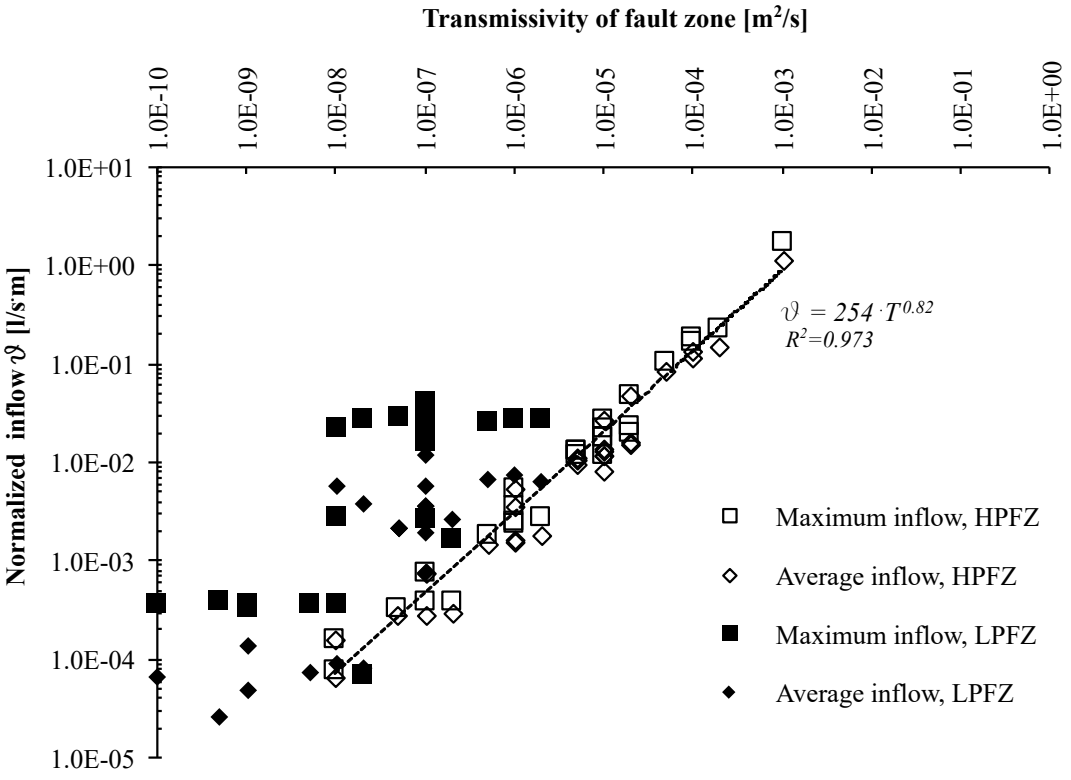

Figure 8.17: Normalized inflow at tunnel face as a function of fault zone transmissivity

where: q = Accumulated inflow rate at tunnel face [l/s]
T = Transmissivity of fault zone [m^2/s]
h_0 = Initial hydraulic head [m]
D = Tunnel diameter [m]
D_{ref} = Reference tunnel diameter = 10 [m]

With a given fraction of solids C_{solid} dissolved in the fluid, the quantity of solids q_{solid}, which is transported into the tunnel by erosion, can be calculated:

$$q_{solid} = q \cdot C_{solid} \tag{8.37}$$

The magnitude of C_{solid} can be estimated from reference cases. Measurements at the Semmering base tunnel showed typical contents of solids in the range of 10 - 200 g/l (max. 260 g/l), causing severe material ingress. When defining a threshold for the volumes loss due to erosion V_{limit} , the time required to reach this volume is:

$$t_{limit} = \frac{V_{limit} \cdot \rho_d}{q_{solid}} \tag{8.38}$$

The time $t_{erosion}$, during which an erosion process can occur, depends on the volume of the rock mass subject to erosion and on the advance rate. As a strongly idealized model, the former is presumed equal to the hemispherical zone up to half of the tunnel diameter ahead of the face, based on the considerations presented for plug failure. That is, erosion is only expected from the poorly confined zone up to a distance of D/2 ahead of the face. $t_{erosion}$ can be calculated for a given advance rate $v_{advance}$:

$$t_{erosion} = \frac{D}{2 \cdot v_{advance}} \tag{8.39}$$

Erosion from more distant areas, e.g. through a hydraulic bypass with greater extent, cannot be assessed adequately with the equation above. In such cases, the decisive boundary conditions, such as length and flow cross section of the hydraulic bypass, vary in a large range and do not allow general statements.

From Equations 8.36 - 8.39, the critical hydraulic head can be calculated as a function of fault zone transmissivity:

$$h_{crit} = \frac{2 \cdot V_{limit} \cdot \rho_d \cdot v_{advance}}{24 \cdot 3600 \cdot 254 \cdot T^{0.82} \cdot D \cdot \frac{D^2}{D_{ref}^2} \cdot C_{solid}} = \frac{V_{limit} \cdot \rho_d \cdot v_{advance}}{1.097 \cdot 10^7 \cdot T^{0.82} \cdot \frac{D^3}{D_{ref}^2} \cdot C_{solid}} \tag{8.40}$$

where: h_{crit} = Critical hydraulic head [m]
V_{limit} = Threshold of volume loss due to erosion [m^3]
ρ_d = Specific dry weight of solid fraction [g/m^3]
$v_{advance}$ = Advance rate of excavation [m/d]
T = Transmissivity of fault zone [m^2/s]
D = Tunnel diameter [m]
D_{ref} = Reference tunnel diameter = 10 [m]
C_{solid} = Fraction of solids [g/l]

The results of this equation for different fractions of solids (10 g/l; 50 g/l; 100 g/l; 200 g/l) is shown in Figure 8.18 with following assumptions: $V_{limit} = 1\,m^3$; D = 10 m; $v_{advance} = 4$ m/d; $\rho_d = 2800\,kg/m^3$.

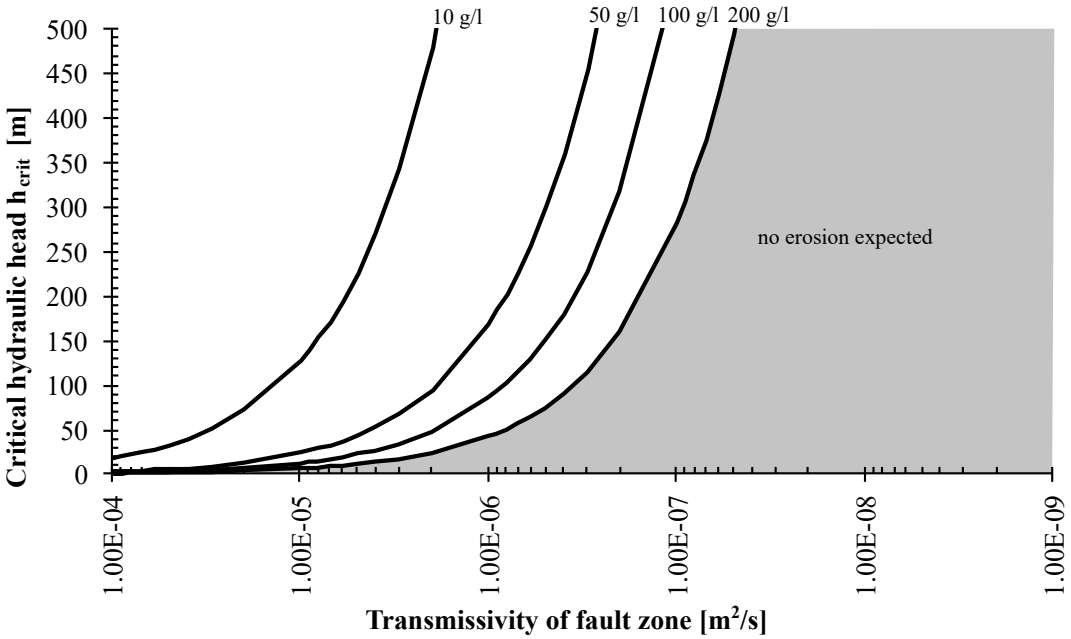

Figure 8.18: Critical hydraulic head for selected fractions of solids as a function of fault zone transmissivity, calculated with following assumptions: $V_{limit} = 1\,m^3$; D = 10 m; $v_{advance} = 4$ m/d; $\rho_d = 2800\,kg/m^3$

This calculation shows that erosion close to the tunnel face can practically be ruled out at a fault zone transmissivity of $< 5 \cdot 10^{-8}\,m^2/s$. This transmissivity corresponds e.g. to a fault zone with a thickness of 0.5 m and a hydraulic conductivity of 10^{-7} m/s. This study

points out that already comparatively thin fault zones bear significant potential for erosion in relevant scales. It is recalled that the above-mentioned equations are derived for fault zones (or a series of fault zones) with a higher permeability than the host rock (HPFZ) and should therefore solely be used in this context.

In case of homogeneous rock mass the inflow rate at the tunnel face can be calculated by substituting Darcy's law (Equation 2.4) into the continuity equation (Equation 2.1). For simplicity, a uniform hydraulic gradient according to Equation 6.9 is assumed at the tunnel face. When this inflow rate is substituted into Equation 8.37, the critical hydraulic head can be calculated as described above. The full analytical description is omitted at this point. For a hydraulic conductivity of $k = 10^{-6}$ m/s and a fraction of solids of 200 g/l, the critical hydraulic head for erosion in homogeneous rock mass evaluates to approx. 15 000 m (for the same boundary conditions as described above). This order of magnitude evaluation shows that erosion basically is uncritical in homogeneous rock mass provided that the large-scale permeability remains unaffected.

8.7 Collapse scenarios

The calculations presented above show that hydraulic failure may occur already at comparatively low hydraulic heads. However, hydraulic failure does not inevitably lead to a collapse of the tunnel or even to a particularly critical situation during excavation. Rather, the initial hydraulic failure can trigger a process, which - under certain conditions - ends up in a large-scale collapse or material ingress. If failure is detected in time and adequate mitigation measures can be taken, or if certain boundary conditions change over time (e.g. reduced inflow to the tunnel face due to low groundwater re-charge), the process may be stopped or stop by itself. With respect to the initial failure modes identified above, two potential scenarios are identified that may finally lead to a large-scale collapse or mud ingress:

1. *Plug failure or cracking with subsequent erosion*, see Figure 8.19a: The failure process initiates with shear or tensile failure of the plug (or a combination of both). In certain cases such as high hydraulic gradients and high inflow rates, failure of the plug may straight away cause a large-scale collapse of the face at this stage. Otherwise, the initial failure may cause increased displacements of the tunnel face without serious consequences at first. In case of limited groundwater re-charge, the hydraulic gradient and the seepage forces decrease immediately after the plug detaches from the surrounding rock mass and the plug can stabilize again. The initial failure of the plug may easily remain undetected during excavation. In case of sufficient re-charge, increased surge towards the interface of plug and surrounding rock mass can occur and initiate piping along tension cracks, failure planes, and within the poorly confined rock mass of the plug (Figure 8.19, upper right). Due to piping, the aperture of cracks increases and new voids propagate further into the rock mass. Local gravity- or stress-induced failures may contribute to this process. The increase of void volume continuously leads to an increase of rock mass permeability (and consequently higher inflow into the tunnel) in a more or less self-amplifying process. At the same time, seepage contributes to the deterioration of the rock mass strength in the poorly confined area of the plug (e.g. by dissolving chemical bonding or - in case of cohesive material - by a strength reduction due to an increase of the water content, as shown by (Wudtke & Witt, 2010)).

2. *Hydraulic bypass with subsequent erosion*, see Figure 8.19b: The failure process initiates with formation of a hydraulic bypass (short-circuit) to a zone with high hydraulic heads. This hydraulic bypass can either be caused by excavation (e.g. borehole drilled behind

a low-permeability layer) or be of natural origin (e.g. opening of cracks due to wash-out of the infill or stress redistribution). Once erosion commences, it can propagate further into the rock mass and increase the void volume. Local gravity- or stress-induced failures may further enlarge the voids. Similarly to plug failure, this process is more or less self-amplifying, because the voids cause an increased permeability.

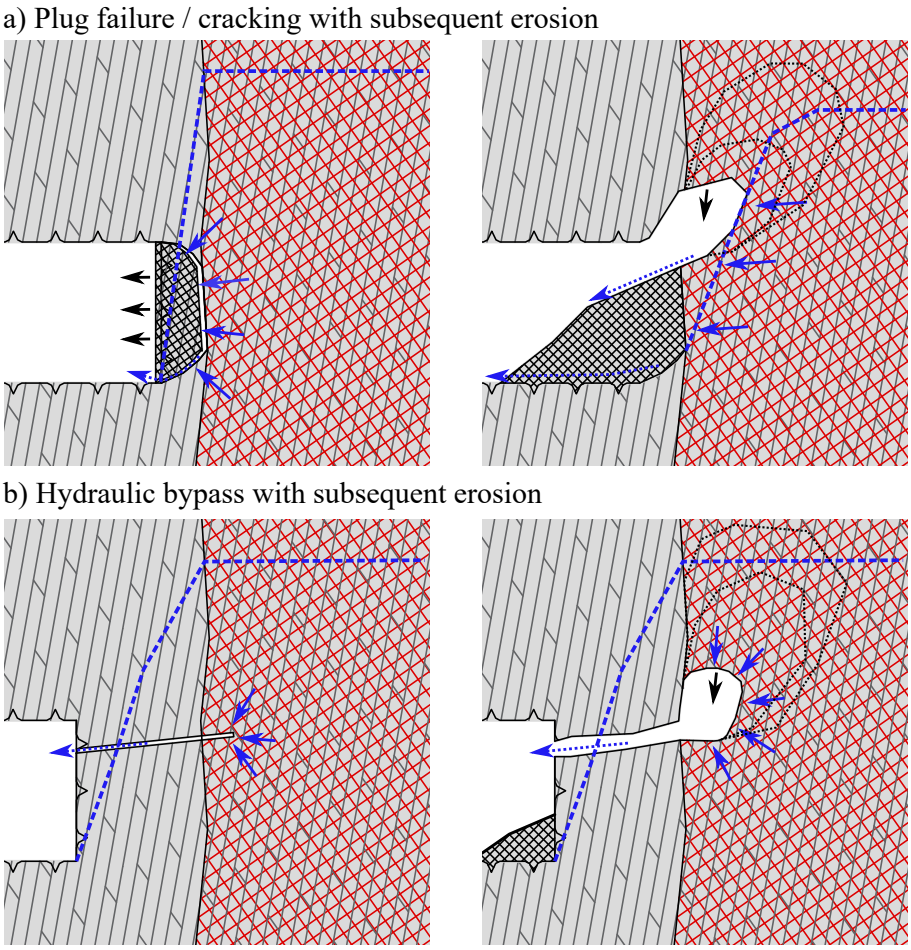

Figure 8.19: Collapse scenarios for hydraulic failure: a) Plug failure and cracking with subsequent erosion, initial stage (left) and progressed stage (right); b) Hydraulic bypass with subsequent erosion, initial stage (left) and progressed stage (right)

In both scenarios, the tunnel finally collapses when the volume of voids and deteriorated rock mass exceeds a critical size. A general statement when this stage is reached is impossible (not even if project-specific detailed information is available). However, understanding of the above-mentioned collapse scenarios may assist in planning of suitable prevention and mitigation measures as well as in detection of these processes during excavation.

9 Conclusion

The presence of groundwater affects the ground and system behaviour of tunnels in various ways, particularly in weak rock mass, such as geological fault zones, and under high overburden. The aim of this thesis is a contribution to understanding the hydraulic failure modes in such conditions. Following issues have been addressed:

- An extensive numerical study was conducted, which allows for conclusions on the distribution of hydraulic heads and gradients in both, homogeneous and heterogeneous rock mass. As shown, the hydraulic head field essentially depends on the initial hydraulic head, the rock mass permeability, the hydraulic contrast between host rock and fault zone, the advance rate of the excavation and the geometrical dimensions. The most adverse groundwater conditions for tunnelling evolve when approaching a zone with considerably higher permeability. In such cases, drawdown ahead of the face is hindered due to re-charge from the fault zone. The hydraulic head in such a high-permeability zone may therefore be close to the initial hydraulic head when reaching it, unless drainage measures are applied in advance.

- Closed-form solutions were developed to estimate the hydraulic heads and gradients ahead of the face for both, homogeneous and heterogeneous rock mass. These equations allow for an assessment of the steady-state hydraulic head field as well as transient conditions. The proposed approach represents a simple alternative to time-consuming three-dimensional seepage flow analyses and may provide the basis for further stability considerations. The applicability of the developed solution was verified in back-analyses of pore pressure measurements conducted during excavation of the Semmering base tunnel.

- Two decisive hydraulic failure modes could be distinguished, based on numerical analyses and a review of relevant case histories: Low confinement stresses (i.e. stresses perpendicular to the face) prevail in a bullet-shaped to hemispherical zone ahead of the face. These stress conditions facilitate shear and / or tensile failure in the rock mass ahead of the face due to seepage forces acting towards the tunnel. This failure mode is referred to as *plug failure / cracking*. In addition, *piping*, that is erosion along a hydraulic bypass such as a crack or borehole, may occur in case of sufficiently high flow velocities. Internal erosion (i.e. erosion of the ground stratum) could practically be ruled out as a relevant failure mode, if the rock mass exhibits at least a minimum of cohesion (as fault rocks typically do).

- For assessing the above-mentioned failure modes, closed-form calculation models were developed. The model for plug failure and cracking is based on a limit equilibrium analysis of a hemispherical failure body ahead of the face. For an identification of the piping potential, the critical velocity, under which no erosion occurs, is taken as a lower threshold. The critical hydraulic head for piping can thus be estimated as a function of the bypass aperture. Nomograms based on the proposed calculation models allow for a fast assessment of the ground and system behaviour in various geotechnical conditions.

- Stability analyses were conducted for a large parameter range, which emphasize the importance of drainage and / or grouting measures under the objective conditions, since hydraulic failure can occur already under low hydraulic heads. An assessment of the potential benefit of grouting measures can be performed using specific nomograms proposed in this thesis.
- Hydraulic failure does not inevitably lead to a large-scale tunnel collapse. For an improved understanding of the processes leading to a collapse, or at least to severe material ingress into the tunnel, two collapse scenarios were identified: initial plug failure with subsequent erosion and regressive erosion through a hydraulic bypass. Both scenarios largely depend on the groundwater inflow rate into the tunnel. For plug failure with subsequent erosion a simplified model was presented to assess the erosion potential, based on the inflow rate into the tunnel.

An adequate assessment of the potential hydraulic failure mechanisms in the design allows for determination and specification of suitable counter measures and for establishment of a monitoring concept. These items are essential features for applying the observational method, which is commonly used in deep tunnels with respect to the inevitable uncertainties in the geological model and the geotechnical parameters. The findings and methods provided in this thesis may assist in the identification of critical situations in time. The author is convinced that this work can contribute to a safer and more efficient construction of tunnels in weak and water-bearing rock mass.

Last but not least, a large research demand remains for future contributors, particularly targeting erosion processes in fault rocks. Hardly any scientific work could be found on this topic. The knowledge gained by laboratory tests as well as by physical and numerical models could allow for establishing a suitable constitutive model for erodibility. The fact that erosion plays a decisive role in the majority of case histories reporting hydraulic-induced collapses or severe material ingress into tunnels emphasizes the importance of this topic.

Bibliography

Anagnostou, G. (2009). The Effect of Advance-Drainage on the Short-Term Behaviour of Squeezing Rocks in Tunneling. In *International Symposium on Computational Geomechanics (ComGeo I)*, (pp. 1–12)., Juan-les Pins, Cote d'Azur.

Anagnostou, G. & Kovári, K. (1994). Die Stabilität der Ortsbrust bei Erddruckschilden. *Mitteilungen der Schweiz. Gesellschaft für Boden- und Felsmechanik*, (129), 27–34.

Anagnostou, G. & Kovári, K. (1996). Face Stability Conditions with Earth-Pressure-Balanced Shields. *Tunnelling and Underground Space Technology*, *11*(2), 165–173.

Asef, M. R. & Reddish, D. J. (2002). The impact of confining stress on the rock mass deformation modulus. *Géotechnique*, *52*(4), 235–241.

Austrian Society for Geomechanics (2010). *Guideline of the Geotechnical Design of Underground Structures with Conventional Excavation* (Translated from version 2.1 ed.). Salzburg: Austrian Society for Geomechanics.

Bense, V. F., Gleeson, T., Loveless, S. E., Bour, O., & Scibek, J. (2013). Fault zone hydrogeology. *Earth-Science Reviews*, *127*, 171–192.

Biot, M. A. (1941). General theory of three-dimensional consolidation. *Journal of Applied Physics*, *12*(2), 155–164.

Bobet, A. (2010). Characteristic Curves for Deep Circular Tunnels in Poroplastic Rock. *Rock Mechanics and Rock Engineering*, *43*(2), 185–200.

Bossart, P., Meier, P. M., Moeri, A., Trick, T., & Mayor, J.-C. (2002). Geological and hydraulic characterisation of the excavation disturbed zone in the Opalinus Clay of the Mont Terri Rock Laboratory. *Engineering Geology*, *66*(1-2), 19–38.

Brandtner, M. & Lenz, G. (2017). Checking the system behaviour using a numerical model. *Geomechanics and Tunnelling*, *10*(4).

Briaud, J. L. (2013). *Geotechnical engineering.* Hoboken, New Jersey: John Wiley & Sons, Inc.

Busch, K., Luckner, L., & Tiemer, K. (1993). *Lehrbuch der Hydrogeologie: Geohydraulik.* Berlin, Stuttgart, Germany: Gebrüder Borntraeger.

Coussy, O. (2004). *Poromechanics. Mechanics of porous continua.* (2nd ed.). Chichester, England: John Wiley & Sons Ltd.

Davidenkoff, R. (1976). *Anwendung von Filtern im Wasserbau.* Berlin/München/ Düsseldorf, Germany: Verlag Ernst & Sohn.

Egger, P., Ohnuki, T., & Kanoh, Y. (1982). Bau des Nakayama-Tunnels, Kampf gegen Bergwasser und vulkanisches Lockergestein. *Rock Mechanics*, *12*, 275–293.

El Tani, M. (1999). Water inflow into tunnels. In Alten, T., Backer, L., Bollingmo, P., Broch, E., Holmoy, K., Holter, K., & Nielsen, K. (Eds.), *Challenges for the 21st century - Proceedings of the world tunnel congress '99*, (pp. 61–70)., Rotterdam. Balkema.

El Tani, M. (2002). Circular tunnel in a semi-infinite aquifer. *Tunnelling and Underground Space Technology*, *18*(1), 49–55.

EN 1997-1 (2014). Eurocode 7: Geotechnical design, Part 1: General rules. ÖNORM, Austrian Standards Institute.

Evans, J. P., Forster, C. B., & Goddard, J. V. (1997). Permeability of fault-related rocks, and implications for hydraulic structure of fault zones. *Journal of Structural Geology*, *19*(11), 1393–1404.

Fasching, F. & Vanek, R. (2011). Engineering geological characterisation of fault rocks and fault zones / Ingenieurgeologische Charakterisierung von Störungsgesteinen und Störungszonen. *Geomechanics and Tunnelling*, *4*(3), 181–194.

Faulkner, D., Jackson, C., Lunn, R., Schlische, R., Shipton, Z., Wibberley, C., & Withjack, M. (2010). A review of recent developments concerning the structure, mechanics and fluid flow properties of fault zones. *Journal of Structural Geology*, *32*(11), 1557–1575.

Fredlund, D. G. & Rahardjo, H. (1993). *Soil Mechanics for Unsaturated Soils*. Hoboken, NJ, USA: John Wiley & Sons, Inc.

Frieg, B., Blaser, P., Adams, J., Albert, W., Dollinger, H., Kuhlmann, U., & Lanyon, G. (2012). Grimsel test site - excavation disturbed zone experiment (edz). Technical report 98-01, National Cooperative for the Disposal of Radioactive Waste.

Gärber, R. (2003). *Design of deep galleries in low permeable saturated porous media*. Doctoral thesis, Ecole Polytechnique Federale de Lausanne, Switzerland.

Giraud, A., Picard, J., & Rousset, G. (1993). Time dependent behavior of tunnels excavated in porous mass. *International Journal of Rock Mechanics and Mining Sciences & Geomechanics Abstracts*, *30*(7), 1453–1459.

Goricki, A. (2003). *Classification of Rock Mass Behaviour based on a Hierarchical Rock Mass Characterization for the Design of Underground Structures*. Doctoral thesis, Graz University of Technology, Austria.

Goricki, A. & Pimentel, E. (2013). Triaxial test on cataclasites. In Schubert, W., Kluckner, A., & Pilgerstorfer, T. (Eds.), *Workshop 'Characterization of Fault zones', Extended Abstracts*, (pp. 22–27). Österreichische Gesellschaft für Geomechanik.

Graziani, A. & Ribacchi, R. (2001). Short and long-term load conditions for tunnels in low permeability ground in the framework of the convergence-confinement method. In Adachi et. al. (Ed.), *Modern Tunnelling Science and Technology*, Lisse, Netherlands. A. A. Balkema.

Grossauer, K. (2001). Tunnelling in heterogeneous ground - numerical investigation of stresses and displacements. Diploma thesis, Graz University of Technology, Austria.

Gschwandtner, G. (2010). Analytische Berechnungsansätze zum Kennlinienverfahren. Master thesis, Montanuniversität Leoben, Austria.

Gschwandtner, G. G., Lenz, G., & Wagner, O. K. (2019). Collapses in the vicinity of fault zones – Geotechnical causes and identification. *Geomechanics and Tunnelling*, *12*(6), 667–673.

Gysel, M. (2002). Anhydrite Dissolution Phenomena: Three Case Histories of Anhydrite Karst Caused by Water Tunnel Operation. *Rock Mechanics and Rock Engineering*, *35*(1), 1–21.

Habimana, J., Labiouse, V., & Descoeudres, F. (2002). Geomechanical characterisation of cataclastic rocks: experience from the Cleuson–Dixence project. *International Journal of Rock Mechanics and Mining Sciences*, *39*(6), 677–693.

Heitfeld, K. & Koppelberg, W. (1981). Durchlässigkeitsuntersuchungen mittels WD-Versuchen. *ZBL Geol Paläont Teil I.*

Hennings, F. (1908). *Projekt und Bau der Albulabahn, Denkschrift.* Kommissions-Verlag von F. Schuler.

Holter, K. G. (2015). *Properties of waterproof sprayed concrete tunnel linings.* Doctoral thesis, Norwegian University of Science and Technology, Norway.

Innerhofer, G. (1984). Wirkung des Kluftwasserdrucks auf einen Felskörper. *Felsbau*, *2*(1), 26–31.

Innerhofer, G. (2008). Action of Force on Rock Mass by Crack Water Pressure. *Geomechanik und Tunnelbau*, *1*(6), 583–589.

Itasca Consulting Group, Inc. (2017). FLAC3D: Fast Lagrangian Analysis of Continua in Three-Dimensions, Ver. 6.0. Minneapolis: Itasca.

Kastner, H. (1962). *Statik des Tunnel- und Stollenbaus.* Berlin, Germany: Springer Verlag.

Knittel, A. (1995). Geotechnische Probleme beim Bau des Erkundungsstollens Kaponig. In B. Schweighofer & H. Müller (Eds.), *Mitteilungen des Instituts für Bodenforschung und Baugeologie, Abteilung Baugeologie*, volume 5 (pp. 67–101). Universität für Bodenkultur Wien.

Kolymbas, D. (1998). *Geotechnik - Tunnelbau und Tunnelmechanik.* Berlin - Heidelberg, Germany: Springer-Verlag.

Langguth, H.-R. & Voigt, R. (2004). *Hydrogeologische Methoden* (Zweite überarbeitete Auflage ed.). Berlin, Heidelberg, Germany: Springer Verlag.

Lee, I.-M., Nam, S.-W., & Ahn, J.-H. (2003). Effect of seepage forces on tunnel face stability. *Canadian Geotechnical Journal*, *40*(2), 342–350.

Leitner, R. & Müller, H. (2007). Numerische Modellierung von Wasserzutritten für tiefliegende Tunnel in Störungszonen. In *Massnahmen zur Beherrschung des Wassers in der Geotechnik*, volume 30, (pp. 293–309). Mitteilungsheft der Gruppe Geotechnik Graz.

Lenz, G., Poisel, A., Brandtner, M., Goricki, A., & Wagner, O. (2018). Semmering Base Tunnel - Geotechnical models in design and construction. *Geomechnanics and Tunnelling*, *11*(5), 559–565.

Mahmutoglu, Y., Vardar, M., Kocak, C., & Sans, G. (2006). Tunnelling difficulties under squeezing and flowing conditions at Ayas tunnel. *Felsbau*, *24*(5).

Mikkelsen, P. & Green, G. (2003). Piezometers in fully grouted boreholes. In *Field Measurements in Geomechanics* (pp. 545–553). Taylor & Francis.

Millen, B., Höfer-Öllinger, G., & Brandl, J. (2015). Change in Hydraulic Properties of Rock Mass Due to Tunnelling. In *Engineering Geology for Society and Territory - Volume 6* (pp. 937–940). Cham: Springer International Publishing.

Müllner, B. (1991). Beitrag zur Untersuchung der Erosionssicherheit bindiger Mischböden bei vertikaler Durchströmung. *Mitteilungen des Fachgebietes Grundbau, Gesamthochschule Kassel - Universität*.

ÖBB Infrastruktur AG (2015). Tunnel chain Granitztal - Project documents. Tender phase.

ÖBB Infrastruktur AG (2019). Semmering base tunnel - Project documents. Tender and execution phase.

Perazzelli, P., Leone, T., & Anagnostou, G. (2014). Tunnel face stability under seepage flow conditions. *Tunnelling and Underground Space Technology*, *43*, 459–469.

Perrochet, P. (2005a). A simple solution to tunnel or well discharge under constant drawdown. *Hydrogeology Journal*, *13*(5-6), 886–888.

Perrochet, P. (2005b). Confined Flow into a Tunnel during Progressive Drilling: An Analytical Solution. *Ground Water*, *43*(6), 943–946.

Perrochet, P. & Dematteis, A. (2007). Modeling Transient Discharge into a Tunnel Drilled in a Heterogeneous Formation. *Ground Water*, *45*(6), 786–790.

Pilgerstorfer, T. (2014). *Mechanical Characterization of Fault Zones*. Doctoral thesis, Graz University of Technology, Austria.

Prinz, H. & Strauss, R. (2011). *Ingenieurgeologie* (5 ed.). Heidelberg: Spektrum Akademischer Verlag.

Pusch, R. (1989). Alteration of the Hydraulic Conductivity of Rock by Tunnel Excvavation. *Int. J. Rock. Mech. Min. Sci. & Geomech.*, *26*(1), 79–83.

Radončić, N. (2011). *Tunnel design and prediction of system behaviour in weak ground*. Doctoral thesis, Graz University of Technology, Austria.

Rehfeld, E. (1967). Die Erosionsbeständigkeit bindiger Lockergesteine - die wichtigsten Grundlagen zur Dimensionierung von Dichtungsschichten aus natürlichem Erdstoff. *Wissenschaftliche Zeitschrift der TU Dresden*, *16*(5), 1431 – 1437.

Riedmüller, G., Brosch, F., Klima, K., & Medley, E. W. (2001). Engineering geological characterization of brittle faults and classification of fault rocks. *Felsbau*, (4), 13–19.

Ruse, N. M. (2004). *Räumliche Betrachtungen der Standsicherheit der Ortsbrust beim Tunnelvortrieb*. Doctoral thesis, Universität Stuttgart, Germany.

Salencon, J. (1969). Contraction quasi-statique d'une cavite a symmetric spherique ou cylindrique dans un millieu elastoplastique. *Annales des Ponts et Chaussees*, *4*, 231–236.

Sattler, T. (2018). Charakterisierung von Størungsgesteinen im Hinblick auf ihr Potenzial für "fließendes Gebirgsverhalten". Master thesis, Graz University of Technology, Austria.

Saucke, U. (2006). Nachweis der Sicherheit gegen innere Erosion für körnige Erdstoffe. *Geotechnik*, *29*(1), 43–54.

Sausgruber, T. & Brandner, R. (2003). The relevance of brittle fault zones in tunnel construction—Lower Inn Valley feeder line north of the Brenner Base Tunnel, Tyrol, Austria. *Mitt. Österr. Geol. Ges*, *94*(August), 157–172.

Schanz, T., Vermeer, P., & Bonnier, P. (1999). The hardening soil model: formulation and verification. In *Beyond 2000 in computational geotechnics - 10 Years of PLAXIS*, Rotterdam. Balkema.

Schubert, P. & Marinko, T. (1992). Karawankentunnel Süd - Bauerfahrungen. *Felsbau*, *10*(3), 116–118.

Schwarz, L., Reichl, I., Kirschner, H., & Robl, K. P. (2006). Risks and hazards caused by groundwater during tunnelling: geotechnical solutions used as demonstrated by recent examples from Tyrol, Austria. *Environ. Geol.*, *49*, 858—864.

Selvadurai, P., Selvadurai, P. A., & Nejati, M. (2019). A multi-phasic approach for estimating the Biot coefficient for Grimsel granite. *Solid Earth*, *10*(6), 2001–2014.

Terzaghi, K. (1936). The shearing resistance of saturated soils. In *Proc. First Int. Conf Soil Mech.*, volume 1, (pp. 54–56).

Theiler, A., Zingg, S., & Anagnostou, G. (2013). Analysis of a demanding historical tunnel: Albula. In *Underground. The Way to the Future* (pp. 2022–2029). CRC Press.

Vogelhuber, M. (2007). *Der Einfluss des Porenwasserdrucks auf das mechanische Verhalten kakiritisierter Gesteine*. Doctoral thesis, ETH Zürich, Switzerland.

Wang, W. S. (1981). Mechanisms of soil liquefaction. In *International Conferences on recent Advances in geotechnical earthquake engineering and soil dynamics*, volume 14, (pp. 221–226).

Winkler, G., Kurz, W., Hergarten, S., & Kiechl, E. (2010). Hydraulische Charakterisierung von Störungskernzonen in kristallinen Festgesteinen am Beispiel der Talhof-Störung (Ostalpen). *Grundwasser*, *15*(1), 59–68.

Winkler, G. & Reichl, P. (2014). Scale dependent hydraulic investigations of faulted crystalline rocks – examples from the Eastern Alps, Austria. In J. Sharp (Ed.), *Fractured Rock Hydrogeology* chapter 11, (pp. 181–197). CRC Press.

Wudtke, R. B. (2014). *Hydraulischer Grundbruch in bindigem Baugrund*. Doctoral thesis, Bauhaus-Universität Weimar, Germany.

Wudtke, R. B. & Witt, K. J. (2010). Hydraulischer Grundbruch im bindigen Baugrund - Schadensmechanismen und Nachweisstrategie. *9. Geotechnik-Tag in München - Wechselwirkungen Boden - Wasser - Bauwerk, München, 19.10.2010, Lehrstuhl und Prüfamt für Grundbau, Bodenmechanik, Felsmechanik und Tunnelbau der Technischen Universität München*, (Heft 46), 33–44.

Youd, L. (1973). Liquefaction, flow, and associated ground failure. Technical report, United States Department of the Interior. Geological Survey Circular 688.

Zingg, S. (2016). *Static effects and aspects of feasibility and design of drainages in tunnelling*. Doctoral thesis, ETH Zürich, Switzerland.

Zingg, S. & Anagnostou, G. (2008). The effects of advance drainage on face stability in homogeneous ground. In *ITA-AITES World Tunnel Congress and 38th General Assembly (WTC 2012)*, Bangkok, Thailand.

Zingg, S. & Anagnostou, G. (2012). Tunnel face stability in narrow water-bearing fault zones. In *Rock Engineering and Technology for Sustainable Underground Construction*, Stockholm, Sweden.

Zou, Y. (2000). Der vom Spannungszustand und Bodengefüge abhängige Erosionsdurchbruch bindiger Böden. *Wasserwirtschaft*, *90*(11), 554–559.